Reviews of Geophysics

REVIEW ARTICLE
10.1029/2024RG000842

Radar Polarimetry in Glaciology: Theory, Measurement Techniques, and Scientific Applications for Investigating the Anisotropy of Ice Masses

Benjamin H. Hills[1], T. J. Young[2], David A. Lilien[3], Esther Babcock[4], Nicole Bienert[5], Donald Blankenship[6], John Bradford[1,7], Giancorrado Brighi[8], Alex Brisbourne[9], Jørgen Dall[10], Reinhard Drews[11], Olaf Eisen[12,13], M. Reza Ershadi[11], Tamara A. Gerber[14], Nicholas Holschuh[15], Daniela Jansen[12], Thomas M. Jordan[16], Nanna B. Karlsson[17], Jilu Li[18], Carlos Martín[9], Kenichi Matsuoka[19], Daniel May[20], Falk M. Oraschewski[17], John Paden[18], Nicholas M. Rathmann[14], Neil Ross[21], Dustin M. Schroeder[20,22], Martin Siegert[23], Matthew R. Siegfried[1], Emma Smith[24], and Ole Zeising[12]

[1]Department of Geophysics, Colorado School of Mines, Golden, CO, USA, [2]School of Geography and Sustainable Development, University of St Andrews, St Andrews, UK, [3]Department of Earth and Atmospheric Sciences, Indiana University, Bloomington, IN, USA, [4]Logic Geophysics & Analytics LLC, Anchorage, AK, USA, [5]Department of Electrical, Computer & Energy Engineering, University of Colorado Boulder, Boulder, CO, USA, [6]Institute for Geophysics, Jackson School of Geosciences, University of Texas, Austin, TX, USA, [7]Office of Global Initiatives and Business Development, Colorado School of Mines, Golden, CO, USA, [8]Department of Industrial Engineering, University of Bologna, Forlì, Italy, [9]British Antarctic Survey, Natural Environment Research Council, Cambridge, UK, [10]Department of Space Research and Space Technology, Technical University of Denmark, Copenhagen, Denmark, [11]Department of Geosciences, University of Tübingen, Tübingen, Germany, [12]Alfred Wegener Institute Helmholtz Centre for Polar and Marine Research, Bremerhaven, Germany, [13]Faculty of Geosciences, University of Bremen, Bremen, Germany, [14]Niels Bohr Institute, University of Copenhagen, Copenhagen, Denmark, [15]Department of Geology, Amherst College, Amherst, MA, USA, [16]Plymouth Marine Laboratory, Plymouth, UK, [17]Department of Glaciology and Climate, Geological Survey of Denmark and Greenland, Copenhagen, Denmark, [18]Center for Remote Sensing and Integrated Systems, University of Kansas, Lawrence, KS, USA, [19]Norwegian Polar Institute, Tromsø, Norway, [20]Department of Geophysics, Stanford University, Stanford, CA, USA, [21]School of Geography, Politics and Sociology, Newcastle University, Newcastle, UK, [22]Department of Electrical Engineering, Stanford University, Stanford, CA, USA, [23]Tremough House, University of Exeter, Penryn Campus, Cornwall, UK, [24]School of Earth and Environment, University of Leeds, Leeds, UK

Abstract Dielectric anisotropy in ice alters the propagation of polarized radio waves, so polarimetric radar sounding can be used to survey anisotropic properties of ice masses. Ice anisotropy is either intrinsic, associated with ice-crystal orientation fabric (COF), or extrinsic, associated with material heterogeneity, such as bubbles, fractures, and directional roughness at the glacier bed. Anisotropy develops through a history of snow deposition and ice flow, and the consequent mechanical properties of anisotropy then feed back to influence ice flow. Constraints on anisotropy are therefore important for understanding ice dynamics, ice-sheet history, and future projections of ice flow and associated sea-level change. Radar techniques, applied using ground-based, airborne, or spaceborne instruments, can be deployed more quickly and over a larger area than either direct sampling, via ice-core drilling, or analogous seismic techniques. Here, we review the physical nature of dielectric anisotropy in glacier ice, the general theory for radio-wave propagation through anisotropic media, polarimetric radar instruments and survey strategies, and the extent of applications in glacier settings. We close by discussing future directions, such as polarimetric interpretations outside COF, planetary and astrophysical applications, innovative survey geometries, and polarimetric profiling. We argue that the recent proliferation in polarimetric subsurface sounding radar marks a critical inflection, since there are now several approaches for data collection and processing. This review aims to guide the expanding polarimetric user base to appropriate techniques so they can address new and existing challenges in glaciology, such as constraining ice viscosity, a critical control on ice flow and future sea-level change.

Plain Language Summary Radar is commonly used to examine into and beneath glaciers and ice sheets where direct observations are difficult to obtain. In this review, we focus on one specific radar application, polarimetry, which analyzes the differences between radar measurements with different antenna orientations. Radar polarimetry is primarily used to measure the orientation of ice crystals, the pattern of which can: (a) influence the flow of an ice mass, an important factor controlling future global sea levels; and (b) record

Benjamin H. Hills, T. J. Young, and David A. Lilien contributed equally to this work.

Key Points:

- Individual ice crystals are dielectrically anisotropic, so polarimetric radar can be used to assess patterns in the bulk crystal orientation
- Crystal orientation depends on past deformation and affects viscosity, so polarimetric radar can constrain ice motion in the past and future
- Anisotropy in dynamic parts of Earth's ice sheets and within planetary ices are knowledge gaps and therefore are new research foci

Correspondence to:
B. H. Hills,
benjaminhhills@gmail.com

Citation:
Hills, B. H., Young, T. J., Lilien, D. A., Babcock, E., Bienert, N., Blankenship, D., et al. (2025). Radar polarimetry in glaciology: Theory, measurement techniques, and scientific applications for investigating the anisotropy of ice masses. *Reviews of Geophysics*, *63*, e2024RG000842. https://doi.org/10.1029/2024RG000842

Received 20 AUG 2024
Accepted 5 OCT 2025

Author Contributions:

Conceptualization: Benjamin H. Hills, T. J. Young, Reinhard Drews, Olaf Eisen, Daniela Jansen, Thomas M. Jordan, John Paden, Neil Ross, Dustin M. Schroeder, Matthew R. Siegfried, Emma Smith
Data curation: Benjamin H. Hills, T. J. Young, David A. Lilien, Jørgen Dall, Reinhard Drews, Olaf Eisen
Funding acquisition: Benjamin H. Hills, Matthew R. Siegfried
Project administration: Benjamin H. Hills, T. J. Young, David A. Lilien, Jørgen Dall, Reinhard Drews, Olaf Eisen, Tamara A. Gerber, Nicholas Holschuh, Daniela Jansen, Thomas M. Jordan, Nanna B. Karlsson, John Paden, Nicholas

M. Rathmann, Neil Ross, Dustin M. Schroeder, Matthew R. Siegfried
Software: Benjamin H. Hills
Supervision: T. J. Young, David A. Lilien, Jørgen Dall, Reinhard Drews, Olaf Eisen, Tamara A. Gerber, Nicholas Holschuh, Daniela Jansen, Thomas M. Jordan, Nanna B. Karlsson, John Paden, Nicholas M. Rathmann, Neil Ross, Dustin M. Schroeder, Matthew R. Siegfried
Visualization: Benjamin H. Hills, T. J. Young, David A. Lilien, Esther Babcock, John Bradford, Giancorrado Brighi, Jørgen Dall, Reinhard Drews, Olaf Eisen, M. Reza Ershadi, Tamara A. Gerber, Nicholas Holschuh, Daniela Jansen, Thomas M. Jordan, Jilu Li, Daniel May, Falk M. Oraschewski, John Paden, Nicholas M. Rathmann, Neil Ross, Dustin M. Schroeder, Matthew R. Siegfried, Ole Zeising
Writing – original draft: T. J. Young, Reinhard Drews, Olaf Eisen, Daniela Jansen, Thomas M. Jordan, Dustin M. Schroeder, Emma Smith
Writing – review & editing: Benjamin H. Hills, T. J. Young, David A. Lilien, Esther Babcock, Nicole Bienert, Donald Blankenship, John Bradford, Giancorrado Brighi, Alex Brisbourne, Jørgen Dall, Reinhard Drews, Olaf Eisen, M. Reza Ershadi, Tamara A. Gerber, Nicholas Holschuh, Daniela Jansen, Thomas M. Jordan, Nanna B. Karlsson, Jilu Li, Carlos Martín, Kenichi Matsuoka, Daniel May, Falk M. Oraschewski, John Paden, Nicholas M. Rathmann, Neil Ross, Dustin M. Schroeder, Martin Siegert, Matthew R. Siegfried, Emma Smith, Ole Zeising

past ice flow, providing insights into past climate on geologic timescales, up to tens of thousands of years. Recent innovations in radar tools have led to accelerated application of polarimetry in glaciological research, and future innovation will only expand the use case further. This review aims to act as an introduction to those unfamiliar with radar polarimetry, as a call to expand this small scientific community within glaciology and extend the relevant scientific applications, and as a guide to users of these techniques, not only in how they have been used historically, but also in the physical context for how best to interpret the polarimetric radar signature.

1. Introduction

Radar polarimetry in glaciology refers to the use of radar with known polarization to investigate the properties of ice and of the ice-bed interface. The propagation of radio waves through glaciers and ice sheets, and reflections from within and beneath them, both depend on polarization because individual ice crystals have many anisotropic (directionally varying) properties, including dielectric and mechanical anisotropy (Figure 1). These properties both largely result from the collective orientation of ice crystals, with greater crystal alignment resulting in stronger anisotropy. Thus, by measuring dielectric anisotropy, radar polarimetry can also offer information about mechanical anisotropy, an important control on ice flow (Shoji & Langway, 1988). Since the orientation of ice crystals is primarily a result of past ice deformation (Alley, 1988), radar polarimetry can also reveal ice-flow history. Other physical properties of the ice and the ice-bed interface, including properties that are important for ice flow such as roughness and water content, can be directional and can therefore also affect the measured radar polarization. Because polarimetric radar has become relatively inexpensive and easy to deploy, it is increasingly being used to investigate physical properties of the ice sheets and their implications for ice flow.

The history of radar polarimetry in glaciology starts with proofs of concept in the 1960s and 1970s (Bentley, 1975; Hargreaves, 1977, 1978; Jiracek, 1967), just a decade after radar sounding began to be widely used in glaciology (Bingham & Siegert, 2007; Dowdeswell & Evans, 2004). These methods have proliferated in recent decades after critical theoretical and laboratory advances (Fujita et al., 1993, 2006) as well as the development of ground-based phase-sensitive radars (e.g., the Autonomous phase-sensitive Radio Echo Sounder; ApRES) that allow relatively straightforward multi-polarization measurements (Brennan et al., 2014; Nicholls et al., 2015). These ground-based radar instruments are inexpensive, relatively simple to deploy, and generally offer high coherence between acquisitions. The growing body of polarimetric radar measurements is pushing knowledge of ice anisotropy beyond slow-flowing sites, where it has been sampled with ice cores, into more dynamic areas. These measurements of anisotropy over different flow regimes are important in achieving a better understanding of ice-sheet processes, and ultimately for accurate incorporation of anisotropic dielectric properties of the ice into predictions of future ice loss and sea-level rise.

While polarimetric methods are still being developed in glaciology, they have a longer history in spaceborne remote sensing (Ulaby & Elachi, 1990; Zebker & Van Zyl, 1991) from which we derive much of the theory presented here as well as adopt notation (Appendix A). Unlike the side-looking radar remote sensing literature, which focuses on surface and subsurface scattering for angles of incidence typically >20°, we mainly emphasize wave propagation *through* anisotropic media when viewed normal (zero- or nadir-incidence) to the ice surface. We term this latter type of measurement "radar sounding," in keeping with similar descriptions of both terrestrial and planetary instruments (Schroeder et al., 2020). In this way, polarimetric radar sounding is similar to seismic methods for detecting anisotropy in the solid Earth using measurements of shear-wave splitting (M. D. Long & Becker, 2010; Shen & Gao, 2021; Weiss et al., 1999), and those seismic methods have also been used in glaciology (Appendix B).

In this review, we synthesize radar polarimetry analyses in glaciology over the past six decades. We hope this material can serve as a reference, primarily for those new to the topic of radar polarimetry, but also to the experienced radar scientists seeking new applications in glaciology. We start with background on the physical properties of ice in Section 2, covering how glacier ice can be anisotropic, why that matters, and why it should be measurable with radar sounding. Then, we provide an overview of the relevant electromagnetic theory (Section 3) and measurement techniques (Section 4), hoping to create a standard framework and terminology for future studies to follow. These sections on background, theory, and technique are targeted toward readers who are new to the subject, in some cases reviewing elementary pieces of radar theory. In Section 5, we focus on polarimetric

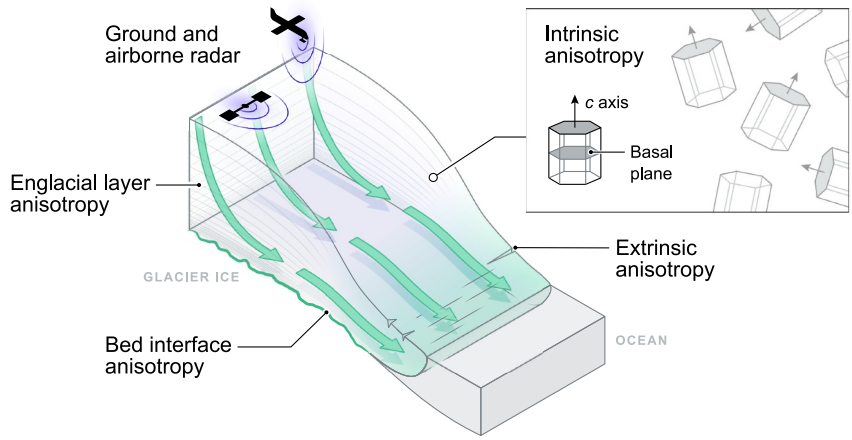

Figure 1. Illustration of anisotropy in the glacier setting. Intrinsic anisotropy is the result of orientations of individual ice crystals (inset) which, considered together, change the bulk ice properties. Extrinsic anisotropy is the result of directional disruptions in the ice media, either within the ice or at the ice-bed interface. Dielectric anisotropy can be measured with both ground-based and airborne radar sounding.

applications for sounding through glaciers and ice sheets, as well as the associated ice dynamic interpretations. In Section 6, we explore a more extended set of possible applications and describe our vision for the future of polarimetric radar in glaciology. Polarimetry is one amongst a group of developing radar sounding methods (e.g., multipass interferometry (Ariho et al., 2022), swath mapping (Holschuh et al., 2020), and others (Schroeder et al., 2020)) which are together changing the way glaciers and ice sheets are surveyed and monitored, both on Earth and in planetary environments.

2. Background: Dielectric Anisotropy in Glacier Ice

Bulk anisotropy in a polycrystalline material can arise in several ways. Following terminology in the seismology literature (e.g., Fichtner et al., 2013; N. Wang et al., 2013), there are two broad classifications, "intrinsic" and "extrinsic." Intrinsic anisotropy arises when crystals of the material (which themselves are anisotropic) are brought into alignment by the macroscopic strain or other processes. Extrinsic anisotropy arises from material heterogeneities, which can also be aligned through stress and strain. Here, we describe the material properties of ice, in particular the electrical properties, as well as when and how ice can exhibit permittivity anisotropy (which means that electromagnetic waves travel with different speeds, phase variations, and loss in different directions through the medium). Throughout, we use ϵ (with any combination of subscripts and superscripts) to denote the *relative* permittivity. The full permittivity can be obtained by multiplying the relative permittivity by the permittivity of free space, ϵ_0. ϵ has both real and imaginary components, that is, $\epsilon = \epsilon' + i\epsilon''$. We discuss the potential for anisotropy in each but focus on the real component that modulates the wave speed in the medium.

2.1. Intrinsic Anisotropy

2.1.1. Individual Crystal Properties

Glacial ice is a polycrystalline aggregate of individual ice Ih (Pauling, 1935) grains. Each water molecule forms four hydrogen bonds in a tetrahedron. Three of the four bonds tessellate in a hexagonal lattice within the basal plane. The fourth bond is perpendicular to the basal plane in the direction of the crystal *c* axis, which is the axis of hexagonal symmetry. This crystal structure causes anisotropy in the mechanical, thermal, and electrical properties: (a) ice shears most readily when the *c* axis is parallel to the shear-plane normal (Shoji & Langway, 1988), (b) elastic waves propagate slowest when polarized parallel to the *c* axis (Maurel et al., 2015) (c) ice is most thermally conductive along the *c* axis (Landauer & Plumb, 1956), and (d) electromagnetic waves propagate slowest (greatest permittivity) when polarized parallel to the *c* axis (Fujita et al., 1993; T. Matsuoka et al., 1997). The thermal conductivity and dielectric permittivity (second rank tensors) and elastic (fourth rank tensor) anisotropies are uniaxial (Nye, 1985), but whether the viscous anisotropy is uniaxial or has some additional variation within the basal plane is still unclear (Kamb, 1961; Qi et al., 2019).

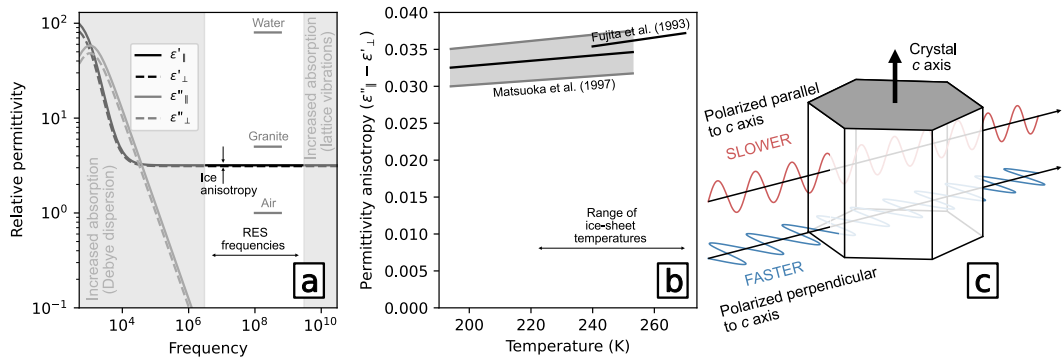

Figure 2. Summary of laboratory measurements for ice-crystal permittivity anisotropy. (a) Relative permittivity across radio frequencies in and above the high-frequency tail of Debye dispersion (Fujita et al., 2000). (b) Temperature dependence of permittivity anisotropy (Fujita et al., 1993; T. Matsuoka et al., 1997). (c) Illustration of polarized waves propagating through an ice crystal.

The ideal frequency band for radar to propagate large distances through ice is from HF to UHF ($\sim 10^6$–10^9 Hz) where ice has an absorption gap between Debye dispersion and lattice vibration (Figure 2) (Fujita et al., 2000; Warren, 1984). Within this absorption gap, permittivity has little dependence on frequency (no dispersion), but there is dependence on propagation direction relative to the crystal orientation. For a single ice crystal with c-axis aligned in the vertical direction, the permittivity tensor is

$$\epsilon_{ij} = \begin{bmatrix} \epsilon_\perp & 0 & 0 \\ 0 & \epsilon_\perp & 0 \\ 0 & 0 & \epsilon_\parallel \end{bmatrix}, \tag{1}$$

where $\epsilon_\perp$ is the permittivity for a wave polarized perpendicular to the c axis, $\epsilon_\parallel$ is the permittivity for a wave polarized parallel to the c axis, and their difference is the magnitude of permittivity anisotropy in an individual crystal,

$$\Delta\epsilon_c = \epsilon_\parallel - \epsilon_\perp. \tag{2}$$

For an arbitrarily oriented single crystal, Equation 1 can be rewritten,

$$\epsilon_{ij} = (2\epsilon_\perp + \epsilon_\parallel)\frac{\delta_{ij}}{3} + \Delta\epsilon_c\left(c_i c_j - \frac{\delta_{ij}}{3}\right), \tag{3}$$

where δ_{ij} is the identity matrix and c_i is the c-axis vector.

Since ice is a poor conductor, non magnetic, and non dispersive, the real component of permittivity determines the wave velocity in the ice

$$v = \frac{v_{\text{fs}}}{\sqrt{\epsilon'}}, \tag{4}$$

where v_{fs} is the free-space velocity. Anisotropy in the real component is ~0.034 ($\epsilon'_\parallel - \epsilon'_\perp = 3.173 - 3.139$) (Fujita et al., 1993; T. Matsuoka et al., 1997). In other words, pure ice is up to ~1% anisotropic in wave speed ("birefringent") at radio frequencies, so polarized waves can exhibit up to 1-wavelength phase delay per 100 wavelengths propagated distance (e.g., ~35 wavelengths delay for two-way propagation of a 300 MHz wave through 1 km of ice, or ~0.35 wavelengths for 3 MHz). The difference in wave speed is maximized for waves polarized parallel and perpendicular to the "optic axis" (defined as the direction with no birefringence, i.e., the crystal c axis). The magnitude of anisotropy in the full permittivity spectrum has some dependence on both

frequency and ice temperature (Fujita et al., 2000), but their dependence is too small to affect radar polarimetry in most cases, so neither are considered here (for all examples below we assume constant $\Delta\epsilon_c = 0.034$).

The imaginary component, ϵ'', partially determines the wave attenuation through electrical conductivity

$$\sigma = 2\pi f \epsilon_0 \epsilon'' + \sigma_{\mathrm{DC}}, \tag{5}$$

where $2\pi f$ is the angular frequency and σ_{DC} is the electrical conductivity at the low frequency limit. T. Matsuoka et al. (1997) found that ϵ'' has some anisotropy in the high-frequency tail of Debye dispersion (tested at 1 MHz), but none in their higher frequency tests (39 GHz). There are few other constraints on attenuation anisotropy, so we limit the discussion of this topic to Section 6.1.1 and suggest it as a point of focus for future studies.

2.1.2. Polycrystalline Ice

The bulk anisotropic properties of polycrystalline ice are the collective characterization of the anisotropy and distribution of individual ice crystals (henceforth "crystal orientation fabric"; COF). Some studies have used analogous terms to describe the same COF distribution, including "ice fabric," "crystallographic preferred orientation" (CPO), "lattice-preferred orientation" (LPO), or occasionally "texture." Since *c*-axis orientations evolve toward preferred directions as ice flows, the bulk properties of the ice are often anisotropic (with the COF principal axes representing the averaged collective distribution of all included *c* axes). Measured or modeled COFs can therefore be used to interpret ice-flow history (Lilien et al., 2021; Llorens et al., 2022) with some limitations (Hunter et al., 2023) and can help predict future ice-flow behavior caused by COF-induced mechanical anisotropy (Ma et al., 2010; Rathmann & Lilien, 2021). Here, we give a brief overview of the mechanisms for COF evolution in ice sheets to contextualize the radar polarimetry interpretations that follow in Section 5. However, we point out that this COF review is not meant to be comprehensive and refer the interested reader toward other dedicated reviews (e.g., Faria et al., 2014a; Hudleston, 2015).

Following the literature, we characterize the COF using the second-order orientation tensor $a_{ij}^{(2)}$, defined as the simple average outer product of grain *c*-axis orientations weighted by grain size, $a_{ij}^{(2)} = \langle c_i c_j \rangle$. The orientation tensor description of COF was introduced to glaciology for ice-flow modeling (Gödert, 2003) but $a_{ij}^{(2)}$ is now the standard description of COF in glaciology and ice-core science. The second-order orientation tensor provides statistical information about the COF, but it does not describe it uniquely, since it is only one moment of the underlying distribution. However, polarimetric radar is thought to be sensitive only to $a_{ij}^{(2)}$ and not other properties of the *c*-axis distribution (Rathmann, Lilien, et al., 2022), so it is a complete and convenient description of the COF for present purposes. The eigenvalues of $a_{ij}^{(2)}$, $\lambda_1, \lambda_2, \lambda_3$, are important measures of COF anisotropy that can be understood as the variance of the *c*-axis distribution projected onto the principal directions of $a_{ij}^{(2)}$ (Figure 3). In this manuscript, we follow conventional radar notation, where the three eigenvalues are ordered $\lambda_1 < \lambda_2 < \lambda_3$, and sum to one by definition ($\lambda_1 + \lambda_2 + \lambda_3 = 1$). Note that this convention is opposite to what is used in ice core analyses, where λ_1 is the largest eigenvalue, which can be a point of confusion (e.g., Fitzpatrick et al., 2014).

The evolution of COFs depends on stress, deformation (strain and rigid-body rotation), and thermal regime (Alley, 1988), so a COF is a result of depositional environment, and deformation and thermal histories. Meteoric ice is deposited as snowflakes, typically with approximately random orientation at the ice-sheet surface. Seasonal and inter-annual changes in deposition can create some anisotropy near the surface (Calonne et al., 2017; Fujita et al., 2014), but stronger anisotropy develops as ice flow reorients grains over time. In cold environments with low deviatoric stress, such as near ice domes and divides, the dominant mechanism of COF evolution is lattice rotation, characterized by no mass exchange between grains as they deform. Deformation is generally a superposition of rigid body rotation, where grains rotate together, and viscoplastic stretching, where intragrain slip causes a relative rotation of grain *c*-axes to accommodate strain (Svendsen & Hutter, 1996). Basal plane glide is much easier than other intragrain slip systems, so grain *c*-axes tend to align with the normal of the bulk shear plane, which is well-captured by director method models (Richards et al., 2021; Svendsen & Hutter, 1996) as well as more sophisticated visco-plastic self-consistent modeling (e.g., Castelnau et al., 1996) and full-field modeling (e.g., Chauve et al., 2024). More generally, lattice rotation causes grains to rotate away from the axis of maximum extension and toward compression (Alley, 1988). Therefore, in unconfined (uniaxial) compression, such as near

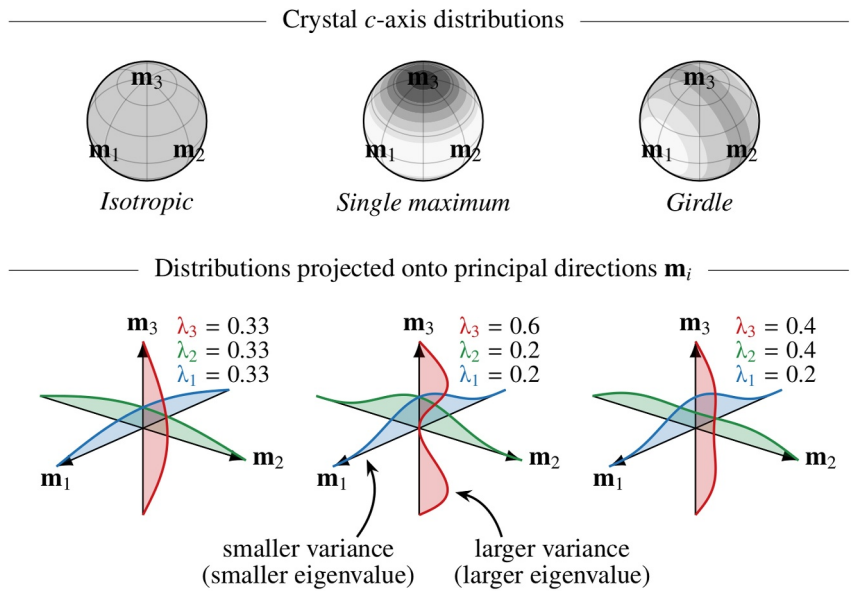

Figure 3. Interpretation of crystal orientation fabric (COF) eigenvalues for three idealized *c*-axis distributions that are resolvable with polarimetric radar: isotropic, single maximum, and girdle. Posing $a_{ij}^{(2)}$ in its principal frame has a similar interpretation as in principal component analysis: the first principal component (eigenvector $\mathbf{m}_3$) is the direction that maximizes the variance (eigenvalue λ_3) of the projected distribution (red curve), the second component is the direction orthogonal to the first component that maximizes the variance of the projected distribution (eigenvalue λ_2), and so on. Distributions with more complicated structure have been observed in glacial ice (e.g., cone and double maxima COF Jackson & Kamb, 1997; Jacka & Maccagnan, 1984), but electromagnetic waves are only sensitive up to the complexity shown here (i.e., $a_{ij}^{(2)}$) which represents the space of single-maximum and girdle COFs.

ice domes, the expected COF is a single maximum that aligns with the vertical axis of compression ($\lambda_x \approx \lambda_y \ll \lambda_z$; Figure 3). In partially confined compression, such as near ice divides, the expected COF is a vertical girdle that aligns with the divide ($\lambda_x \ll \lambda_y \approx \lambda_z$, assuming divergence across the divide in the x direction).

Multiple forms of recrystallization—a family of processes that move mass between ice grains—can also influence COF development (Faria, 2006a, 2006b). Laboratory (e.g., Journaux et al., 2019; Qi et al., 2019) and in situ (e.g., Gerbi et al., 2021; Weikusat et al., 2017a) observations indicate that, of these processes, migration recrystallization has the strongest effect on COF development. In this process, grains with small dislocation density tend to nucleate and grow, consuming older, more strained grains with higher dislocation density, thus shifting the mass-averaged orientation of *c* axes (De La Chapelle et al., 1998). In warm or temperate environments, such as in basal ice or in ice-stream shear margins, migration recrystallization may dominate over lattice rotation and cause substantially faster reorganization of the COF to match the local stress and deformation (Fan et al., 2020; McCormack et al., 2022). The rate of migration recrystallization is highly variable and believed to depend primarily on ice temperature, dislocation density, and stress state (Chauve et al., 2024; Faria et al., 2014b), though in some models this complexity is reduced to a linear or Arrhenius-type activation function of temperature alone (Lilien et al., 2023; Richards et al., 2021). Recrystallization can lead to more complicated COFs, such as those with multiple maxima (Gow & Williamson, 1976), but since radio waves are only sensitive to $a_{ij}^{(2)}$ those are not be resolvable with radar methods.

Natural ice-sheet COFs have been directly observed, typically near ice domes and divides where most deep ice cores have been drilled (e.g., Weikusat et al., 2017a; Zichu, 1985), but also in streaming ice (e.g., Stoll et al., 2025) and active shear zones (e.g., Gerbi et al., 2021; Jackson & Kamb, 1997; Monz et al., 2021). Samples of natural ice are important because there is likely a strain-rate dependence (Hunter et al., 2023; Piazolo et al., 2013) that cannot be reproduced in laboratory experiments, which complicates their applicability to natural settings (Richards et al., 2023). More measurements, field samples, laboratory, and modeling work are needed to better constrain models of COF evolution (Rathmann et al., 2025), particularly at flank-flow locations as most ice

cores and thus direct COF sampling happen near the dome or divide of the ice sheets. Polarimetric radar can provide one such source of information.

2.2. Extrinsic Anisotropy

Ice often contains air, water, or chemical impurities, so it is sometimes best described as mixed media rather than a perfect polycrystal. The permittivity of ice is notably greater than that of air and less than that of other Earth materials (e.g., granite) or water (Peters et al., 2005). Therefore, when the discontinuities in the polycrystal are not homogeneous they can cause anisotropy in the bulk properties.

Microscale extrinsic anisotropy may occur when interstitial spaces in the ice (e.g., bubbles) or the ice crystals themselves (and therefore the air- or water-filled junctions as well) are somehow directional or elongated (Drews et al., 2012). Near-surface snow and firn contain connected air-filled pore spaces. These tend to develop a preferential vertical elongation during snow metamorphism, causing vertical dielectric anisotropy (Fujita et al., 2009; Lytle & Jezek, 1994). Encapsulated air bubbles exist down through the clathrate transition at ∼500–1,500 m (Kipfstuhl et al., 2001), and even in clathrate ice, some water- or air-filled space still exists at the triple junction between ice crystals (Raymond & Harrison, 1975). Elongation of these encapsulated bubbles can be induced by rapid ice deformation (Alley & Fitzpatrick, 1999).

The more apparent form of macroscale extrinsic anisotropy is in crevasses, whether they be air- or water-filled. Since crevasses are a feature of the strain field, they align with the extensional axis (Harper, 1993; Meier et al., 1974) and are therefore naturally anisotropic. However, crevasses are often larger than or comparable to the radar wavelength, so they can cause scattering and make the anisotropy signal harder to retrieve using radar sounding methods.

There can also be some polarization dependence to the way radar energy scatters from englacial or subglacial interfaces that are rough at scales from a fraction of the wavelength to hundreds of wavelengths, analogous to polarization change at scattering surfaces in satellite remote sensing (Zebker & Van Zyl, 1991). Englacial scattering interfaces are commonly flat and specular at the scale of the radar wave (with little or change in polarization), but they can be folded and rough in dynamic regions (Hudleston, 2015; Jennings & Hambrey, 2021), for instance, in an ice-stream shear margin (Holschuh et al., 2019). The ice-bed interface itself can display directionally varying roughness, likely due to glacial erosion (Cooper et al., 2019; Holschuh et al., 2020). There can also be directionality in water routing of the englacial and subglacial hydrologic systems (Flowers, 2015), again potentially resolvable by radar systems (Scanlan et al., 2022; Schroeder et al., 2016).

3. Theory: Wave Propagation Through Anisotropic Media

The behavior of a wave propagating through anisotropic media depends on its polarization relative to the axes of anisotropy. For most cases, this orientation dependence makes it difficult to interpret radar polarimetry measurements qualitatively, so mathematical models are used as a guide (e.g., Fujita et al., 2006; Rathmann, Lilien, et al., 2022). Although there can be many model implementations, we choose to focus our examples on a layered *Jones*-matrix model for vertically propagating ($\theta = 0$) plane waves (Ulaby & Elachi, 1990) since it is relatively straightforward to understand and currently the most widely adopted model in the glaciology literature (Fujita et al., 2006). In this section, we start by reviewing the assumptions (Section 3.1) and underlying framework (Section 3.2) for that model, sequentially adding descriptions of transfer functions for anisotropic transmission (Section 3.3), scattering (Section 3.4), and both together (Section 3.5). Embedded throughout are a series of progressively more complicated synthetic examples (reproducible following Hills, 2025), with references to how this model and similar have been used in the literature. Finally, the section ends with 3.6 by noting some alternatives to the Jones-matrix model which are applicable to obliquely propagating waves (i.e., with $\theta \neq 0$) and arbitrary COFs (i.e., not limited to those with one eigenvector oriented vertically). The notation used throughout is given in Table 1 and Figure 4.

3.1. Effective Medium Approximation

We make an *effective medium* approximation (Choy, 2015) by assuming that the wave propagation depends on bulk dielectric anisotropy rather than the anisotropy of each individual crystal. This assumption holds for intrinsic

Table 1
Variable Definitions

Variable symbol	Variable description
x, y, z	Spatial dimensions
t	Time
θ	Polar angle
ψ	Azimuth angle
δ_{ij}	Identity matrix
c_i	c-axis vector
$a_{ij}^{(2)}$	Second-order orientation tensor
$\lambda_i\ (i = 1,2,3)$	Eigenvalue of $a_{ij}^{(2)}$
$\lambda_j\ (j = x,y,z)$	Eigenvalue of $a_{ij}^{(2)}$, assuming that one is vertically oriented
$\Delta\lambda$	Difference of horizontal eigenvalues
$\mathbf{E}$	Electric field Jones vector
$\mathbf{J}$	Arbitrary Jones matrix
$\mathbf{R}$	Rotation Jones matrix
$\mathbf{T}$	Transmission Jones matrix
$\mathbf{\Gamma}$	Scattering Jones matrix
r	Reflection ratio
N	Number of layers in the Jones-matrix model
ϵ	Relative permittivity (real component unless otherwise noted)
$\epsilon_\perp, \epsilon_\parallel$	ϵ for waves polarized perpendicular and parallel to the c axis, respectively
$\Delta\epsilon_c$	Magnitude of permittivity anisotropy for an individual ice crystal
$\Delta\epsilon$	Magnitude of permittivity anisotropy for the bulk ice
σ	Electrical conductivity
k	Angular wavenumber
f_c	Center frequency
v	Wave velocity
τ	Travel time
ϕ	Phase
γ	Rotation of polarization ellipse
A	Wave amplitude
Ω	Beat frequency
L	Beat wavelength
H, V	Horizontally and vertically polarized wave components, respectively
$\mathbf{s}$	Measured waveform; vector (range)
$\mathbf{S}$	Measured waveform; matrix (range × azimuth)
C	Coherence
Ξ_ϕ	Phase uncertainty

Note. Some variables are only defined in the text.

and microscale extrinsic anisotropy, since radar wavelengths in ice (~cm to m) are longer than a typical ice crystal or air bubble (~mm to cm). If grain size and orientation are uncorrelated, the *effective* permittivity is then the grain average of the single-crystal permittivity in Equation 3 (Bussemer et al., 1991),

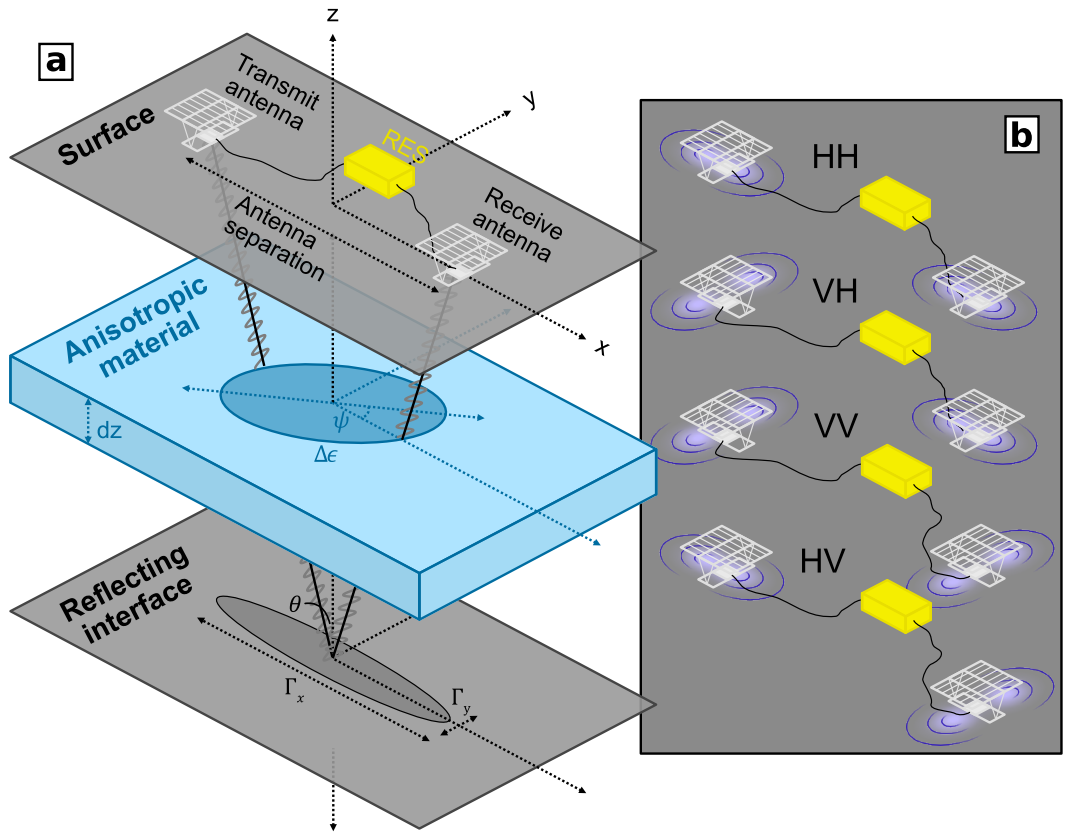

Figure 4. (a) Symbol notation and survey geometry used for the model scenarios throughout Section 3. The illustrated design is for a ground-based radar, but the same notation could be used for an airborne system with some altitude above the ice surface. (b) The four distinct transmit-receive antenna pairings used in a quad-polarization survey (see Appendix A).

$$\langle \epsilon_{ij} \rangle = \epsilon_{\perp} \delta_{ij} + \Delta\epsilon_c a_{ij}^{(2)}. \tag{6}$$

In a perfectly isotropic polycrystal ($\lambda_i = 1/3$, i.e. $a_{ij}^{(2)} = \delta_{ij}/3$) the effective permittivity is the same in all directions, so $\langle \epsilon_{ij} \rangle = \left(\frac{1}{3}\epsilon_{\parallel} + \frac{2}{3}\epsilon_{\perp}\right)\delta_{ij}$.

In some cases, the effective medium approximation can also be made for extrinsic, inter-granular features such as water-filled veins or air-filled bubbles, but only if the features are small compared to the radar wavelength (large crevasses cause anisotropic scattering and generally cannot be considered part of an effective medium with the bulk ice). The mixed-media permittivity anisotropy depends on the relative permittivity of ice and whatever fills the void space, as well as the shape, distribution, and total volume fraction of voids. There are many relevant mixing formulas (Sihvola, 2000); for example, the popular Maxwell Garnett (1904) approximation has a form for aligned ellipsoids which is relevant here,

$$\epsilon_{\mathrm{mix},ij} = \epsilon_{\mathrm{ice}}\delta_{ij} + \nu\epsilon_{\mathrm{ice}}\frac{\epsilon_{\mathrm{void}} - \epsilon_{\mathrm{ice}}}{\epsilon_{\mathrm{ice}} + (1-\nu)\zeta_{ij}(\epsilon_{\mathrm{void}} - \epsilon_{\mathrm{ice}})}, \tag{7}$$

where ν is the volume fraction of voids in the ice, and ζ_{ij} is a depolarization factor for the ellipsoidal voids. Taylor (1965) considered additional void shape distributions and in lossy media which may be more appropriate in the glaciological setting. Equation 7 assumes that the ice itself is isotropic, that is, $\epsilon_{\mathrm{ice}} = \frac{1}{3}\epsilon_{\parallel} + \frac{2}{3}\epsilon_{\perp}$, but both intrinsic and extrinsic anisotropy can be considered together if desired (Sihvola, 2000).

Whether from intrinsic or extrinsic anisotropy, the bulk ice is generally an optically biaxial medium and its effective permittivity tensor forms a permittivity ellipsoid (often described in terms of the corresponding

refractive indices as the "indicatrix" or "index ellipsoid"; Bain, 2019). The extent to which the material anisotropy is expressed dielectrically depends on the cross section of the permittivity ellipsoid that is perpendicular to the wave propagation direction. Most radar sounding surveys use nearly collocated transmit and receive antennas, so we focus discussion on vertically propagating waves whose polarization bisects the permittivity ellipsoid in the x-y plane. Then, x-y anisotropy (e.g., a vertical girdle or horizontal single maximum COF) is most relevant to what can be measured by the radar, and it becomes useful to reference in the principal frame where $a_{ij}^{(2)} = \mathrm{diag}(\lambda_x, \lambda_y, \lambda_z)$. Now, the difference in permittivity between the two horizontally eigenpolarized waves is

$$\Delta\epsilon_{\mathrm{COF}} = \Delta\epsilon_c(\lambda_y - \lambda_x), \tag{8}$$

with no dependence on the vertical eigenvalue, λ_z. The extrinsic, mixed-media case also depends only on the horizontal anisotropy in the eigenframe,

$$\Delta\epsilon_{\mathrm{mix}} = \epsilon_{\mathrm{mix},yy} - \epsilon_{\mathrm{mix},xx}. \tag{9}$$

3.2. The Polarization Ellipse

The polarization of a wave can change as it propagates through an anisotropic material ("depolarization" is a common term within the radioglaciology literature, but we avoid it here for potential confusion with the side-looking radar remote sensing literature). Before discussing how that happens in the coming sections, it is first useful to give a framework with which to represent a single polarization state. For a plane wave, the complex electric field amplitude can be described as a Jones vector (Collett, 2005),

$$\mathbf{E} = \begin{bmatrix} A_x e^{i(k_x z + \phi_x)} \\ A_y e^{i(k_y z + \phi_y)} \end{bmatrix} e^{-i\omega t}, \tag{10}$$

where A is the wave amplitude, k is the angular wavenumber, ϕ is a phase angle, and there are two wave components, $\mathbf{E} = \begin{bmatrix} H \\ V \end{bmatrix}$, where H is the horizontal and V the vertical component. Despite the terminology, both wave components propagate in the same direction (typically assumed vertically through the ice column, i.e., in the z direction with $\theta = 0$, as before) and with polarization perpendicular to the propagation direction (in the x-y plane for horizontal reflectors). At any depth, z, the components of the electric field vector can be combined to yield the equation for an ellipse (Ulaby & Elachi, 1990) traced out over time, $t = 2\pi/\omega$. The wave is therefore *elliptically* polarized. The shape of this polarization ellipse can be described with two variables, the phase delay and rotation, which we will use for conceptualization in the coming examples (see Appendix C for additional detail).

The ellipse phase delay is

$$\phi_{\mathrm{ellipse}} = \arg(H \cdot V^*) = (k_x z + \phi_x) - (k_y z + \phi_y), \tag{11}$$

where * is the complex conjugate. If $k_x \neq k_y$ then the phase delay changes with propagated distance since the two wave components have different velocity (analogous to the "ordinary" and "extraordinary" waves in uniaxial materials). At integer multiples of π ($\phi_{\mathrm{ellipse}} = n\pi$) the wave components are synchronized and the equation for the ellipse reduces to a straight line (*linear* polarization).

The ellipse rotation describes the relative amplitude of measured signals, H and V,

$$\gamma = \tan^{-1}\left(\frac{|V|}{|H|}\right) = \tan^{-1}\left(\frac{A_y}{A_x}\right). \tag{12}$$

Take an incoming wave that is initially horizontally polarized, at $|H| = 1$ the wave polarization is unrotated (linear polarization in the x direction) and at $|V| = 1$ it is fully rotated (linear polarization in the y direction). In the unique case that $|H| = |V|$ and $\phi_{\mathrm{ellipse}} = \pi/2$ the electric field traces a perfect circle (circular polarization).

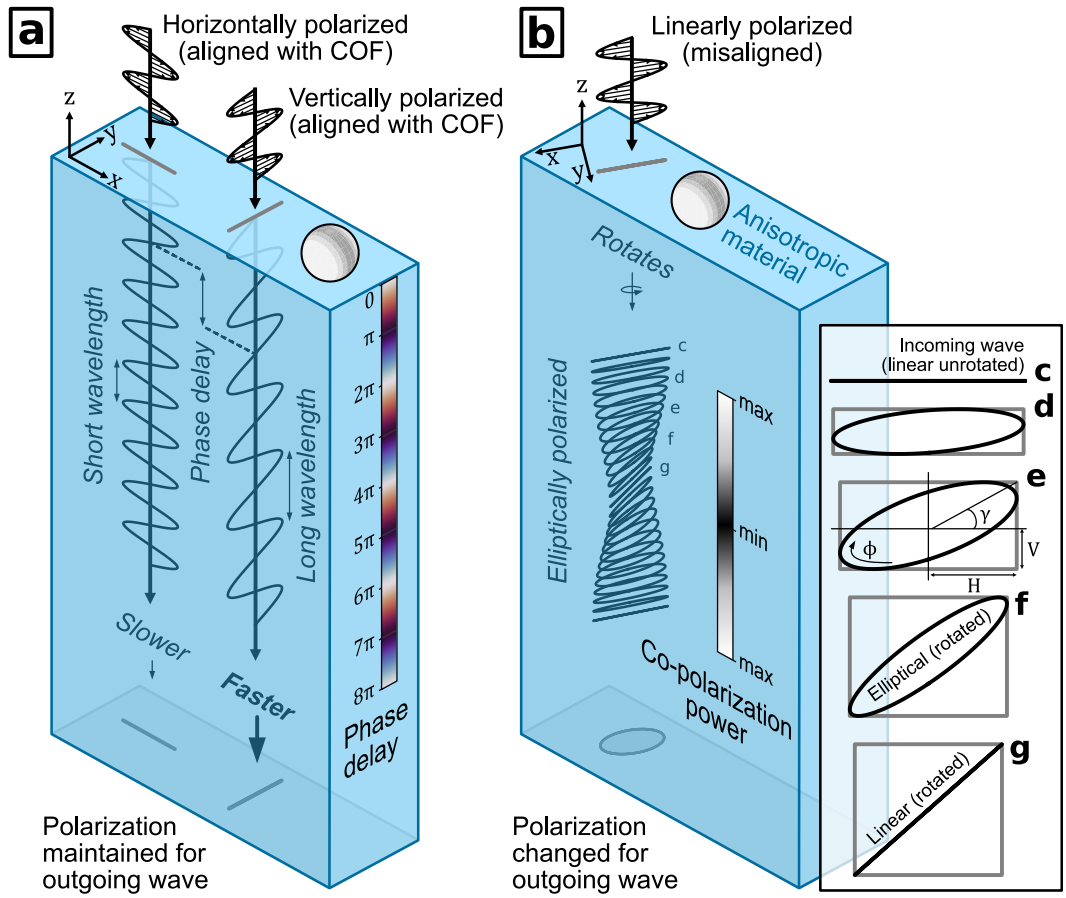

Figure 5. Wave propagation through anisotropic ice. (a) When the transmitted wave polarization is parallel to one of the COF principal axes it maintains its polarization, but wave propagation is faster for polarization along the principal axis with the lower eigenvalue, causing a phase delay between waves. (b) When the wave polarization is misaligned from the material anisotropy, its polarization changes with propagated distance through the material (the birefringent beat signature), and the outgoing wave is elliptically polarized. (c)-(g) The polarization ellipse at any point along the propagation path is defined by a phase delay, ϕ, and a rotation, γ, here shown relative to the orientation of the initial wave polarization. Note that the coordinate reference frame is defined relative to the radar system geometry (as in Figure 4a) so is different between panels (a) and (b), but the material anisotropy is the same for each (visualized here with *c*-axis distributions as in Figure 3).

The polarization state, $\mathbf{E}$, changes as the wave propagates through or scatters from anisotropic media. Mathematically, this change is represented with a transform function which, for this model, is a Jones matrix, $\mathbf{J}$, such that

$$\mathbf{E}_{\text{out}} = \mathbf{J}\mathbf{E}_{\text{in}}, \tag{13}$$

where $\mathbf{E}_{\text{in}}$ is the incoming and $\mathbf{E}_{\text{out}}$ is the outgoing complex electric field, each represented as a Jones vector as in Equation 10. Here, $\mathbf{J}$ can represent any sequence of transmission and scattering.

3.3. Anisotropic Transmission (Birefringence)

When a polarized wave propagates through an anisotropic medium, the polarization ellipse changes shape with propagated distance. Consider one-way transmission through a single uniform layer with no attenuation or scattering (Figures 5 and 6). This process can be described by the Jones matrix

$$\mathbf{J}_{\text{transmission}} = \mathbf{R}\mathbf{T}\mathbf{R}', \tag{14}$$

where

10.1029/2024RG000842

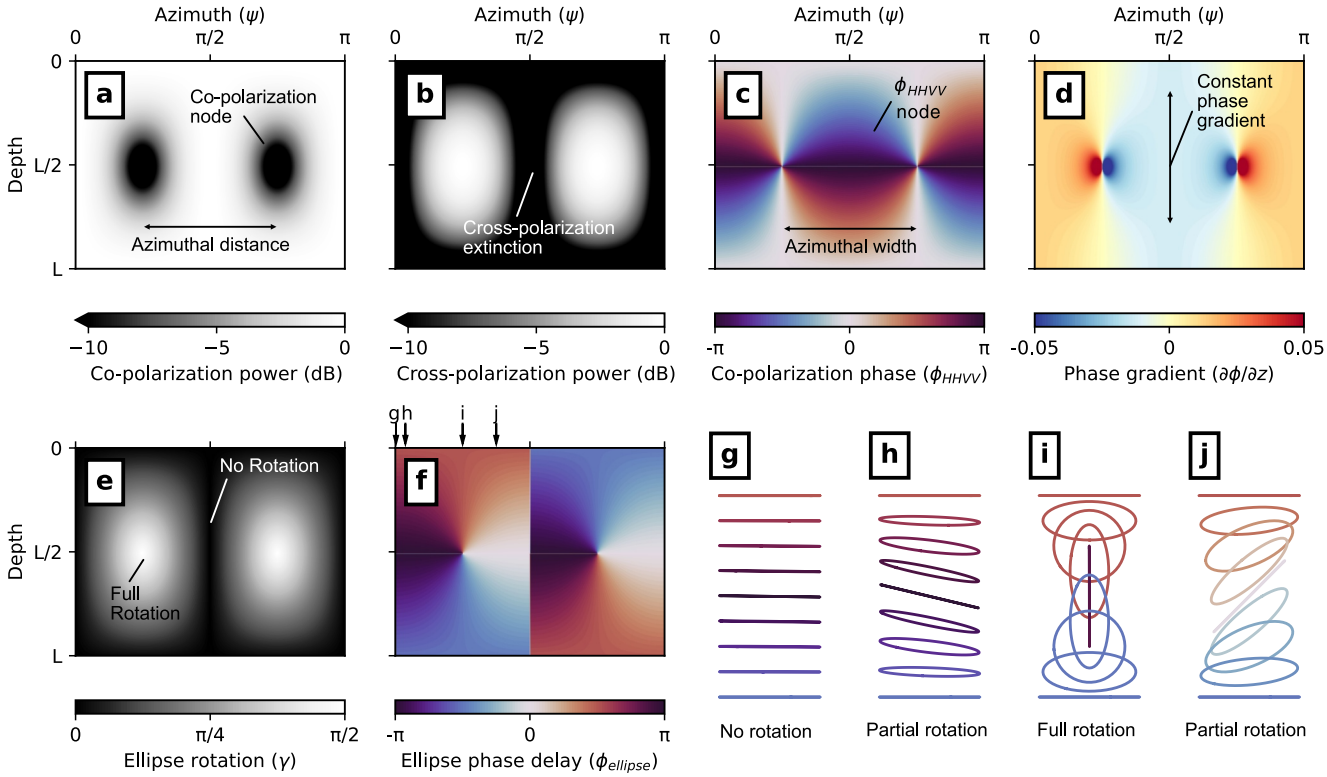

Figure 6. Modeled wave polarization for an idealized vertical girdle with principal axes at 0 and $\pi/2$, following Fujita et al. (2006). The plotted depth is between the ice surface, 0, and one beat wavelength, L. The (a) co-polarization power, (b) cross-polarization power, (c) co-polarization phase delay, and (d) co-polarization phase gradient have been shown in prior studies (Fujita et al., 2006; see also Ershadi et al., 2022; Jordan et al., 2019; Jordan, Schroeder, et al., 2020). We also show the (e) rotation and (f) phase delay of the polarization ellipse to demonstrate change in polarization as in Equations 11 and 12, respectively. (g–j) Visualizations of the polarization ellipse at azimuths shown by arrows in (f). For each, the wave starts linearly polarized but the amount of rotation depends on the azimuth angle relative to the principal axes in the ice.

$$\mathbf{R} = \begin{bmatrix} \cos(\psi) & -\sin(\psi) \\ \sin(\psi) & \cos(\psi) \end{bmatrix} \tag{15}$$

is counterclockwise rotation by ψ, the angle between the principal axis of the medium (λ_x) and the incoming wave polarization, and

$$\mathbf{T} = \begin{bmatrix} T_x & 0 \\ 0 & T_y \end{bmatrix} \tag{16}$$

is the transmission matrix which has different terms for transmission in each polarization, $T_i = e^{i(k_i - k_0)z}$. The permittivity anisotropy shows up here, where each component of the transmission matrix has some dependence on the effective permittivity for that orientation through its respective wavenumber, $k_i(\epsilon)$ (Fujita et al., 2006).

Using Equation 14, first consider perfect alignment of the radar antenna with a principal axis of the ice (ψ at integer multiples of π) (Figure 5a). In this case, the rotation matrix is equal to plus or minus the identity matrix, so none of the energy is rotated between x/y directions and γ is constant. Without rotation, the Jones matrix has no off-diagonal terms, $\mathbf{J}_{\text{transmission}} = \begin{bmatrix} T_x & 0 \\ 0 & T_y \end{bmatrix}$, operating on each wave component independently. Then, if the input wave is linearly polarized, one component is zero and the non-zero component maintains its polarization (Figure 6g). If the input wave is elliptically polarized, the component parallel to the permittivity maximum (i.e., in line with the most crystal c axes) travels slower than the perpendicular component, changing the phase of the

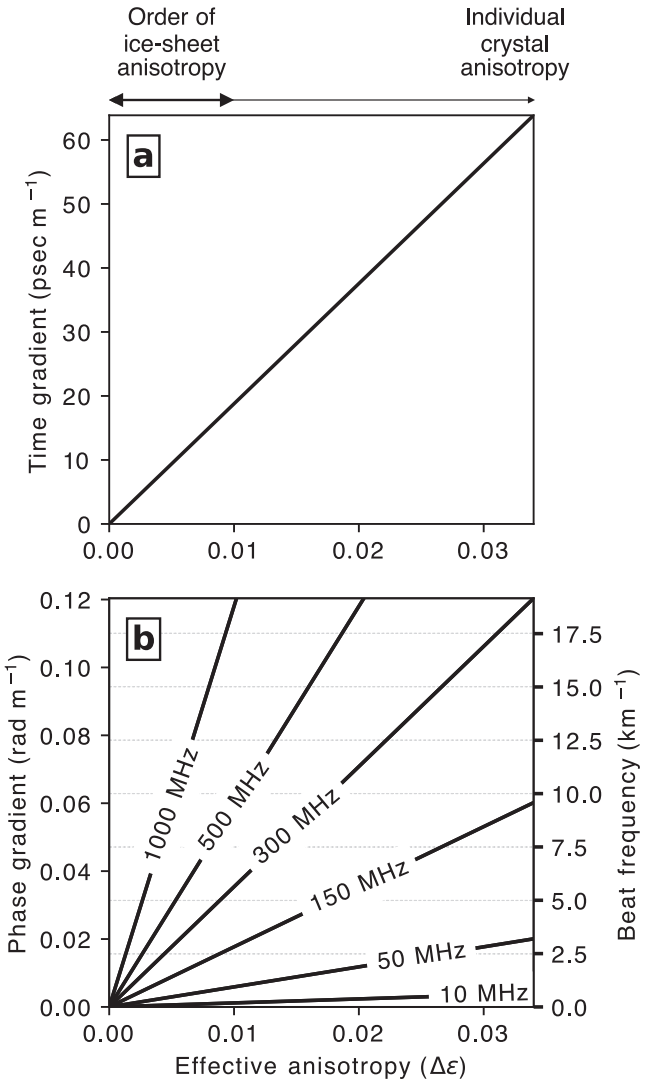

Figure 7. Measurable radar signals across the range of possible COF anisotropy from 0 (isotropic) to the crystal anisotropy. (a) Time gradient from Equation 18. (b) Phase gradients from Equation 20 and beat frequencies from Equation 21. Phase gradient and beat frequency are dependent on the center frequency of the radar, f_c, so several representative radar frequencies are given between 10 and 1,000 MHz.

ellipse, ϕ_{ellipse}, but still the ellipse rotation goes unchanged (no energy moving between H and V). This logic also holds at $\psi = \pi/2$, with a flipped transmission matrix (i.e., perpendicular and parallel components reversed).

Although perfect alignment can never be achieved in a real setting, alignment can be sufficiently precise to give rise to two measurable phenomena. First, without rotation, there is no (or minimal) birefringent power loss. A horizontally polarized wave emitted at the ice surface remains horizontally polarized and is not measurable by a vertically polarized receive antenna. The axis of anisotropy can therefore be determined based on this angle, termed the azimuth of cross-polarization extinction (XPE, Figure 6b). Second, the magnitude of anisotropy can be inferred based on the delay in two-way travel time between two waves (or wave components). Generally, this delay is most apparent between two co-polarization acquisitions that are perpendicular to one another and aligned with the horizontal eigenvectors. For example, the expected time delay between one acquisition with H-polarized transmit and H-polarized receive (denoted HH as in Appendix A) and a second acquisition, VV, is (Figure 7)

$$\tau_{HHVV} = \frac{2}{v_{\text{fs}}}\int_{z_0}^{z}\left(\sqrt{\epsilon_y(z)} - \sqrt{\epsilon_x(z)}\right)dz, \tag{17}$$

where the permittivity anisotropy is integrated from the surface, z_0, to arbitrary depth z and with a factor of 2 to account for return to the surface. In this hypothetical case with no rotation, the phase delay is *linearly* related to the magnitude of x/y anisotropy and the two-way propagated distance. For small deviations (relative to the radar wavelength) about a mean (polarization-averaged) permittivity (i.e., assuming $\epsilon = (\epsilon_x + \epsilon_y)/2$, which may only hold in certain cases), Equation 17 can be expressed through a first-order Taylor expansion following Jordan et al. (2019, Equation 12) as

$$\tau_{HHVV} = \frac{1}{v_{\text{fs}}}\int_{z_0}^{z}\frac{\Delta\epsilon(z)}{\sqrt{\epsilon}}dz, \tag{18}$$

where $\Delta\epsilon$ is the magnitude of anisotropy that the wave is subjected to by the bulk ice, whether that be intrinsic or extrinsic. Considering vertically propagating plane waves, $\Delta\epsilon$ can only change in z and ϵ is generally assumed constant. In phase-coherent radar systems, the delay between waves can be measured precisely based on the complex coherence between acquisitions (Dall, 2010; Lee et al., 1994)

$$C_{HHVV} = \frac{HH \cdot VV^*}{|HH||VV|}. \tag{19}$$

The magnitude of coherence, $|C_{HHVV}|$, gives the correlation strength between acquisitions. The phase delay between co-polarization acquisitions is $\phi_{HHVV} = \arg(C_{HHVV})$ (analogous to Equation 11). Then, this is related to Equation 18 by

$$\phi_{HHVV} = 2\pi f_c \tau_{HHVV} \tag{20}$$

where f_c is the instrument center frequency (Figure 7b).

Now consider a wave propagating vertically but with the polarization out of alignment from the principal axes (Figure 5b). In this case, the two components of the wave which are aligned with the principal axes have different

velocity, causing a rotation of the polarization, γ, with propagated distance (Figures 6h–6j). Rotation brings the now elliptically polarized wave in and out of alignment with the receive antenna at a regular timing called the "beat frequency" (or "beat signature"), an interference effect between perpendicularly polarized wave components. That frequency is calculated as the depth gradient in phase divided by 2π radians per wavelength. Within a layer of uniform anisotropy, the integral in Equation 18 reduces to $z\overline{\Delta\epsilon}$ and combining with Equation 20 the beat frequency is

$$\Omega = \frac{f_c \overline{\Delta\epsilon}}{v_{\mathrm{fs}} \sqrt{\bar{\epsilon}}}, \tag{21}$$

with units m^{-1} and where $\overline{\Delta\epsilon}$ and $\bar{\epsilon}$ are the depth-averaged dielectric anisotropy and permittivity, respectively. $L = 1/\Omega$ is the associated beat wavelength. The extent of rotation, that is, maximum change in γ, depends on the degree of misalignment from the principal axes. At maximum misalignment, $\psi = \frac{(2n+1)\pi}{4}$, the wave is *fully* rotated and a power minimum is seen in the co-polarization acquisition (node in Figure 6a). There is also no relative phase delay at this maximally misaligned azimuth since both wave components are equally misaligned from the principal axes. At intermediate azimuths the phase gradient depends on the extent of rotation, with the steepest gradients corresponding to the most rotated waves. The frequency of the beat is independent of azimuth, so in cases where: (a) the radar antennas are misaligned from the ice anisotropy, (b) the beat can be distinguished from englacial stratigraphy, and (c) the ice is sufficiently thick for multiple beats to be observed, this phenomena can be measured.

3.4. Anisotropic Scattering

Scattering at an interface can also cause a change in polarization. Similarly to Equation 14, this is represented as a rotated Jones matrix,

$$\mathbf{J}_{\mathrm{scattering}} = \mathbf{R}\boldsymbol{\Gamma}\mathbf{R}', \tag{22}$$

where

$$\boldsymbol{\Gamma} = \begin{bmatrix} \Gamma_x & 0 \\ 0 & \Gamma_y \end{bmatrix} \tag{23}$$

is the *scattering* matrix. Each of the terms can be described by the complex Fresnel reflection coefficients (Ulaby & Ravaioli, 2015), here assuming a vertically propagating wave and normal incidence,

$$\Gamma_i = \frac{\sqrt{\epsilon_{i,1}} - \sqrt{\epsilon_{i,2}}}{\sqrt{\epsilon_{i,1}} + \sqrt{\epsilon_{i,2}}}, \tag{24}$$

where ϵ_1 and ϵ_2 are the relative permittivity of the two media at the reflection interface and i denotes the direction (x, y). Unlike birefringent power losses which are periodic at $\pi/2$ (Figures 6a and 6b), scattering is periodic at π, so the two can be distinguished in that way (Fujita et al., 2003; Gerber et al., 2025).

For radar sounding, there are scattering interfaces throughout the ice column, and one particularly strong interface at the basal boundary (we reserve discussion of anisotropy at the basal interface for Section 6.1.2). Some englacial scatterers are associated with a change in permittivity anisotropy with depth (see interpretations in Section 5.2.2), so the components of the scattering matrix can be derived from Equation 24 (Paren, 1981). For example, in the case of COF boundaries, the reflection comes from a change in the real permittivity between layers (Drews et al., 2012)

$$\Gamma_i = \left| \frac{(\lambda_{i,n} - \lambda_{i,n+1})\Delta\epsilon_c}{4\epsilon} \right|, \tag{25}$$

where n is the layer above the reflecting interface and $n + 1$ below. Then, the reflection ratio, $r = \Gamma_y/\Gamma_x$, is related to the COF boundary by (Ershadi et al., 2022)

$$r = \left| \frac{\lambda_{y,n} - \lambda_{y,n+1}}{\lambda_{x,n} - \lambda_{x,n+1}} \right|. \tag{26}$$

This reflection ratio can be inferred from measurements based on either the azimuthal distance between co-polarization nodes.

$$\psi_{\mathrm{AD}} = 2\tan^{-1}\left(\frac{1}{\sqrt{r}}\right), \tag{27}$$

or the azimuthal width of phase nodes (Ershadi et al., 2022, their Appendix F). Together with the constraint that the eigenvalues sum to one, measurements of phase delay in Equation 20, and reflection ratio in Equation 27 can be used to determine all three eigenvalues explicitly (Ershadi et al., 2022). This assumes that transitions in COF are the sole source of anisotropic reflections (see Section 6.1.3 for a discussion of extrinsic contributions to anisotropic scattering), that such reflections are always produced, and that one eigenvalue is oriented vertically. However, the gradient in COF may be too smooth compared to the radar wavelength to produce a reflection, in which case this approach cannot accurately recover the vertical eigenvalue. In cases where no eigenvalue is oriented vertically, Equation 26 cannot be applied and one might consider designing a targeted survey with oblique propagation (Section 3.6).

3.5. Multi-Layer Matrix Model

Anisotropy is relatively easy to detect in the near-surface ice based on the measurable phenomena described above: the beat frequency in measured power (Young, Schroeder, et al., 2021), cross-polarization extinction (Ershadi et al., 2022), with azimuthal symmetry in the phase gradients (Jordan et al., 2022), and/or travel time differences (Zeising et al., 2023). However, if the anisotropy has some azimuthal rotation with depth (excluding the ideal case of a 90-degree rotation described by Jordan et al., 2022), any subsequent change in the orientation of the fabric becomes difficult to constrain since the wave received at the surface is an integration of path effects for all the ice through which it traveled. By the time the wave encounters the second anisotropic parcel of ice, it has changed to an elliptical polarization. The interaction of the now elliptically polarized wave with the new principal axis is in practice never such to bring it back to the original linear polarization. For these reasons, inferring anisotropy using extinction or depth-phase gradients is difficult when the principal axis rotates in depth (e.g., if a COF in the shallow ice is misoriented from a COF in the deeper ice) but can be done with careful analysis or geophysical inversion.

Now, we must expand to the full model from Fujita et al. (2006), which includes multiple layers through the ice column, with transmission and rotation through each (including both downward and upward propagation) as well as scattering at the reflection interface,

$$\mathbf{J}_N = \prod_{n=1}^{N} \left[\mathbf{R}_{N+1-n} \mathbf{T}_{N+1-n} \mathbf{R}'_{N+1-n} \right] \mathbf{R}_N \boldsymbol{\Gamma}_N \mathbf{R}'_N \prod_{n=1}^{N} \left[\mathbf{R}_n \mathbf{T}_n \mathbf{R}'_n \right], \tag{28}$$

The wave transmission effect from Equation 14 is now cumulative over all layers ($n = 1$ to N), where $\prod$ is an iterative matrix product (the first being upward propagation and the second downward). Note that the Jones matrix in Equation 13 is appended on the left-hand side of the input vector (i.e., $\mathbf{J}_N \mathbf{J}_{N-1} \cdots \mathbf{J}_2 \mathbf{J}_1$). For airborne surveys, an additional term is commonly added to Equation 28 for free-space propagation losses, $D = \frac{\exp(ik_0 z)}{4\pi z}$ (and squared for two-way losses).

This multi-layer model allows for non-uniformity through the ice column, both in the magnitude and orientation of anisotropy (e.g., Figure 8). Strengthening anisotropy behaves as may be expected, co- and cross-polarization nodes have narrowing depth separation (increasing beat frequency) and the phase-depth gradient steepens. Rotation of the principal axis is less intuitive. After a rotation, the XPE axis no longer follows the principal axis.

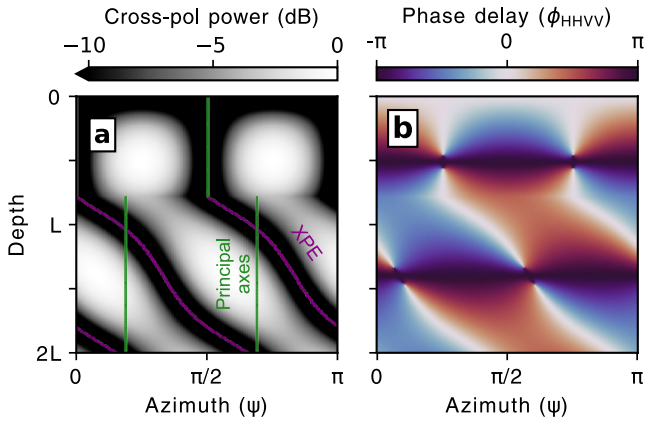

Figure 8. Jones model result for instantaneous rotation of the COF principal axes at a depth in the ice column. (a) Cross-polarization power and (b) co-polarization phase delay as in Figures 6b and 6c. The XPE axis is in magenta, and the true principal axes in green.

Instead, the cross-polarization power for the incoming wave at the azimuths of the new principal axes is maintained. No signal is rotated when aligned with the principal axis and γ is constant.

3.6. Oblique Propagation and Anisotropy Generalizability

All examples above assume vertically propagating plane waves through media with one eigenvector oriented vertically (consistent with the propagation axis), so the wave polarization and material anisotropy are restricted to the plane perpendicular to wave propagation (the *x*-*y* plane). K. Matsuoka et al. (2009) adapted the Jones-matrix model above for oblique propagation (e.g., for bistatic radars). They used rotated coordinate systems to define the appropriate transmission matrix in Equation 28 for both uniaxially and biaxially bulk media. Their interpretation focused on birefringent power losses through media with upward-oriented uniaxial anisotropy (single-maximum COF) or biaxial anisotropy (girdle COF, Figure 3), where the beat frequency depends on the obliquity of wave propagation. Yet, their model can be expanded to non-vertically oriented COFs and conserves the full complex waveform which also enables interpretation of time/phase delays (Oraschewski et al., 2025). By constraining the model to wave propagation within an eigenplane of the permittivity ellipsoid, an arbitrary number of layers can be modeled in the same way as above examples for vertical propagation (Jordan, Besson, et al., 2020; Oraschewski et al., 2025).

Although the inclusion of oblique propagation is useful, the Jones-matrix model is still limited in the range of COF anisotropies allowed. Recent work by Rathmann, Lilien, et al. (2022) further generalized the transfer matrix method to allow for arbitrary COF anisotropy as well as oblique wave propagation. They adapted a 4 × 4 transfer matrix formalism used in the optics literature (Passler et al., 2020; Yeh, 1980) as an alternative to the 2 × 2 matrices as considered in Equation 28. With this generalization, the matrix model also allows for an easier representation of nonzero off-diagonal elements in the permittivity tensor (compared to the Jones model with a rotated frame of reference) that are important when considering oblique reflection and transmission on internal interfaces (energy exchange between eigenpolarizations) (Passler & Paarmann, 2017). For radar waves propagating vertically through ice with a vertical eigenvector, this approach is equivalent to that in Equation 28, which suffices for the most common applications of polarimetric radar, but the added complexity may be necessary to interpret future data collected with alternative sensor geometries (Section 6.3.1).

4. Measurement Techniques

4.1. Survey Design

There are three measured variables in the radar signal—time, power, and phase (Section 3)—and each variable can be used to infer anisotropy (i.e., in Equations 18, 20, and 21). In this section, we describe the measurement techniques from least to most complicated, including when and how each can be used to measure one or more of the variables for anisotropy. For integrated analyses, these techniques can be used together to leverage the strengths of each (e.g., Gerber et al., 2023).

4.1.1. Single Polarization

In a conventional (non-polarimetric) radar survey, the transmit and receive antennas are polarized in the same direction. Single polarization experiments can measure the power loss by birefringence as a function of depth, where the power loss is oscillatory at the beat frequency (see Equation 21). In theory, the beat signature can be measured in a stationary acquisition. However, in practice a two-dimensional (Z-scope) profile (i.e., concatenating individual soundings along track, also called a "radargram") makes the beat signature substantially easier to distinguish from reflectivity variations within the ice column because the shapes of those englacial reflecting horizons, which vary along track, are not expected to conform with the beat signature (Figure 9) (Gerber et al., 2023; Young, Schroeder, et al., 2021).

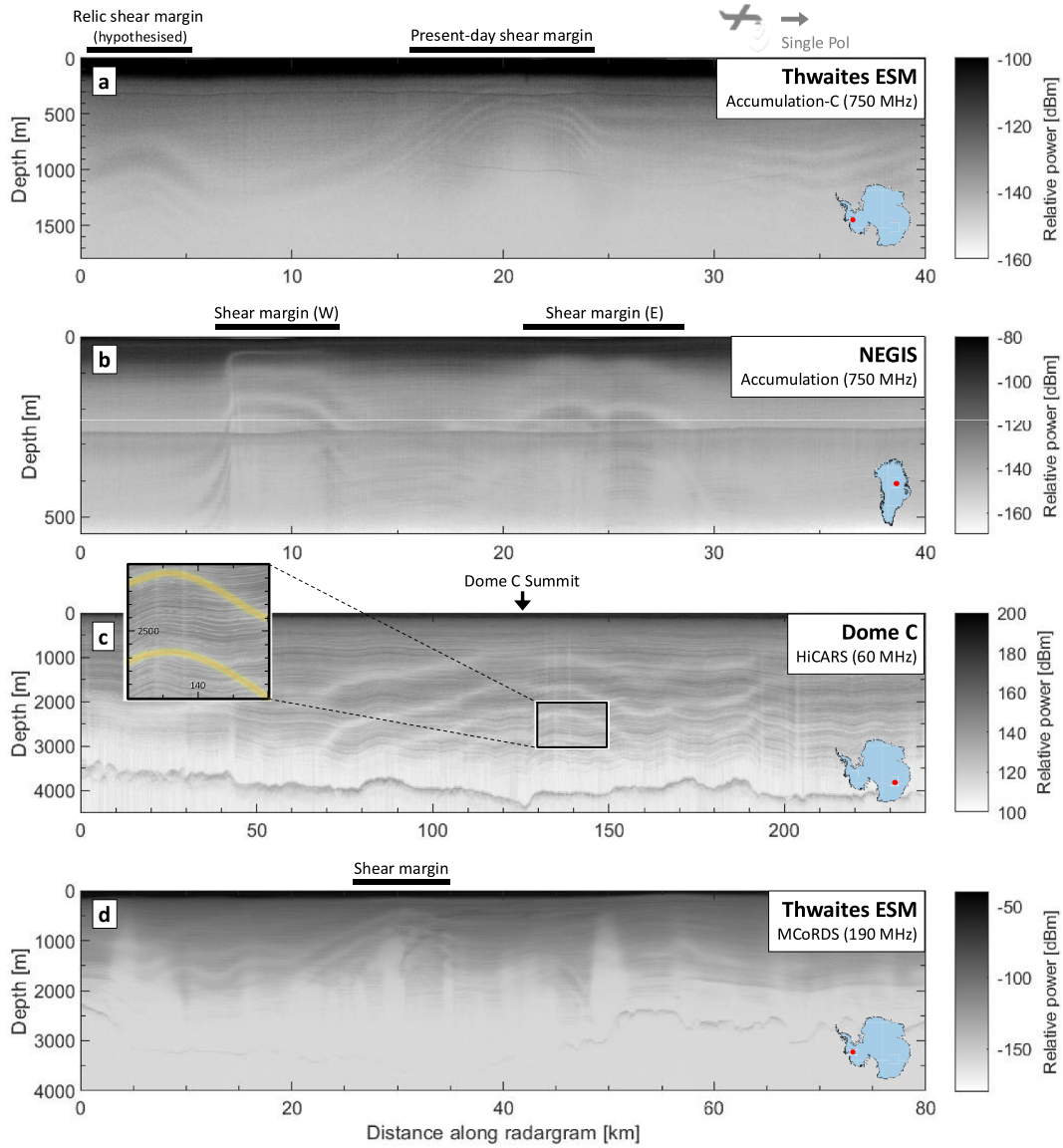

Figure 9. Single-polarization radargram observations of birefringent power losses seen through beat signatures with different radar systems and in different glaciological settings. (a) The eastern shear margin (ESM) of Thwaites Glacier, Antarctica using the Center for Remote Sensing and Integrated Systems (CReSIS) Accumulation-C radar. (b) The Northeast Greenland Ice Stream (NEGIS) using the CReSIS Accumulation radar. (c) Dome C, Antarctica using the High CApability Radar Sounder (HiCARS) radar. (d) ESM of Thwaites, now using the CReSIS Multichannel Coherent Radar Depth Sounder (MCoRDS). The beat frequency changes between images based on the instrument frequency and strength of the ice anisotropy. The inset within (c) shows the beat signature, highlighted in orange, to overlay the higher-frequency reflectivity variations created by changes in ice chemistry throughout the column. *Source:* Figure modified from Young, Schroeder, et al. (2021).

Not all single-polarization acquisitions produce a beat signature within the ice column, even if the ice is anisotropic, depending on survey design and radar architecture choices. If the polarization is aligned (or nearly aligned) with a principal axis (i.e., ψ is an integer multiple of $\pi/2$), then there is no (or minimal) birefringent power loss (Young, Schroeder, et al., 2021). Radar systems with a lower center frequency may produce a beat signature with wavelength longer than the ice column, especially if the anisotropy is weak. For example, with a ∼3–10 MHz radar frequency, a commonly used frequency range for ground-based radar surveying (e.g., Christianson et al., 2016; Welch & Jacobel, 2003), that propagates through ice with $\Delta\epsilon = 0.005$ (∼15% of pure crystal anisotropy) the signal will have a beat wavelength of ∼10–35 km (Figure 7), much longer than the

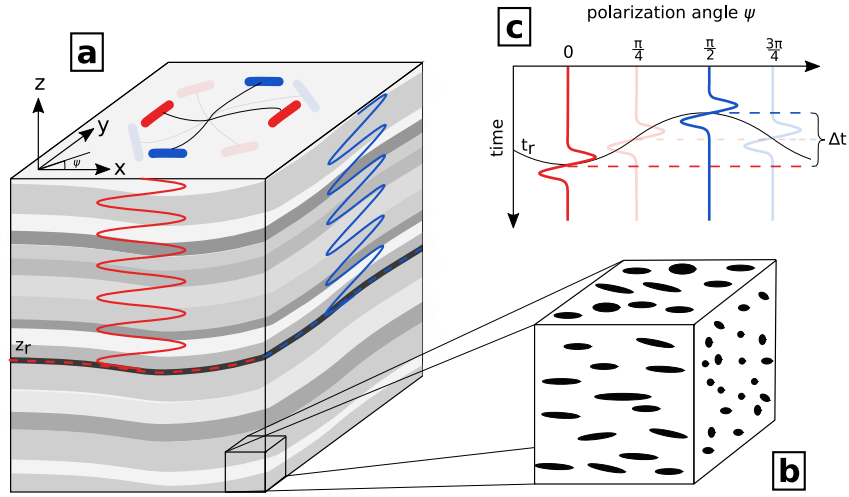

Figure 10. Illustration of dual- and multi-polarization radar surveys in an anisotropic media. Considering (a) a stratified ice sheet with anisotropic COF and *c* axes predominantly pointing in the horizontal direction, *x*, as illustrated by the ellipses in (b). Waves polarized parallel to the dominant *c*-axes direction (red) travel slower than waves polarized perpendicular to it (blue). In this case, (c) the time offset of a reflection signal from depth z_r between the two waves is maximal and phase shifts occur with depth. However, for antennas which are not aligned with the bulk principal axes ($\psi \neq 0$), the travel time difference is smaller and phase shifts less pronounced. Then, the inferred anisotropy is underestimated, which in the most misaligned case ($\psi = \frac{\pi}{4}$) results in no time offset at all (illustrated as faded lines in panel (c)).

thickness of any ice sheets on Earth. Even in some cases with strong anisotropy and the polarization misaligned from the principal axes, the beat signature can still be difficult to observe if, for example, anisotropic scattering causes vertical stretching of the co-polarization birefringence nodes (e.g., Ershadi et al., 2022, their Figure 3a, annotation L6).

Single-polarization surveys can also be used to infer anisotropy using time delay. Again assuming that the antenna is not aligned with the principal axes, the transmitted wave is split into two components that propagate at different speeds (after splitting). If anisotropy and reflector depth combine to produce a delay longer than the time resolution of the radar, these two components will appear as temporally distinct reflections when measured at the same orientation as the original transmission. The relative amplitude and temporal separation of the two returns can then be used to identify the strength and orientation of the fabric using Equation 18 and some trigonometry (Nymand et al., 2025). In theory, a single polarization is thus sufficient to infer anisotropy from travel-time delay, assuming the noise level is known, though to date it has only been applied to quad-polarization data (Nymand et al., 2025).

4.1.2. Dual Polarization

Now, consider two acquisitions with perpendicular polarization. These can be acquired with multiple antenna elements in a single radar design (Langhammer et al., 2019; Yan et al., 2020), by manually rotating the antenna elements between acquisitions (generally the strategy for ground-based single-point acquisitions), or by comparing single-polarization radargrams collected perpendicularly to one another (Bradford et al., 2013; Gerber et al., 2023). In any of these three measurement techniques one may observe: a power differential between polarizations in the case of anisotropic scattering (e.g., Gerber et al., 2025; Ross et al., 2020) or a time/phase delay between polarizations in the case of birefringence (Figure 10).

The time delay can be inferred by interpretation of the reflecting horizon in each acquisition, either by manually picking the travel times of the reflection in each recording (Gerber et al., 2023) or with an automated method by cross-correlation of the two time series (Zeising et al., 2023). The time delay increases with increasing ice thickness, so the relative uncertainty becomes smaller for deeper reflections. The associated anisotropy can be then calculated with Equation 18. The phase delay is inferred by coherence between acquisitions (Equation 19). Since acquisitions are generally noisy, the coherence can be averaged over some number of range bins, *M*, within a moving window (Dall, 2010; Lee et al., 1994)

$$C_{HHVV} = \frac{\sum_{m=1}^{M} \mathbf{s}_{HH,m} \cdot \mathbf{s}^{*}_{VV,m}}{\sqrt{\sum_{m=1}^{M} |\mathbf{s}_{HH,m}|^2} \sqrt{\sum_{m=1}^{M} |\mathbf{s}_{VV,m}|^2}}, \tag{29}$$

where $\mathbf{s}$ is the full array of measured range bins. Then, the phase uncertainty can be calculated using, for example, the Cramer–Rao bound (Jordan et al., 2019; Touzi et al., 1999)

$$\Xi_{\phi_{HHVV}} = \frac{1}{|C_{HHVV}|} \sqrt{\frac{1 - |C_{HHVV}|^2}{2M}}. \tag{30}$$

For small phase delays and negligible attenuation, the uncertainty should decrease with a larger coherence window (larger M) at the cost of lower range precision.

The magnitude of the coherence reduces with depth as the overlap of range-resolution cells of s_{HH} and s_{VV} decreases due to the time delay caused by the permittivity anisotropy. The coherence is lost when the apparent range difference observed for the same reflection between both polarizations is greater than the length of one resolution cell in range (Leinss et al., 2016). The depth limitation can be enhanced by reducing the bandwidth, which diminishes the range-resolution and facilitates the detection of a larger range difference (Zeising et al., 2025). Introducing a range bin offset $m + l$ for s_{VV} in Equation 29 allows an accurate determination of the travel-time difference for the same reflector from the co-registration of s_{HH} and s_{VV} (Zeising et al., 2023). High correlation values indicate the correct range-bin offset. This modification of the coherence method enables a more precise determination of the travel-time difference under strong anisotropy, as it maximizes the overlap of the range resolution cells. However, this modification requires the use of a high resolution (large bandwidth) radar system.

The anisotropy inferred by dual-polarization methods is affected by the antenna azimuth. For wave polarizations aligned with the horizontal principal axes, the anisotropy can accurately be determined by phase delay or travel-time difference methods. However, if antennas and the principal axes are misaligned, or when principal axes (or COF) rotations occur with depth, inferred anisotropy may be erroneously low (Figure 10b, faded profiles). In this sense, current dual-polarization methods can only provide a lower-bound estimate of horizontal anisotropy.

4.1.3. Multiple Polarization

Dual-polarization acquisitions are difficult to interpret when the COF principal axes are not aligned with the polarization directions since the time/phase gradient can be nonlinear in those cases. The opposite is true for single-polarization surveys, where interpretations of the beat signature are easiest when the principal axes are misaligned from the polarization direction. In this way, the two techniques complement each other. In cases where the expected anisotropy orientation is unknown, one may choose to repeat the dual-polarization acquisition at many azimuths, either by gradually rotating the antennas around their phase center (Hargreaves, 1977; Zeising et al., 2023), or by steering the radar system in a circle (Drews et al., 2012; J. Li et al., 2018). The multiple polarizations can be evaluated in the same way as the dual polarizations.

4.1.4. Quad Polarization

The final technique, quad-polarization acquisition, is similar to the previous, but can be accomplished without repeating measurements at multiple azimuths. Instead, cross-polarization acquisitions ($\mathbf{s}_{HV}$ and $\mathbf{s}_{VH}$) are used together with the co-polarization acquisitions (Figure 11) (e.g., Doake et al., 2002; Ershadi et al., 2022). With all four terms, a rotational transform is used to calculate the expected signal at any azimuth,

$$\mathbf{S}(\psi, z) = \mathbf{R}(\psi)\mathbf{S}_0(z)\mathbf{R}'(\psi), \tag{31}$$

where $\mathbf{S}_0 = \begin{bmatrix} \mathbf{s}_{HH} & \mathbf{s}_{VH} \\ \mathbf{s}_{HV} & \mathbf{s}_{VV} \end{bmatrix}$ is the measured waveform. The two cross-polarization terms are theoretically identical (in practice only one needs to be measured). Each measurement acquisition is an array of range bins, so rotating through all azimuths gives a total of four 2-dimensional complex amplitude images, one for each polarization ($\mathbf{S}_{HH}$, $\mathbf{S}_{VH}$, $\mathbf{S}_{HV}$, $\mathbf{S}_{VV}$). Hence, this technique gives the same information as for multiple polarization but now at

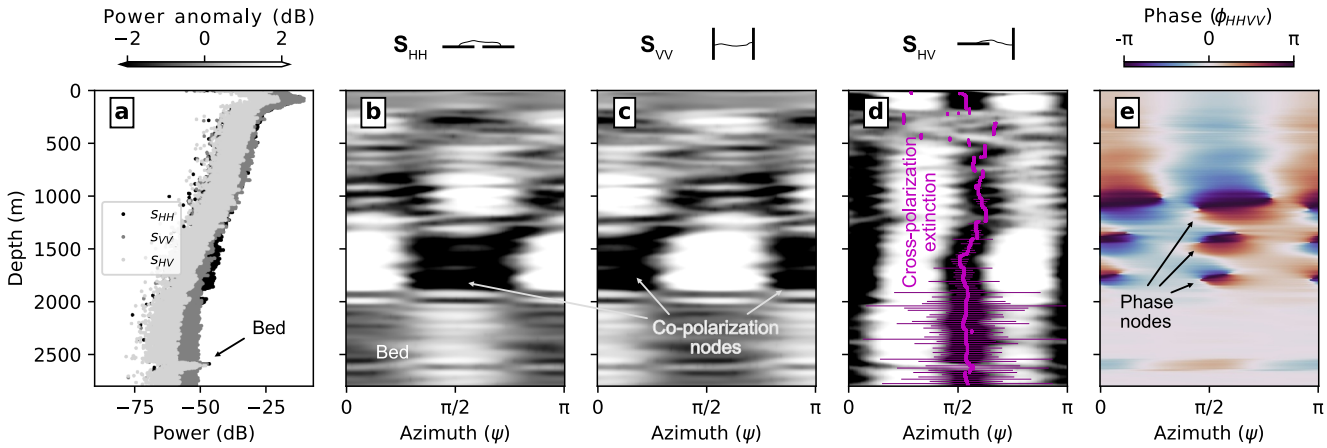

Figure 11. An example quad-polarization radar acquisition. (a) Individual A-scope acquisitions for both co-polarizations ($\mathbf{s_{HH}}$ and $\mathbf{s_{VV}}$) and one cross polarization ($\mathbf{s_{HV}}$). (b) Horizontally polarized power anomaly (removing the azimuthal mean for each range bin). (c) Vertically polarized power anomaly. (d) Cross-polarization power anomaly with the XPE axis (magenta) and uncertainty (violet). (e) Co-polarization phase calculated with Equation 29. *Source:* Figure recreated with data from Hills et al. (2025).

arbitrary azimuth, and the two have been shown to produce consistent results (Ershadi et al., 2022). The azimuthal resolution depends on the phase noise, but for acquisitions with minimal phase noise, the antenna placement may be the largest source of azimuthal uncertainty.

4.2. System and Antenna Design

Until recently, the radar systems used in polarimetry studies have not been specifically designed with the above measurements in mind. Instead, the systems conventionally used for either profiling (e.g., in Figure 9) or interferometry (e.g., the ApRES) have been adapted for polarimetry by implementing the survey designs described above. We therefore withhold discussion of any systems which are currently under development until Section 6.3, prioritizing here the design considerations which have been most relevant in making high-fidelity polarimetry observation possible up to now.

Anisotropy interpretations that use the beat signature (i.e., single polarization) are applicable across the broadest set of radar systems since they do not require coherence between acquisitions. There are two main constraints on the hardware. First, the system must have sufficiently high center frequency so that the beat frequency is expressed within the range of the ice thickness (~10–100s MHz for ~km thickness). Second, the system must have sufficiently high range-resolution to sample the beat frequency above the Nyquist frequency (100s kHz–MHz). Many modern radar sounders meet those criteria; for example, Figure 9 shows beat signatures successfully resolved in images from four different instruments (Young, Schroeder, et al., 2021). These instruments have been deployed on a variety of aircraft and with different radar antennas. Single polarization systems with two or more channels with different frequency bands could conceivably be used to correct birefringent losses across channels since the beat signature depends on the system frequency, although we are not aware of any studies which have done this up to now.

Quad-polarization surveys require phase-coherent radar systems and phase stability to obtain meaningful results from the coherence in Equation 19. Coherent stacking can improve the signal-to-noise ratio and reduce phase noise in coherence estimates, so stationary ground-based surveys with long acquisition times have been common. Some early coherent polarimetry experiments used a vector network analyzer as a continuous wave radar system (Doake et al., 2003), but more recently the ApRES has become the most widely used of the phase-coherent systems in terms of polarimetry applications. The ApRES transmits a linear frequency-modulated continuous wave, optimized to be used with a 1 s chirp from 200 to 400 MHz. Two antenna types are commonly used with the ApRES, including for polarimetry applications, the skeleton slot and cavity-backed bowtie (Nicholls et al., 2015), with tradeoffs in durability, price, and data quality. The ApRES can be manufactured in two designs, single-input single-output (SISO) and multiple-input multiple-output (MIMO). The SISO ApRES is commonly used for both multiple-polarization (Jordan, Schroeder, et al., 2020; Zeising et al., 2023) and quad-polarization measurements

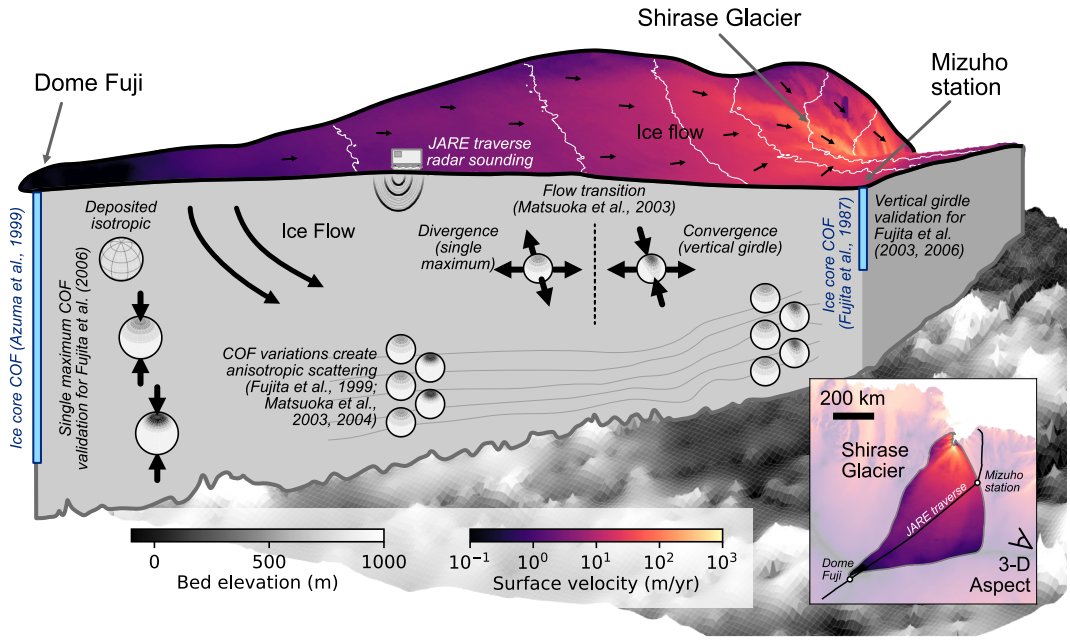

Figure 12. A new visualization of prior interpretations from foundational radar polarimetry studies. Surface velocities and the associated unit vectors (Mouginot et al., 2019) from the Shirase Glacier basin (Rignot et al., 2019) are plotted on the extruded surface topography (Howat et al., 2019), and the extruded bed topography (with less vertical exaggeration than the surface) is consistent with its plotted colormap (Pritchard et al., 2025). The vertical cutaway slice with drawn interpretations is along the traverse line of the 37th Japanese Antarctic Research Expedition (Fujita et al., 1999). The visualized COF interpretations are based on those from the original work (Azuma et al., 1999; Fujita & Mae, 1993; Fujita et al., 1987, 2003, 2006; K. Matsuoka et al., 2003, 2004; Yoshida et al., 1987). (inset) Map view of the visualized area, see also Figure 13.

(Ershadi et al., 2022; Jordan et al., 2022; Young, Martín, et al., 2021), each of which requires reorientation of the antennas. Because MIMO ApRES can leverage up to 16 channels (Young et al., 2018), it has the ability to capture quad-polarization data using four channels without manually reorienting antennas between acquisitions (Ershadi et al., 2024).

Many other multi-channel systems that can acquire quad-polarization data without manually reorienting antennas now exist. As we will see in Section 6.3.2, their promise in terms of polarimetry applications is toward a moving platform that can acquire quad-polarization data continuously. In designing these multi-channel multi-polarization systems, a challenge is to simultaneously address: the high bandwidth needed for range resolution, effective isolation between antenna elements (i.e., cross-polarized antennas should act independently), and a small form factor which can still transmit within the frequency band where ice is transparent.

5. Glaciological Applications for Crystal Orientation Fabric

Understanding intrinsic anisotropy and its implications for ice flow have been the primary focus of polarimetric radar applications. In Section 5.1, we summarize the *early* history (until 2006) of polarimetric radar consisting of initial validation, the introduction of phase-coherent radars, and research preceding the seminal work of Fujita et al. (2006) (Figure 12), which provided the basis of modern methods to infer COF from polarimetric radar. In Section 5.2, we then discuss how these modern methods have been validated through comparison to ice cores, while also considering some of the synergies that have resulted from these comparisons. Finally, in Section 5.3, we describe modern applications of polarimetric radar to infer COF, interpret past ice flow, and evaluate the effect of modern COF on ice-sheet rheology and flow. Throughout, we reference locations in Greenland and Antarctica where this work has been done (Figure 13).

5.1. Early History of Polarimetry Measurements

Some of the earliest polarimetric radar experiments established it as a useful tool for determining COF. Hargreaves (1977) found the first in situ confirmation of birefringence in ice at radio frequencies by identifying

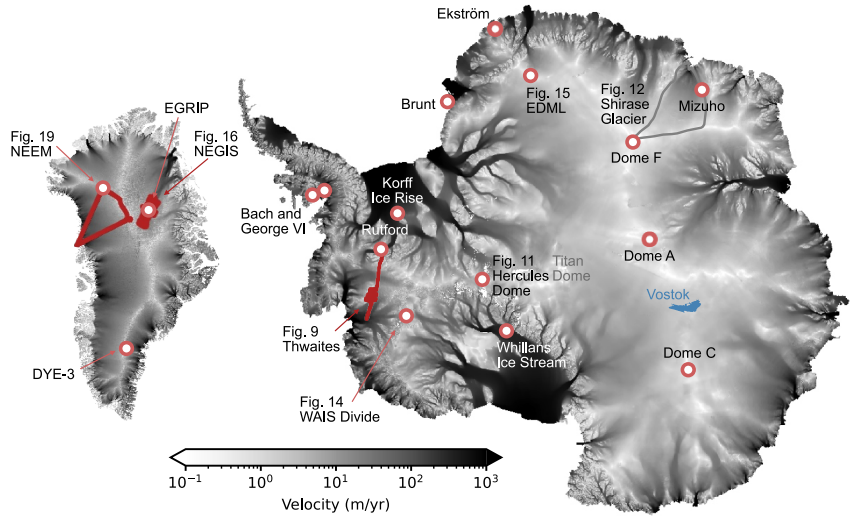

Figure 13. Overview maps with site locations for select polarimetry studies described in this article. Grayscale is surface velocity for Greenland (Joughin et al., 2010) and Antarctica (Mouginot et al., 2019).

azimuthal variations in return power near the DYE-3 site in Greenland. Power varied with characteristic 90° azimuthal periodicity and was consistent with constant birefringence (and thus COF) with depth. Yoshida et al. (1987) conducted detailed measurements of bed-echo power variations with azimuth at Mizuho station in Dronning Maud Land, East Antarctica. They found that birefringence aligned with flow, consistent with early theoretical predictions of COF development (Budd, 1973). Fujita and Mae (1993) later used this same data set, combined with their intervening measurements of dielectric anisotropy (Fujita et al., 1993) and COF in an ice core drilled at Mizuho station, to argue that internal reflections observed in these data were due to variations in COF. Siegert and Kwok (2000)'s and Siegert and Fujita (2001)'s analyses of radar transects around Dome C, Lake Vostok, and Titan Dome (near South Pole) demonstrated that internal reflections were caused by COF at certain depths, though they could not associate these reflections with particular COFs. Fujita et al. (1999) and K. Matsuoka et al. (2004), aided by the mounting evidence for fabric-induced reflections, attributed the presence of several hundred meter thick "high scattering zones" between 900 and 1,500 m depth (~50% of the ice column) near Mizuho to alternations of COF induced by ice flow. They interpreted these data as suggesting that the COF was a depth-increasing vertical girdle, indicative of convergent flow at Mizuho station. K. Matsuoka et al. (2003) identified spatial variability in anisotropic signals between six sites along a flowline from Dome F through Shirase Glacier, finding evidence of both birefringence and anisotropic scattering, spatially consistent with model predictions of COF variations between convergent and divergent flow (Azuma, 1994).

Other early polarimetric radar focused on ice shelves. Woodruff and Doake (1979) conducted polarized measurements upstream and downstream of the grounding line of Bach Ice Shelf, finding a marked change in anisotropy of the bed reflection across the grounding line. Doake et al. (2002) made the first polarimetric radar measurements that leveraged phase information. They used a precursor to the modern ApRES to measure the amplitude and phase of the basal reflection from Brunt and George VI ice shelves at various orientations. They were able to infer birefringence in the ice column and anisotropic reflection at the ice-ocean interface. Although this work foreshadowed coming methods for more accurate inference of COF, the 2π ambiguity in the phase of returns and the simplicity of their approach prevented meaningful interpretation of the birefringence in terms of COF.

5.2. Validation of Radar-Derived COF

Radar methods to infer COF (Section 4) can be tested against *c*-axis measurements derived from ice-core thin sections (Table 2), and mechanisms of COF-induced internal reflections, originally theorized from first principles, can be corroborated through direct comparison with observed layering in ice cores (e.g., Eisen et al., 2007). However, although ice cores provide the most precise measure of COF strength (through thin sections), it is rarely possible to recover the azimuthal orientation of COF due to the rotation of the core in the barrel during or

Table 2
Instances Where Radar-Derived COF Has Been Validated With Direct Measurements

Glacier setting (specific site)	COF type (direct sample)	Radar match to COF	Reference
Flank (Mizuho Station)	Vertical girdle	Magnitude and core orientation	Fujita and Mae (1993) and Fujita et al. (2006)
Ice dome (Dome Fuji)	Single maximum (vertical)	Magnitude only (power method)	Fujita et al. (2006)
Ice divide (NEEM)	Single maximum (vertical)	Magnitude only (coherence method)	Dall (2010) and Jordan et al. (2019)
Ice divide (WAIS Divide)	Vertical girdle	Magnitude with depth (see Figure 14c)	Young, Martín, et al. (2021)
Ice dome (EDC and EDML)	Single maximum (vertical) transitioning to vertical girdle	Magnitude for all three eigenvalues	Ershadi et al. (2022)
Ice stream (NEGIS)	Vertical girdle	Magnitude only (cross-method comparison)	Gerber et al. (2023)
Ice stream (NEGIS)	Vertical girdle	Magnitude with depth (cross-correlation method)	Zeising et al. (2023)

Note. The ice-core azimuthal orientation could not be reconstructed in any case but one (Mizuho), so radar-derived COF orientation cannot be validated, magnitude only, except in that one case. For some glaciological settings where geophysical interpretations of COF have been made, they have not been directly validated (e.g., in ice stream shear margins).

following extraction (Fitzpatrick et al., 2014; Westhoff et al., 2021). Radar methods offer a means to resolve this missing component of COF orientation. Moreover, ice cores sample only a single horizontal point, so the application of radar polarimetry to expand the spatial footprint from ice-core sites represents a marked improvement toward exploring and quantifying the ice anisotropy regionally. Polarimetric radar measurements near ice cores thus create synergistic opportunities to recover the ice-core orientation and expand the measured COF spatially. This opportunity was recognized early in the history of polarimetric studies (e.g., Hargreaves, 1977; Yoshida et al., 1987), and new polarimetric radar methods are commonly demonstrated near ice-core sites as well (e.g., Ershadi et al., 2022; Nymand et al., 2025; Zeising et al., 2023).

5.2.1. COF Birefringence

In their seminal work, Fujita et al. (2006) developed the framework to quantitatively determine COF from radar (Section 3) and validated their results against ice core data from two sites near Mizuho station and Dome Fuji. Using their new matrix-based model to interpret these data, they showed that measured variations of return power with depth and azimuth were consistent with the thin-section-derived COF obtained at these core sites (Azuma et al., 1999; Fujita et al., 1987). They were able to distinguish between birefringence and anisotropic scattering effects based on the azimuthal periodicity of their measured signal, where the scattering signal at Mizuho was in agreement with the COF measurements from the core (Fujita et al., 2003).

Two other methods to infer COF from similar data (quad- or multi-polarization at one point in space) have been validated against ice-core data. The polarimetric coherence method, based around the same matrix model but focusing on the coherence phase (Equation 19), was validated using radar surveys at the North Greenland Eemian Ice Drilling (NEEM) project ice core site (Dall, 2010; Jordan et al., 2019). These studies quantified COF eigenvalues by estimating the relative phase between orthogonal co-polarized measurements, finding eigenvalues in close agreement with those from the ice core. Compared to more direct analysis of power anomalies as in Fujita et al. (2006), this method avoids some of the ambiguities caused by azimuthal periodicity in birefringent and scattering effects. A travel-time based method using cross-correlation between co-polarization acquisitions was validated against data from the East Greenland Ice-Core Project (EastGRIP) (Zeising et al., 2023). This work found excellent agreement between the radar-inferred and ice-core-inferred COF and also showed that their method was more practical than a power-based approach in regions where rapid changes in COF with depth cause poor coherence.

These three methods (Dall, 2010; Fujita et al., 2006; Zeising et al., 2023) provide practical options to infer the horizontal eigenvalue difference $\Delta\lambda = \lambda_x - \lambda_y$, but are unable to infer the vertical eigenvalue λ_z. They are thus unable to discern azimuthally invariant COFs (e.g., vertical single maximum, horizontal girdles) or other COFs with similar horizontal expression (e.g., vertical girdles vs. weak horizontal single maxima). To address this limitation, Ershadi et al. (2022) used the reflection ratio (Equation 26) to reconstruct the vertical eigenvector iteratively from the surface. They validated this method by comparing ApRES measurements against ice-core

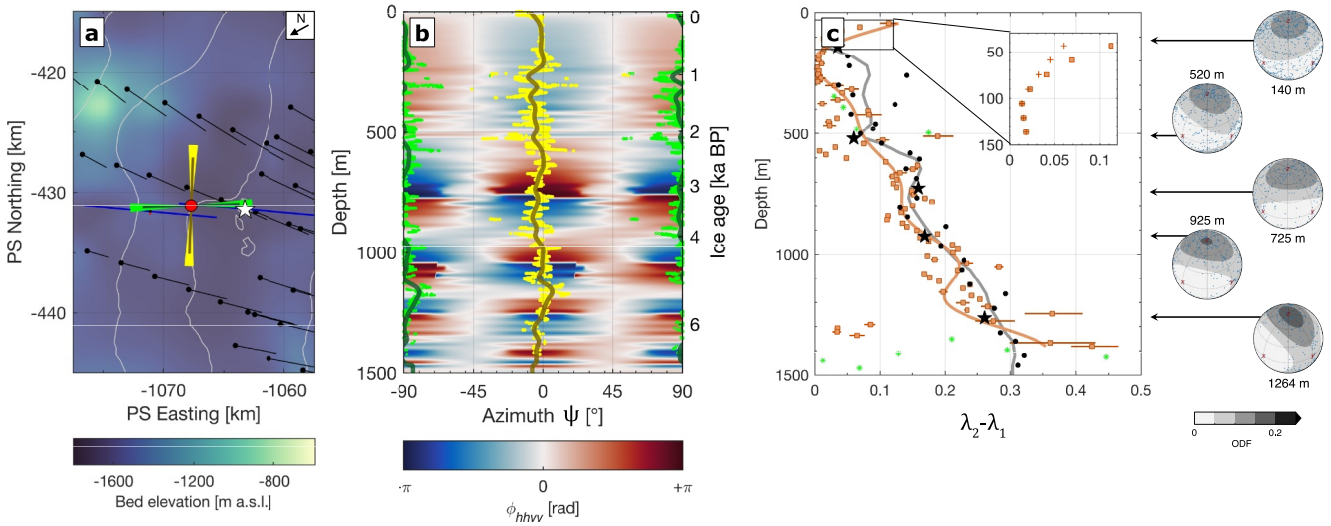

Figure 14. Radar-derived anisotropy at WAIS Divide (Young, Martín, et al., 2021). (a) Map of their quad-polarization survey location (red dot) and regional surface velocity field (black lines). (b) Co-polarization phase as in Figure 11e, with calculated orientations of the λ_1 (green) and λ_2 (yellow) eigenvectors corresponding to directions shown in panel (a). (c) Horizontal anisotropy as a profile with depth calculated from radar (orange) and comparison to that measured in ice-core thin sections (black). The inset shows near-surface horizontal anisotropy values with (orange squares) and without (orange crosses) corrections to account for depth-dependent density in the firn layer, as suggested by Jordan et al. (2019). Examples of COF measured in individual ice core thin sections (corresponding to black stars) are represented as *c*-axis distributions (grayscale, following Figure 3) and with individual grain COFs (blue dots). *Source:* Figure adapted from Young, Martín, et al. (2021).

data near the European Project for Ice Coring in Antarctica Dome C (EDC) and Dronning Maud Land (EDML) cores, finding that they could infer all three eigenvalues under the assumption that one eigenvector was vertical and that the resulting values were consistent with the respective ice cores. However, their method required site-specific tuning, and Zeising et al. (2023) found that this method was ineffective at inferring COF near EastGRIP, likely due to rotations of the COF eigenvectors with depth. Thus, to date, no method can favorably reproduce all three eigenvectors from multi-polarization radar at all sites.

The West Antarctic Ice Sheet (WAIS) Divide ice-core site provided a key test bed for comparing methods for COF inference more broadly. Since there are four independent calculations of ice fabric at WAIS Divide through ice-core observations (Fitzpatrick et al., 2014; Voigt et al., 2015), sonic logging (Kluskiewicz et al., 2017), seismic surveys (Horgan et al., 2011), and radar polarimetry (K. Matsuoka et al., 2012; Young, Martín, et al., 2021), WAIS Divide is an ideal site for cross-methods comparison as well as multi-method data assimilation to reconstruct the full fabric eigenvector solution. K. Matsuoka et al. (2012) conducted an areally extensive polarimetric radar study (60 km × 150 km) around WAIS Divide and observed depth-variable azimuthal shifts within the ice column, corresponding to flow regimes at their respective age-depth periods. At the ice-core site, however, their results were inconclusive due to periodic node ambiguities through depth. However, Young, Martín et al. (2021)'s subsequent investigations using a ground-based quad-polarization survey found excellent agreement with corresponding thin-section COF estimates (Figure 14). They determined that the current COF matches the present-day strain regime through the measured depth interval (~40% of the total ice column). Closer to the bed, ice-core measurements indicate COF changes toward a vertical single maximum, implying increased horizontal shear from basal resistance (Fitzpatrick et al., 2014). These dynamic changes occur within the well-known radar "echo-free zone" (e.g., Drews et al., 2012; Fujita et al., 1999). This gap in data can be filled with other geophysical methods. For example, in-borehole sonic logging (Kluskiewicz et al., 2017) resolves only λ_z, but at centimeter resolution, complementing the results obtainable with radar.

Although ice cores have provided critical validation for radar measurements of COF, the range of ice dynamics that they sample is limited. Ice cores are generally not drilled in the more ice-dynamically active areas that hold a larger range of fabric types. One notable exception is the EastGRIP core (Dahl-Jensen et al., 2021), motivated by the International Partnerships for Ice Core Sciences program "ice coring for ice dynamics," which was accompanied by a number of radar and seismic surveys. With a new approach to virtually re-orient part of the retrieved core (Westhoff et al., 2021) it became feasible to compare anisotropy deduced from radar (e.g., Gerber et al., 2023) and seismics (e.g., Pearce et al., 2024) to the core-based results quantitatively. Although EastGRIP

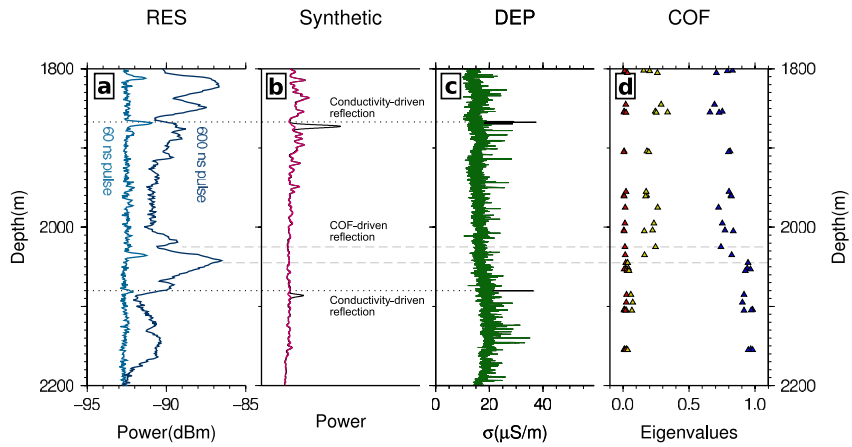

Figure 15. A comparison of EDML ice-core measurements to the nearby radar sounding profiles. (a) Radar profiles from 60 to 600 ns transmitted pulses. (b) Synthetic 60 ns radar profile produced using measured ice-core variables plotted in (c) conductivity and (d) eigenvalues of COF (Weikusat et al. (2017b) with data from Weikusat et al. (2013); Weikusat et al. (2013a, 2013b)). Red line in (b) has major conductivity peaks removed. *Source:* Figure adapted from Eisen et al. (2007).

provides important validation, there is still a lack of measurements of COF in other dynamic areas—a gap that polarimetric radar could remedy. With increased confidence in the interpretation, radar polarimetry methods can now be applied to prospective ice-coring site locations where no ground truth is yet available. For example, at Hercules Dome, derived girdle orientation and magnitude are consistent with present-day ice flow, implying no significant change in ice dynamics since at least the mid Holocene (Hills et al., 2025).

5.2.2. COF Transitions and Associated Reflections

Englacial radio echoes are reflected by conductivity or permittivity contrasts (Fujita & Mae, 1994) from changes in the ice impurity content (Eisen et al., 2003; Gudmandsen, 1975), ice density (Robin et al., 1969), or COF (Eisen et al., 2007; Harrison, 1973). It can be difficult to determine the permittivity contrast that caused an individual reflection since each type of contrast can manifest similarly or ambiguously. However, the origins of radar reflections can be examined with direct ice samples near ice-core sites. If identified reflections correspond in depth to sharp contrasts (relative to the radar wavelength) in electrical conductivity (ECM, typically measured in vacant ice core holes or along ice cores), then their source is likely to be the presence of impurity and density contrasts (e.g., Hempel et al., 2000; Mojtabavi et al., 2022). On the other hand, if reflections cannot be explained by the coincident ECM profile, as shown at the EDML ice-core site, then they are likely to arise from COF transitions (Eisen et al., 2007) caused by an orientation-dependent permittivity contrast due to an abrupt change (again relative to the wavelength) in COF anisotropy (Figure 15). Differences in reflected power at different azimuths can also be used to infer COF-type reflections. Drews et al. (2012) found two zones of anisotropic scattering near EDML and, using the ice-core timescale, hypothesized that the transition between the two could be linked to a glacial-interglacial age transition. After ruling out other plausible sources, they concluded that small-scale eigenvalue fluctuations with depth are the most likely source of anisotropic scattering at EDML. Similar observations have also been made at the Northeast Greenland Ice Stream (NEGIS) (Gerber et al., 2025), where anisotropic scattering follows the ice-sheet stratigraphy, is most likely linked to COF fluctuations, and can thus act as an independent measure of COF orientation, as long as other sources of anisotropic scattering can be ruled out. B. Wang et al. (2018) analyzed a gridded polarimetric radar survey centered around Dome A and extending to the Vostok ice-core site, identifying several prominent transitions in scattering at depths consistent with glacial-interglacial cycles, showing how these transitions in COF can be used to expand measurements over a large region beyond ice-core sites themselves.

5.3. Ice Dynamics Interpretations

5.3.1. Inference of Past Ice Flow

Because COF develops as a result of stress and strain, it can be used to reconstruct the history of ice flow (e.g., on geologic timescales). Such an approach is particularly important for ice-covered areas far from geologic sources

of information on past ice-mass configurations (e.g., for enabling the dating of exposed erosional surfaces or erratics using cosmogenic nuclides; Schaefer et al., 2022). Analysis of COF within the ice can provide direct evidence of past ice-flow direction, key glaciological features such as shear margins, and, potentially, speed (Lilien et al., 2021). Ice-flow history can refer to either: (a) the range of different deformation regimes (e.g., vertical shear, vertical compression) experienced by the ice along its past flow path (Llorens et al., 2022), or (b) temporal changes in ice flow (e.g., ice stream deactivation, migration, or widening) (Lilien et al., 2021). Polarimetric radar has identified COF changes with depth that cannot be explained by local glaciological conditions at the site of measurement, and these variations in COF have been attributed to deformation regimes upstream. Multi-polarization radar near Mizuho station revealed that ice at different depths showed different anisotropic scattering properties, interpreted as resulting from varying modes of deformation upstream (K. Matsuoka et al., 2004). More recently, quad-polarization radar on Rutford Ice Stream showed that COF near the surface is consistent with the local deformation regime, while in places deeper COF is substantially rotated (Jordan et al., 2022). This deeper COF is consistent with strain upstream, suggesting that the COF advected to the measurement site while preserving inherited information about its past deformation. It is thought that COF can survive strains of 100% or more with some overprinting (Alley, 1988; Llorens et al., 2022), and thus persist for ∼1–10 kyr in typical ice-sheet conditions (Lilien et al., 2021; Thorsteinsson et al., 2003), so the relatively frequent mismatch between COF and local conditions is unsuprising. However, some recent work has questioned whether COF is truly a proxy for strain history in light of processes that depend on strain rate and temperature as well as total strain (Hunter et al., 2023), implying that the theoretical foundations for inferences about past flow might be tenuous.

Less work has attempted to use polarimetric radar to infer temporal variations in flow. In the clearest example of such work to date, polarimetric radar data acquired alongside seismic measurements at Korff Ice Rise in the Weddell Sea Sector of WAIS, an area with few geologic constraints on ice-flow history (Siegert et al., 2019), showed that COF in the lower half of the ice column was almost perpendicular to the present-day ice flow direction (Brisbourne et al., 2019). They interpreted the COF as having developed under past flow conditions, with ongoing evolution to reflect the present-day flow regime. In this case, a change in flow dynamics was independently known from other geophysical evidence and modeling (Kingslake et al., 2016), supporting this interpretation. Similarly, Nymand et al. (2025) observed an asymmetry in COF orientation across the center of NEGIS and argued that this is inconsistent with steady flow. Instead, they hypothesized that the asymmetry results from changes in ice flow during the Holocene that have been independently identified by several recent studies (Franke et al., 2022; Grinsted et al., 2022; Jansen et al., 2024). COF-related beat signatures in radargrams have been used to infer the possibility of inward migration of the eastern shear margin of Thwaites Glacier (Young, Schroeder, et al., 2021). These studies qualitatively identified changes in flow from radar, but using fabric evolution models to identify COF lifetimes (Lilien et al., 2021) for specific scenarios may allow quantification of preceding flow regimes. Further development of such models to more accurately account for recrystallization timescales is necessary to make them applicable in the warmest and most dynamic areas of the ice sheets (Richards et al., 2023) and thus to be fully confident in resulting reconstructions of ice-flow history.

5.3.2. Implications for Modern Ice Dynamics

Estimates of COF in highly dynamic areas, such as ice shelves, ice streams, outlet glaciers, grounding lines, and shear margins, are of great interest because flow speeds in these areas modulate ice-sheet contributions to sea-level rise (e.g., Miles et al., 2022; Otosaka et al., 2023). In glacier ice, COF-induced mechanical anisotropy can substantially alter its effective viscosity in the principal strain directions and, in some regimes, can magnify its "softness" (ease of deformation) by up to three orders of magnitude (Shoji & Langway, 1985). COF may influence flow patterns by softening shear margins (Grinsted et al., 2022; Minchew et al., 2018), facilitating internal deformation and flow over sticky spots (Rathmann & Lilien, 2021), and hardening ice in such a way as to couple its motion along flow (Gerber et al., 2023), though the overall effect is complicated and geometry-dependent (Ma et al., 2010; McCormack et al., 2022). Direct measurements of fabric are logistically difficult to obtain in dynamic areas, and coupled with a general desire to obtain ice cores with long, undisturbed paleoclimate records, this has led to a dearth of measurements of COF in areas of fast or complex flow, with a few notable exceptions (Gerbi et al., 2021; Jackson & Kamb, 1997; Thomas et al., 2021; Zeising et al., 2023). Moreover, until recently, many large-scale models of fabric development were questionably applicable to these dynamic areas because they neglected migration recrystallization (Faria, 2006a, 2006b), and those models now capable of describing fabric

evolution in such areas are still in need of validation (Lilien et al., 2023; Richards et al., 2021, 2023). Seismic inferences of COF exist in a few fast-flowing regions (Picotti et al., 2015; E. C. Smith et al., 2017), but radar-based measurements of COF provide the majority of COF data in dynamic areas and are thus critical for inferring viscosity and for model validation. However, persistent challenges to obtaining information relevant for ice flow from polarimetric radar remain due to the difficulty in characterizing the full three-component fabric (Ershadi et al., 2022; Fujita et al., 2006; Rathmann, Lilien, et al., 2022), unconstrained higher-order moments of the fabric that affect directional viscosity (Rathmann & Lilien, 2022), and the subtle assumptions needed to derive viscosity from orientation (Castelnau et al., 1996; Jordan et al., 2022).

Following demonstrations that fabric could be inferred in dynamic areas using polarimetric radar (Jordan, Schroeder, et al., 2020), quantitative description of the effect of radar-derived COF began with Jordan et al. (2022). They used ground-based coherent radar on Rutford Ice Stream to infer the horizontal eigenvalue differences, which they converted to directional viscosities based around assumptions about the vertical component of the fabric. In turn, the range of viscosities was calculated using an established, fully tensorial viscosity model (Gillet-Chaulet et al., 2005; Martín et al., 2009), with assumptions about how grain-scale properties translate to the polycrystal scale (Castelnau et al., 1996; Gillet-Chaulet et al., 2005) and, implicitly, how $\mathbf{a}^{(4)}$ varies as a function of $\mathbf{a}^{(2)}$ (Gagliardini & Meyssonnier, 1999; Gillet-Chaulet, 2006). The considerable uncertainty in directional viscosity was dominated by a given $\Delta\lambda$ being consistent with multiple fabrics (i.e., λ_z was poorly constrained); nevertheless, their results demonstrated that flow enhancement can be estimated directly from polarimetric radar without use of a fabric-development model. Methods from Ershadi et al. (2022) might be used to constrain λ_z. Whether the anisotropic flow relation, the closure approximation (i.e., assumptions about $\mathbf{a}^{(4)}$), or residual uncertainty about $\mathbf{a}^{(2)}$ would then dominate uncertainty in the viscosity is unclear. Application of seismic surveys may resolve the latter two problems: P-waves are sensitive to the vertical component of the fabric and $\mathbf{a}^{(4)}$ (Rathmann, Grinsted, et al., 2022), whereas S-waves are sensitive to the horizontal properties, and seismics are often applied with larger offsets (i.e., not only waves propagating at nadir but also with larger angles of incidence). Further details on seismic approaches are provided in Appendix B.

In the last 5 years, the development of methods to infer ice properties from single-polarization radars has enabled fabric investigation of fast-flowing regions using airborne surveys originally designed for other applications. One beat-signature approach (Section 4.1.1) proposed by Young, Schroeder, et al. (2021) was motivated by observations of anomalous power loss in radargrams when crossing the shear margins of Thwaites Glacier, one of the fastest flowing and most globally impactful ice streams (Joughin et al., 2014). By tracing out birefringence nodes horizontally and with depth, they found that COF was consistent with expectations about such a dynamic area, with weak COF outside the ice stream, large $\Delta\lambda$ consistent with a horizontal single maximum in the shear margins, and moderate $\Delta\lambda$ consistent with a vertical girdle in the midst of the ice stream. Gerber et al. (2023) approached the same problem in calculating the beat frequency through application of an independently developed spectral analysis to radargrams, thereby revealing the relationship between $\Delta\lambda$ and beat frequency through automated means. This approach could potentially be applied across most existing airborne radargrams, thus expanding coverage to wide swaths of the ice sheets. With beat frequency analysis alongside crossover-point analysis of airborne radargrams collected in 2018 over NEGIS (Franke et al., 2021) and point-based multi-polarization measurements that crossed its shear margins, Gerber et al. (2023) presented an extensive synthesis of COF around NEGIS that showed reasonable agreement across all methods and with measurements derived from ice cores drilled at EastGRIP and at NEGIS's shear margin (Figure 16). By using their inferred COF to validate models of fabric development that calculated anisotropic flow enhancement across the NEGIS catchment, they showed that the inferred enhancement factors would significantly alter viscosity, demonstrating that important rheological parameters can now be inferred from radar surveys at the ice-stream scale.

6. Extended Applications and Future Directions

Although the majority of radar polarimetry applications in glaciology have focused on COF and the associated ice dynamic or ice-flow history interpretations in terrestrial ice (Section 5), a subset of applications has considered different mechanisms for anisotropy as well as the anisotropy of planetary ice masses. Future work in these extended applications may, in turn, improve geophysical techniques that aim to resolve COF in Earth's ice sheets. In Section 6.1, we review the interpretations of anisotropy ascribed to mechanisms unrelated to crystal *c*-axis-driven birefringence or scattering. In Section 6.2, we give a brief background on some radar applications in

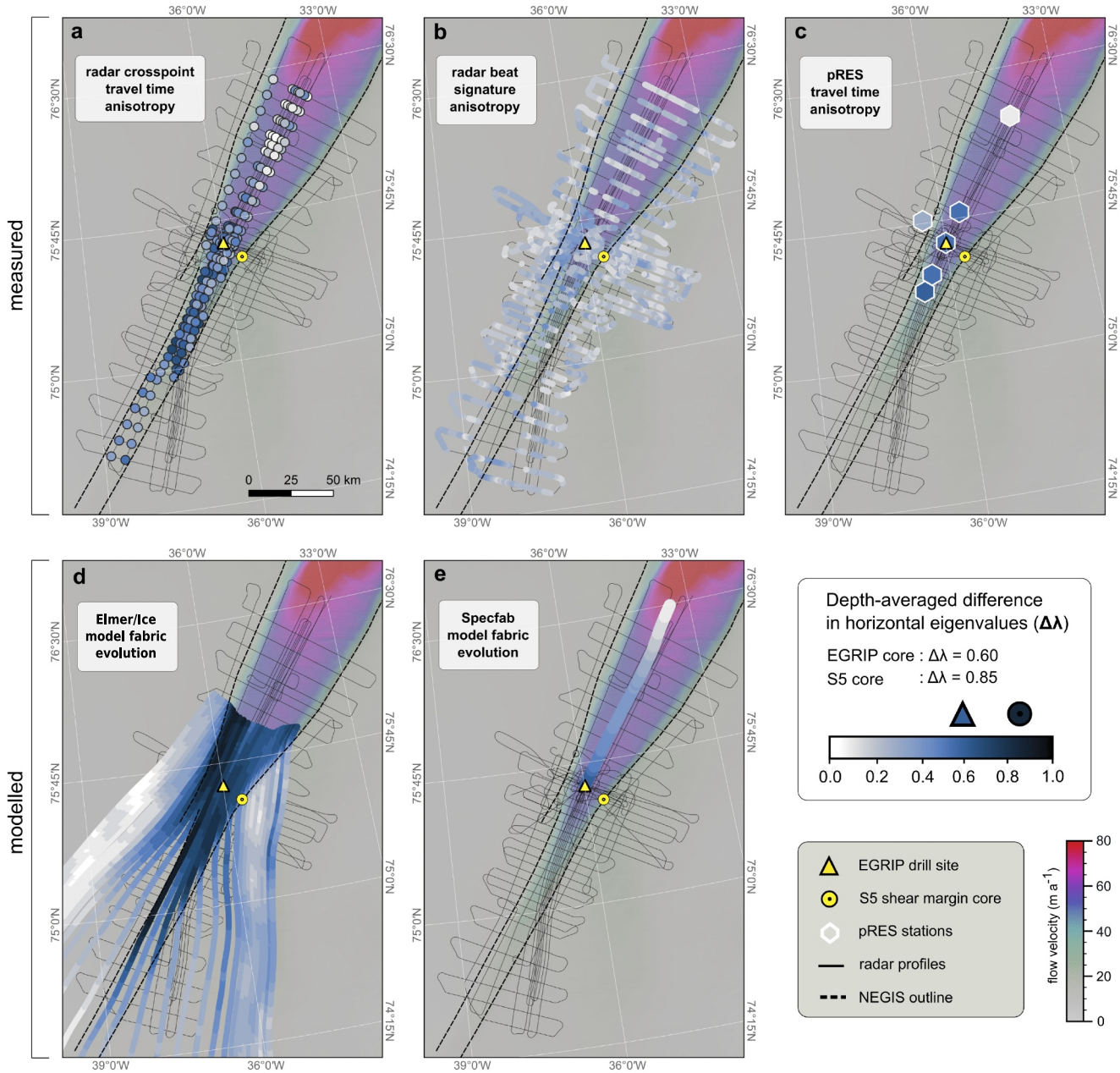

Figure 16. Comparison between radar-based estimates of horizontal anisotropy from (a) crosspoint travel-time, (b) beat signature, and (c) ApRES travel-time analyses and simulations of COF-evolution models in the NEGIS region from (d) Elmer/Ice and (e) Specfab (Gerber et al., 2023). Radar-derived eigenvalue differences agree reasonably well among these methods, and with ice-core observations and COF simulations with Elmer/Ice (panel d; Lilien et al., 2021) and Specfab (panel e; Rathmann et al., 2021). *Source:* Figure adapted from Gerber et al. (2023).

planetary sciences and astrophysics and how similar polarimetric analyses could be used for additional insight in those fields. Finally, in Section 6.3, we discuss emerging research that is advancing polarimetric measurement techniques.

6.1. Anisotropy Interpretations Beyond COF

6.1.1. Attenuation Anisotropy

The electrical conductivity of an ice crystal may be anisotropic at radar frequencies (T. Matsuoka et al., 1997), although less so than the real permittivity anisotropy which has been the focus of this review. Polycrystalline ice is

more conductive when impurities exist at grain boundaries (e.g., liquid water veins in temperate ice; Raymond & Harrison, 1975), so it can have strongly anisotropic conductivity if grain shapes are preferentially elongated in specific direction(s). Because radar attenuation is directly dependent on conductivity (MacGregor et al., 2007), these anisotropic properties would be measurable as differential losses between polarizations.

Temperate ice can have anisotropy in the shape of meltwater between grains (i.e., the "melt-preferred orientation"; MPO) which may develop based on the stress setting (Seltzer et al., 2024). Although attenuation anisotropy in temperate glacier ice has not been explicitly demonstrated with radar, theory suggests it could be useful for constraining the extent of temperate ice (e.g., near the ice-sheet bed or an ice-stream shear margin). Since temperate ice has increased scattering (Fountain et al., 2005), successful constraints on attenuation anisotropy would likely require a targeted ground-based survey and possibly a complementary seismic experiment (see Section 6.3.1).

Sea ice can exhibit attenuation anisotropy due to the brine inclusions between ice grains (Babcock et al., 2015). The inclusion properties, such as volume fraction, shape, size, connectivity, and salt concentration, depend on the environment during ice formation and growth, notably the temperature gradient. For columnar sea ice, brine pockets are oriented perpendicularly to the crystal *c* axis. External pressures from wind and tides during ice formation can preferentially align this matrix, resulting in attenuation anisotropy since salinity content is the main driver for sea ice conductivity. This phenomenon can reduce or eliminate the ice-bottom radar reflection, making feature detection beneath the ice difficult (e.g., oil spills; Wilkinson et al., 2017). Based on similarities between sea ice anisotropy and the MPO above, it is worth considering physical and methodological parallels in sea ice research, which could eventually be applied in temperate glacier ice, or at ice shelves and planetary ice shells both of which overlie conductive ocean water.

6.1.2. Bed-Echo Anisotropy and Specularity

Roughness of the subglacial bed on scales below the horizontal resolution of radar systems still causes anisotropic scattering of radar waves. This anisotropy enables polarimetric investigation of sub-resolution characteristics, such as the distribution of water or fine-scale morphology of the ice-sheet substrate, that have important implications for the stress balance governing ice flow (M. Hoffman & Price, 2014; A. O. Hoffman et al., 2022; Hogan et al., 2020). For entirely specular targets, there is no polarization dependence to the reflectivity, which limits the utility of polarimetric radar for their characterization (D. Long & Ulaby, 2015). However, for rough surfaces, a fraction of the reflected energy is incoherently scattered (Giannopoulos & Diamanti, 2008), possibly with some dependence on polarization, enabling target imaging at a range of angles, as well as introducing a cross-polarization signal absent for specular interfaces. Because the polarization and angular distribution of scattered energy depends on both large and small-scale heterogeneity at the scattering interface, it then becomes possible to leverage polarimetric radar to directly diagnose these properties. For glaciological radar sounding, applications have focused on the ice-bed interface, as we describe here, but englacial interfaces with directional roughness can theoretically cause anisotropic scattering as well (Gerber et al., 2025), although those interfaces are generally more specular.

By characterizing the total recovered energy as a function of angle for co-polarization, *HH* systems, Schroeder et al. (2013) showed that features below the resolution of their radar system could be evaluated using the directional-dependence of observed backscattering. They quantified this directional-dependence in terms of anisotropy in the "specularity content" (a measure that relates the nadir response to the integrated incoherent scattering along a flight path). This type of analysis pushes beyond the simplest form of the radar equation, which considers only nadir imaging and coherent scattering (Bogorodskiĭ et al., 1985). To apply the radar equation to polarimetric, incoherent scattering, we must include both a polarization and angle dependence to the system and synthetic aperture geometries, ice-surface transmissivity, and the target geometry and dielectric properties. The polarimetric response of sub-wavelength features can be included in scattering models through the radar cross-section of the target (e.g., Ruck et al., 1970).

Using approaches described in the applied geophysics literature (Radzevicius & Daniels, 2000), Scanlan et al. (2022) showed that both analytical approaches and simple method of moments models can be used to estimate the polarimetric response for different configurations of the subglacial hydrologic network. Their work provides a model for future polarimetric data interpretation. Based on a priori expectations for the nature of subglacial roughness or the distribution, size, and orientation of subglacial meltwater channels, it should be

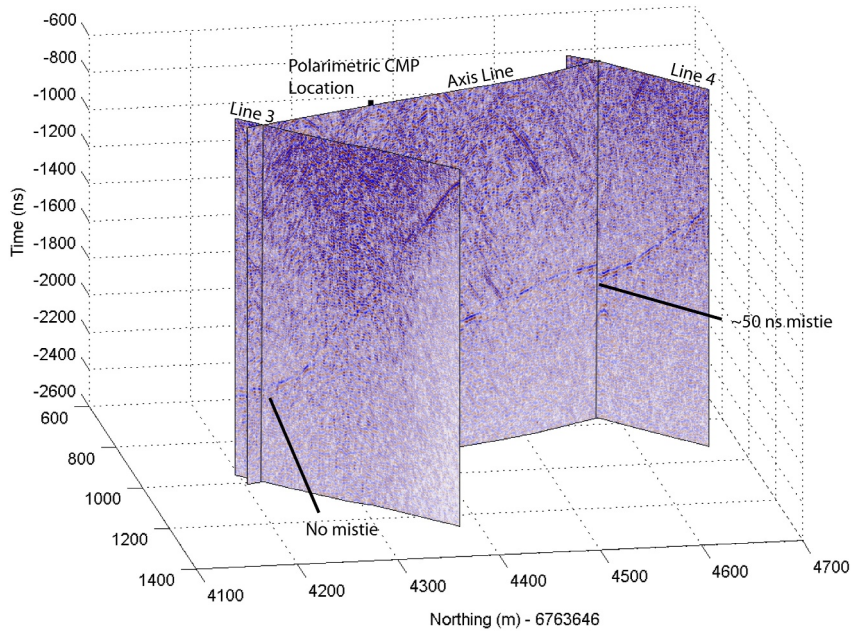

Figure 17. Perpendicular radar sounding images in an alpine glacier setting. The "mistie" is a time delay from birefringence associated with a directional crevasse field. They also conducted a polarimetric CMP experiment, the results from which are not shown here. *Source:* Figure adapted from Bradford et al. (2013) with permission from the International Glaciological Society.

possible to calculate the quad-polarization scattering matrix (Equation 23), and evaluate hypothesized properties against observations. There are challenges associated with non-uniqueness in the scattering responses of different interfaces (due to specific feature orientation, permittivity, and scale), and more study is required to establish the limits of polarimetry in roughness and hydrological research.

6.1.3. Extrinsic Anisotropy

Disruptions in the ice media can lead to bulk birefringence, attenuation anisotropy, or both, depending on the electrical properties and directional alignment of the non-ice material. Spatially extensive disruptions (e.g., crevasses) will generally cause incoherent scattering as well, which can make these forms of anisotropy difficult to infer from radar observations alone. Still, there have been several notable efforts studying and interpreting extrinsic anisotropy in glacier ice with radar polarimetry, both at the macro (crevasses) and micro (bubbles) scales.

Crevasse openings manifest on roughly the meter scale. Radar polarimetry applications investigating this macro-scale damage should therefore either: (a) focus on anisotropy in the scattering itself (Matsouka et al., 2007; Nobes, 1999), or (b) transmit at sufficiently low frequencies ($\ll$100 MHz, equivalent to $\sim$1.7 m wavelength in ice) to limit scattering effects from overwhelming the desired birefringent signal. When designed appropriately, radar surveys can be used to infer crevasse orientation (at cross-polarization extinction) as well as properties of the mixed media such as porosity or water content for water-filled crevasses. Bradford et al. (2013) demonstrated the feasibility of measuring crevasse anisotropy from birefringence with a 25-MHz radar survey in an alpine-glacier setting (Figure 17). They observed a notable time delay between azimuths in both dual-polarization and multi-polarization surveys, consistent with anisotropy interpretation from coincident seismic data.

At the microscale, non-uniformities within firn and glacier ice, such as elongated pores and bubbles, may similarly cause birefringence or anisotropic scattering (e.g., due to a change in "bubbliness"). Oraschewski et al. (2025) demonstrated that bistatic polarimetric radar can detect structural firn anisotropy, specifically vertically elongated pores, which can dominate birefringence during oblique radio-wave propagation. Using a radiative transfer model, Drews et al. (2012) partitioned the effects of COF and bubbles around the EDML drill site, and concluded that azimuthal variations in volume scattering from elongated bubbles were small due to small

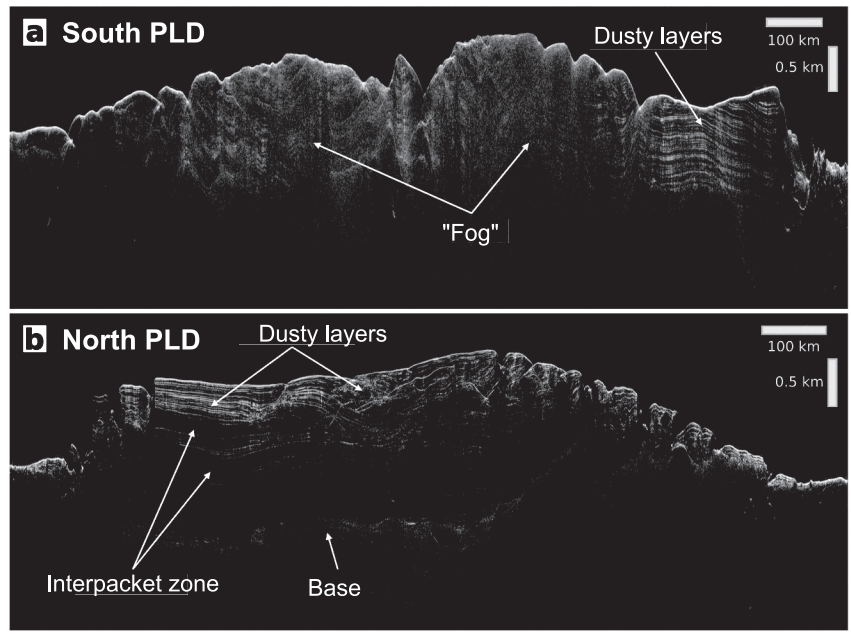

Figure 18. SHARAD radargrams of Mars' Polar Layered Deposits (PLDs). (a) South PLD, where bright subsurface reflectors are laterally discontinuous. Whether they are absent at specific locations or just obscured by the diffuse radar pattern, usually referred to as fog (Whitten & Campbell, 2018), is uncertain. (b) North PLD, which features a laterally continuous structure, with packets of bright layers separated by radar-dark zones (Phillips et al., 2008).

diameters (this could be revisited using the effective medium approach outlined in Section 3.1). Similarly, they concluded that anisotropic backscatter at EDML was due to vertical variations in COF (Drews et al., 2012), rather than impurities or bubbles.

6.2. Applications in Planetary Science and Astrophysics

6.2.1. Planetary Ice

Water ice has been found throughout the solar system, for example on Mars in small shaded reservoirs (e.g., Brothers & Holt, 2016) or within debris (e.g., Plaut et al., 2009), in the Martian polar caps (e.g., Picardi et al., 2005; Plaut et al., 2007), or in the thick shells of icy moons which potentially conceal subsurface oceans (e.g., Nimmo & Pappalardo, 2016). Although the study of terrestrial ice can benefit from several independent observational methodologies including orbiter-based, airborne, ground-based, and in situ measurements, the exploration of planetary ice remains limited, for now, to orbiter-based techniques such as radar sounding, visible imaging (e.g., Fishbaugh et al., 2010), and gravimetry (e.g., Broquet et al., 2021). Complementary insights can be gained through the investigation of Earth analogs, which can be extremely valuable to interpret planetary ice observations (e.g., Culberg et al., 2022).

The connection between COF, dynamics, and bulk composition of ice formations make anisotropy investigations of particular interest for planetary applications, where dynamics and rheology of icy structures are poorly constrained. Important questions, such as the presence or absence of ice flow in the polar caps of Mars or the detection of material uplift suggesting past ocean-surface interactions in Europa's shell, could be effectively addressed using the radar polarimetry methods discussed in this review. Here, we emphasize two environments of particular interest, first, the North and South Polar Layered Deposits (NPLD and SPLD) of Mars, and second, the thick ice shells on Jovian moons (in particular that of Europa), but we note that the full range of potential planetary applications are much broader than what is covered here.

The PLDs (NPLD and SPLD) are masses of ice at the Martian poles with lateral dust layers (Phillips et al., 2008; Plaut et al., 2007) that manifest in radar images similar to Earth's ice sheets (Figure 18). To date, they are the most extensively studied examples of planetary ice, with detailed three-dimensional reconstructions of their internal structure derived from sounding data (Foss II et al., 2024). Two orbital radar sounders are actively probing the

surface and subsurface of Mars: the SHAllow RADar (SHARAD) (Seu et al., 2007) and the Mars Advanced Radar for Subsurface and Ionosphere Sounding (MARSIS) (Picardi et al., 2004). SHARAD operates at 20 MHz center frequency with a 10 MHz bandwidth for a vertical resolution of around 8 m in clean water-ice, whereas MARSIS, thanks to its lower frequency between 1.8 and 5 MHz, has greater penetration but lower resolution. Although both SHARAD and MARSIS are single-polarization systems, some of the techniques described in Section 4 could feasibly be used to asses anisotropy. To date, we are not aware of any active efforts to observe radar beat signatures in the Martian polar caps. Any such attempt would be challenged by radar clutter due to off-nadir surface and/or subsurface scatterers that could obscure the periodic beat. Additionally, a relatively shallow thickness compared to the expected beat wavelength may also limit the applicability of this technique for measuring ice anisotropy. Instead, crossing orbital tracks may enable anisotropy inference from time/phase delay analyses. In particular, the Mars Reconnaissance Orbiter, which carries SHARAD, has a sun-synchronous polar orbit which crosses many times over the PLDs.

Thick planetary ice shells, like that on Europa, conceal subsurface oceans, which are one viable environment for planetary life (Lunine, 2017). Visible signs of activity at the surface suggest that these shells range from tectonically and/or volcanically active on Europa to moderately active on Ganymede to inactive on Callisto (Daubar et al., 2024; Heggy et al., 2017). Ice dynamics within shells, whether associated with tectonics or any form of upwelling (i.e., cryovolcanism, diapirism, displacement from volumetric expansion due to freezing/contraction due to melting), could develop a COF within the ice shell. Additionally, that COF would be a partial control on the ice-shell rheology, along with the temperature and composition of non-ice intrusions (both of which are also poorly constrained (Blankenship et al., 2024)). Hence, surveying ice-shell anisotropy could give insight on both past and present dynamic activity, much like for the ice sheets on Earth as explored in Section 5.

Around 2030, the Radar for Icy Moon Exploration (RIME) onboard the Jupiter Icy Moons Explorer (Juice) (European Space Agency) (Bruzzone et al., 2013; Grasset et al., 2013) and the Radar for Europa Assessment and Sounding: Ocean and Near-surface (REASON) onboard Europa Clipper (National Aeronautics and Space Administration) (Blankenship et al., 2024; Pappalardo et al., 2024) will arrive to Jupiter and begin surveying the shells of the planet's icy moons: Europa, Ganymede, and Callisto. RIME will operate at 9 MHz with up to 3 MHz bandwidth, and REASON is a dual-frequency radar: first 9 MHz with 1 MHz bandwidth and second 60 MHz with 10 MHz bandwidth. Much like the Martian sounders, both RIME and REASON are single-polarization systems, but again the beat-frequency and crossover-based approaches could be used, especially since Europa Clipper's trajectory is designed to have multiple intersections of its ground track over Europa (Roberts et al., 2023).

6.2.2. Constraints for Neutrino Detection

The ice sheets on Earth are a natural laboratory for detection of high-energy neutrinos which originate from cosmic accelerators outside our solar system, such as supernovas, black holes, or other extreme extragalactic phenomena (IceCube, 2013). Neutrino collision with an ice molecule emits Cherenkov radiation at frequencies between ∼150–800 MHz (Allison et al., 2012), frequencies at which ice is transparent and birefringent. This secondary Cherenkov radiation can be detected using instruments installed within the ice (if appropriately shielded from cosmic rays and other background radiation). Hence, instrumented arrays of Cherenkov detectors have been installed in ice at South Pole (Abbasi et al., 2011; Achterberg et al., 2006), with plans for both an expansion there (Aartsen et al., 2021) and a complementary array at Summit station in Greenland (Aguilar et al., 2021).

To better constrain the origin trajectory of detected neutrinos, it is important to know the dielectric properties of the ice through which the Cherenkov radiation propagates (e.g., Aguilar et al., 2023; Welling & Collaboration, 2024). Since that radiation is in the same frequency band as the active-source radar sounding instruments discussed in this article, it is subject to the same birefringent effects when in anisotropic ice (Abbasi et al., 2024). COF has been directly measured from ice-core samples at the sites of current and future detector arrays, South Pole (Voigt, 2017) and Summit station (Gow et al., 1997). In both cases, there is a strong component of vertical anisotropy, especially in deep ice. Unlike the vertically propagating waves which are most common in radar sounding applications, Cherenkov radiation in ice propagates outward in all directions from the neutrino collision toward detectors. The vertical eigenvalue is often the strongest, so obliquely propagating waves may exhibit stronger birefringence than vertically propagating (with measurements up to 0.3% of the mean refractive index or $\Delta\lambda \approx 0.3$; Allison et al., 2019; Kravchenko et al., 2011) The oblique waves are also more complicated in

producing two ray path solutions that highlight refraction effects (Deaconu et al., 2018; Prohira et al., 2021). Modeled studies based off empirical polarization time delay measurements revealed that birefringence can indeed be used to constrain the range to a theoretical neutrino interaction in certain configurations, but additional refinement of processes included in modeling oblique radio-wave propagation is needed to achieve sufficient precision for reliable neutrino detection (Connolly, 2022; Jordan, Besson, et al., 2020). In these ways, there are mutual synergies between how understanding of glacier physics can be used to calibrate and correct neutrino detection, how in situ radio-frequency experiments that leverage these arrays further theoretical and methodological understanding of in-ice oblique radio-wave propagation, and how a deep understanding of the optical properties at the in-ice instrument arrays can develop glaciological understanding.

6.3. Innovations in Polarimetric Surveying

6.3.1. Stationary Soundings and Integrated Geophysical Experiments

Stationary, polarimetric ground-based radar surveys have seen widespread use as a component in multidisciplinary field campaigns. Integration with other co-located geophysical investigations allows for improved constraints when inferring COF and other englacial and subglacial properties. In theory, ground-based radar systems allow the user to place the source and receiver in separate locations at the surface, or within the glacier volume where boreholes are present, to vary both the total propagated distance and the incidence angle of energy in the subsurface. Collecting polarimetric data with large variations in incidence angle allows for a more comprehensive investigation of COF compared to standard monostatic polarimetric surveys, since it can provide a more direct constraint on λ_z (K. Matsuoka et al., 2009). In practice, obtaining long-offset radar measurements, with offsets on the order of kilometers, can prove difficult due to the hardware limitations of commonly used radar systems, but several approaches to address these limitations are in development which we describe next.

Impulse radar systems have been employed to collect long-offset radar data both in single-polarization (e.g., Holschuh et al., 2016; Winebrenner et al., 2003) and multiple-polarization (e.g., Bradford et al., 2013). Such systems are incoherent, so only travel time and wave amplitude (not phase) can be measured. However, multiple measurements taken at the same location can be incoherently stacked to achieve higher signal-to-noise ratios through time-synchronization using the direct path. Furthermore, in the absence of a cabled connection between source and receiver, the direct path through the air must be detectable in order to trigger a recording, potentially setting a limit on the maximum attainable offset. For amplitude analysis, the correction of the received amplitude for the radiation pattern of antennas poses an intrinsic problem as the radiation pattern measured in free space will be distorted when operating on a medium like snow, firn, or ice, which are inhomogenous and anisotropic.

Coherent systems provide a phase-sensitive solution to some of these limitations, increasing the precision of time/phase delay interpretations (Oraschewski et al., 2025). However, it can be difficult to maintain phase coherence for long antenna offsets. Some novel approaches are being applied to maintain sufficient signal-to-noise ratio over long distances (e.g., Bienert, Schroeder, Peters, et al., 2022; Paden et al., 2005). When deployed in a common mid-point (CMP) or wide-angle reflection/refraction (WARR) configuration, the collection of polarimetric data can potentially map important englacial and subglacial properties, including ice temperature, bed material composition, water content, ice COF, and firn structure and density, through leveraging the signal anisotropy present through signal refraction, transmission, and reflection (Bienert, Schroeder, Peters, et al., 2022; Bienert, Schroeder, & Summers, 2022; Oraschewski et al., 2025). Importantly, coherent oblique returns would likely enable more consistent and accurate reconstruction of all three fabric eigenvectors than has previously been possible (K. Matsuoka et al., 2009).

Geometries permitting direct transmission of energy from source to receiver, such as vertical seismic profiling (Booth et al., 2020; Brisbourne et al., 2021; Fichtner et al., 2023), allow for more direct observation of ice properties compared to reflection-based radar due to reduced uncertainty in travel path lengths and directionality, properties that have proved advantageous in recent seismic measurements (Lutz et al., 2022; Rathmann, Grinsted, et al., 2022). Although radars have also been deployed down boreholes, those cross-borehole or "trans-illumination" experiments typically use incoherent systems in a single polarization and have been limited in borehole depth and offset, focusing on near-surface variations in water-content (Axtell et al., 2016; Murray et al., 2000). Fortunately, similar approaches to long-offset surface radar measurements can be applied to borehole measurements (e.g., using a low-loss fiber optic cable to connect radar elements). Due to geometry constraints, however, modifications to the antennas used may be required to ensure they can fit down a borehole,

Table 3
Quad-Polarization Profiling Radars in Use and in Development

System name	Platform	Frequency (MHz)	Reference
PASIN	Airborne (Twin Otter)	145–155	Arenas-Pingarrón et al. (2023)
POLARIS	Airborne (Twin Otter, Basler)	392.5–477.5	Dall et al. (2010)
CReSIS RDS (multiple versions)	Ground-based sled	135–165	J. Li et al. (2018)
	Airborne (Basler)	150–600	Hale et al. (2016)
EastGRIP Radar	Ground-based sled	180–480	L. Li et al. (2022)
AccumRadar	Ground-based sled	600–900	Kaundinya et al. (2023)
MIMO ApRES	Ground-based rover	200–400	Ershadi et al. (2024)

though the development of down-hole probes suggest that such limitations can be overcome (Prior-Jones et al., 2021).

6.3.2. Polarimetric Profiling

Radar profiling is commonly used for regional-scale surveying of glaciers and ice sheets. As shown in Section 5.3, some studies have demonstrated the viability of anisotropy interpretations from airborne profiling platforms: with single-polarization systems using the beat signature (Young, Schroeder, et al., 2021), with dual-polarization systems (Scanlan et al., 2022), and at cross-over points (Gerber et al., 2023). The single- and dual-polarization methods are complementary in that the former performs best when misaligned from the principal axes by $\pi/4$ and the latter performs best for perfect alignment. However, at the regional scale, the COF principal axes orientation may be unknown, and in a region with varying orientation the radar polarization, hence the aircraft heading, should in principle be changed accordingly to maximize the sensitivity to anisotropy. Instead, a quad-polarization system can be mounted on a moving platform to carry out conventional radar profiling at all four polarizations in order to capture signal across all azimuths.

Six such systems that we know of are at varying stages of development and being used for polarimetric profiling today (Table 3). First, the Polarimetric Airborne System INstrument (PASIN) (Heliere et al., 2007) and the upgraded version, PASIN2, are airborne radar developed by the British Antarctic Survey. This system has primarily been used in its "standard," single-polarization antenna configuration for geometric surveying of the Antarctic Ice Sheet (Frémand et al., 2022), but it also has a quad-polarization antenna configuration for which the capabilities are under study (Arenas-Pingarrón et al., 2023). Second, the Polarimetric Airborne Radar Ice Sounder (POLARIS) (Dall & Kusk, 2009) was developed by the Technical University of Denmark specifically as a quad-polarization radar (Dall, 2009). POLARIS features a dual-polarization microstrip patch array (Vazquez-Roy et al., 2012) with an 85 MHz bandwidth, developed to assess the feasibility of orbital radar sounding through ice. Third, the Center for Remote Sensing and Integrated Systems (CReSIS) has been developing a series of radar depth sounder (RDS) instruments for about 40 years. As for PASIN, these have generally been operated in a single-polarization mode for ice-sheet surveying, but polarimetric capabilities are being developed in several cases. An early prototype was tested in 2008 on the ground at NEEM (J. Li et al., 2018), and a subsequent wideband version (Hale et al., 2016) was flown over the NEGIS in 2018 (Franke et al., 2021). Fourth, the "EastGRIP Radar" developed by the University of Alabama is a ground-based system that can be towed behind a snowmobile and is capable of continuous, quad-polarization, ultra-wideband (180–480 MHz) measurements (Nymand et al., 2025; Yan et al., 2020). Fifth, a new version of the CReSIS accumulation radar, which primarily targets shallow stratigraphy, has a polarimetric mode (Kaundinya et al., 2023). Finally, Ershadi et al. (2024) deployed an autonomous rover outfitted with a four-channel MIMO ApRES which collected 23 km of quad-polarimetric radar data across the grounding zone of Ekström Ice Shelf.

As quad-polarization becomes a standard in the suite of radar-profiling capabilities, regional- and even continental-scale surveying of ice-sheet anisotropy will become possible. As an example, Figure 19 shows a depth- and azimuth-resolved *HH-VV* phase delay calculated from polarized measurements with POLARIS. From these data, the extracted COF orientation is consistent between flight tracks after compensating for the different aircraft heading (approximately aligned with the ice divide) and is consistent with a girdle COF, as expected for

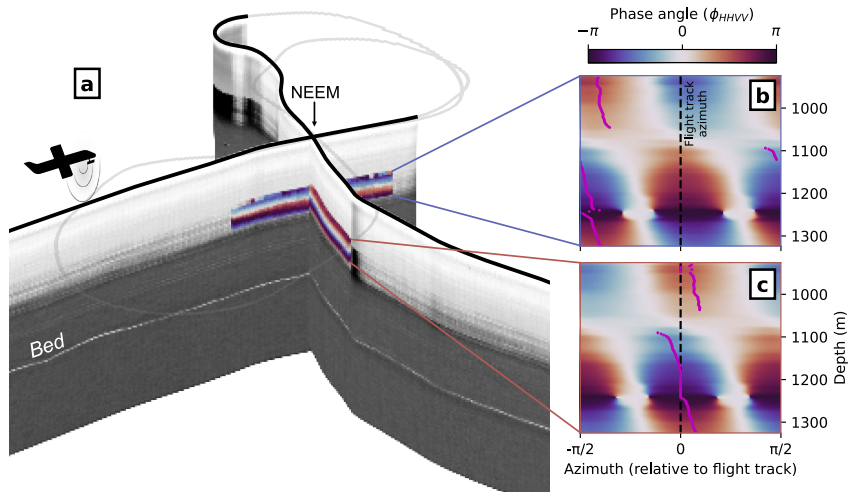

Figure 19. A proof-of-concept for quad-polarization profiling with POLARIS, flown at the NEEM ice-core drilling site in 2008 (Dall, 2020). (a) The two tracks flown, one parallel and one perpendicular to the ice divide with the *HH*-power (grayscale profiles) and the *HH*-*VV* phase delay (colored profiles) near the summit location. Using all four polarizations together in Equation 29 the phase delay can be projected to all azimuths for both the northeast-bound track (b) and the southeast-bound track (c). The COF horizontal principal axis (λ_2, assuming λ_3 is vertical) is estimated from the XPE and shown relative to the flight track for both flights (magenta). *Source:* Figure adapted from Dall (2020).

this ice divide. In addition to the implications for COF interpretation, polarimetric profiling could be used to interpret bed-interface anisotropy, buried crevasse orientation, and possibly other features not described here.

7. Conclusion

In this review, we have described a unified theoretical framework for interpreting polarimetric radar, summarized currently used methods, described key applications, and identified the emerging frontiers for radar polarimetry as applied in glaciology. To date, radar polarimetry's greatest contribution has been information about intrinsic anisotropy, its COF. The broad adoption of relatively affordable and easy to use ground-based coherent radar instruments are enabling collection of multi-polarization data at locations throughout both of Earth's ice sheets, providing widespread information about COF. Nascent methods exist to use radar polarimetry for applications beyond intrinsic anisotropy, but these techniques are much less developed. Still, the theoretical framework described in this review provides a foundation for understanding both intrinsic and extrinsic anisotropy. We hope that by providing this shared framework and terminology we can standardize future studies so that they can easily be compared with one another.

We anticipate that future work in polarimetric radar sounding will both expand applications for extrinsic anisotropy and further improve techniques for measuring intrinsic anisotropy. In this review, we focused on developments in: (a) wide-angle surveys, which will allow measurement of the full set of COF eigenvectors and values, and (b) profiling radars, which will allow more spatially comprehensive measurement of anisotropy. However, we hope that this review also serves to guide new and existing users of radar polarimetry to where other opportunities exist. For example, we hinted at how emerging techniques to infer COF from crossover points of radars on Earth might lay the groundwork for similar application to Mars or icy Jovian moons, and how the propagation path of Cherenkov radiation from neutrinos might be used synergistically with nadir-looking polarimetry to constrain COF in more dimensions. As deployments of polarimetric radars continue to expand, we hope that this review can guide users toward the diversity of emerging and established techniques to maximize the scientific impact of these data.

Appendix A: Survey Geometry and Polarization Notation

Throughout the manuscript, we use a coordinate reference system oriented with the survey geometry (Figure 5a), where x and y are aligned with the radar antenna array in the horizontal plane. We reference anisotropy in that x-y plane, both in the ice column and at the reflecting interface, as an ellipse with an azimuthal rotation, ψ,

counterclockwise from the x-axis. Then, z is the vertical dimension, with some number, N, of modeled layers with thickness, dz, from top to bottom of the ice column.

For polarization, there has been some notation inconsistency in published articles since the radar and seismic literature tend to use different notation (Appendix B). We choose to use the notation from the remote sensing literature, which has also been the most commonly used in radioglaciology (e.g., Ershadi et al., 2022; Young, Martín, et al., 2021). Under this notation, "H" indicates horizontally polarized (in line with the antenna array, in the x direction) and "V" indicates vertically polarized (perpendicular to the antenna array, in the y direction). Then, co-polarization acquisitions (with transmit and receive antennas in the same orientation) are HH or VV, and cross-polarization (perpendicular antenna orientations) are HV or VH. Some radar antennas, such as the commonly used ApRES skeleton slot antenna, are not symmetric at $\psi = \pi$ (180° rotation), so it is useful to clarify further. For example, Ershadi et al. (2024) suggested using "Up" and "Down" (for the two V polarizations), or "Left" and "Right" (for the two H polarizations). Where possible, we recommend that the instrument orientation is aligned to ice flow. That way, minimal coordinate transformations are necessary to interpret the radar result within the ice-flow model coordinate reference system.

Our polarization notation assumes vertical wave propagation and normal incidence with an interface in the x-y plane, but for generalizability we include notation for a zenith rotation from the z-axis, θ, of either the wave propagation vector or the anisotropy orientation. In the case of oblique wave propagation away from nadir (at some angle, θ), such as for side-looking spaceborne radars (Zebker & Van Zyl, 1991) or bistatic sounding (K. Matsuoka et al., 2009), it may be additionally useful to define separate coordinate systems for wave propagation in each direction (downward and upward) and polarization states referenced to each. Permittivity anisotropy is expressed as a cross section of the full permittivity ellipsoid, perpendicular to the direction of wave propagation, so zenith rotations can alter the expression by a factor of order $\cos(\theta)$ (Appendix II in K. Matsuoka et al., 2009). We therefore argue that small angles ($\theta < 5°$) can be considered vertical for most cases (i.e., $\cos(5°) = 0.99$), but oblique wave propagation may need to be considered for some cases, even with a small antenna separation (e.g., the standard 10 m for ApRES) such as in near-surface firn or thin ice shelves (e.g., <100 m).

Appendix B: Analogies to Seismic Observation of Ice Anisotropy

In some ways, seismic methods are analogous to the radar methods described in this review, and they too have been used for surveying of both intrinsic and extrinsic anisotropy. Some of the early work on seismic anisotropy in glaciology was on cold glacier ice and snow (e.g., Acharya, 1972; Bentley, 1971; Robinson, 1968), but theory suggests that melt-preferred orientation in temperate ice should also be measurable (Seltzer et al., 2024). In other ways, seismic methods are unique from radar sounding, with inherent differences in wave propagation, source mechanism, data acquisition, analytical methods, and relevant material properties, so they can complement one another well. For instance, active-source seismic methods cannot match the capacity of radar methods to scale beyond local ground-based experiments, but seismic methods are insensitive to electrical conductivity and may therefore aid the interpretation of radar observations through the discrimination of meteoric stratigraphy from COF (Diez et al., 2015). Conversely, the stratigraphy derived from radar measurements may be used to define a depth structure which then supports a more realistic glaciological interpretation from the seismic analysis (Kufner et al., 2023).

Elastic shear-wave (S-wave) splitting (Savage, 1999), a form of birefringence, is the seismic measurement that is most directly comparable to polarimetric radar sounding. A number of studies have used this technique to investigate COF in glacial firn and ice, using either naturally occurring ("passive") seismicity (e.g., Harland et al., 2013; Pearce et al., 2024) or human-generated ("active") seismic sources (e.g., Brisbourne et al., 2019; Lutz et al., 2020; Schlegel et al., 2019). With only limited measurements, it is difficult to isolate where along the wave path the splitting occurred; however, by using large seismic networks with thousands of events at the bed, multiple fabric types within the ice column can be distinguished (E. C. Smith et al., 2017; Kufner et al., 2023).

Longitudinal pressure waves (P-waves) do not have a direct analogy in radar sounding and can therefore be used as a complementary geophysical tool. Englacial P-wave reflectors have been identified toward the base of the ice column (e.g., Horgan et al., 2011), where radio echoes are less prevalent (Drews et al., 2009). One hypothesis is that those reflections are from a contrast of vertical anisotropy in COF (Horgan et al., 2008; A. M. Smith, 1996)—a material boundary with which vertically propagating radar would not be expected to interact—and attempts

have been made to quantify the strength of the COF contrast with seismic measurements (Hofstede et al., 2013; Horgan et al., 2011). In this way, seismic methods allow the discrimination of the full second-order orientation tensor of the fabric, through the combined use of both longitudinal P- and transverse S-waves (Picotti et al., 2015; Wittlinger & Farra, 2015), by leveraging a broader range of raypath geometries (Blankenship & Bentley, 1987), or by recording the full wavefield on three-component receivers (Kufner et al., 2023; Zhang et al., 2024). Vertical seismic profiling (VSP), using a borehole seismometer, permits measurements of seismic anisotropy using both P- and S-waves; the results of an initial survey of this type in the shear margin of Priestley Glacier were consistent with ultrasonic measurements on samples obtained at the site (Lutz et al., 2022). Subsequent development of an inverse modeling framework suggests that vertical seismic profiles could be used to infer generic COFs (Rathmann, Grinsted, et al., 2022).

Appendix C: The Poincaré Sphere

Throughout the manuscript, we use two parameters to conceptualize any polarization state: the phase, ϕ, and the rotation, γ, of the polarization ellipse. We visualize those parameters either by plotting each individually or by explicitly drawing the ellipse. Here, we offer an alternative visualization (Figure C1), bringing the two parameters

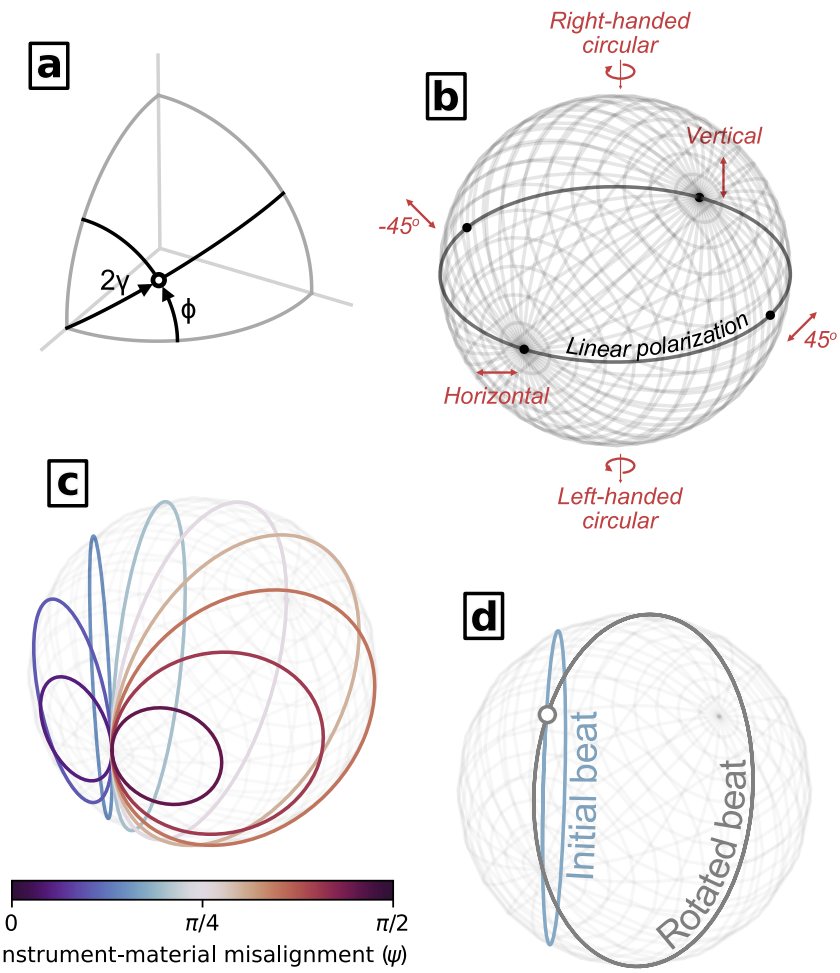

Figure C1. Visualizations with the Poincaré Sphere. (a) An octant of the sphere to illustrate the two parameters of interest, ϕ and γ. (b) The full sphere, with text for notable polarization states and a grid for lines of equal phase and rotation. (c) Birefringent transmission through media with uniform anisotropy (as in Figure 6). Colors correspond to azimuthal offsets between the material anisotropy (one of the principal axes) and the instrument (equivalent to the x-axis in Figures 6a–6f). (d) For a modeled scenario of principal-axis rotation (as in Figure 8a). The colored circle shows an initial beat signature, for depths above the principal-axis rotation (same as in panel (c)), the white dot indicates the polarization at the depth of principal-axis rotation, and the gray circle shows the beat signature for depths below rotation.

together onto the Poincaré Sphere (Poincaré, 1892), as is commonly done in textbooks which describe polarization (e.g., Collett, 2005; Huard, 1997) but less commonly used within the radioglaciology literature up to now (c.f., Doake, 1981). This Poincaré Sphere is often displayed using the Stokes Parameters (Stokes, 1851), but for consistency with the main article we maintain our original parameters here. Every point on the sphere represents a individual polarization state. At the poles of the sphere ($\gamma = 0$ and $\gamma = \frac{\pi}{2}$) the wave is linearly polarized in either the horizontal or vertical. The latitude-like lines between the poles are lines of equal rotation, and the great circles connecting the poles are lines of equal phase. Points at the surface of the sphere are full power, but there are also polarization states inside the sphere to indicate diminished power associated with losses due to scattering or attenuation.

Now, we revisualize scenarios from the main text with the Poincaré Sphere. For birefringence through a media with uniform anisotropy (as in Figure 6), the polarization state changes depending on the azimuth of the transmitted wave (linear polarization) relative to the principal axes. Each transmitted polarization traces a circle at the surface of the Poincaré Sphere, cutting across the lines of equal phase and rotation, and repeating in a cycle (the beat signature). Next, for an instantaneous rotation of the principal axes (as in Figure 8), the rotated principal axes will be out of alignment with the particular polarization state. Then, the beat signature below the rotation will be skewed (i.e., no longer symmetric between hemispheres) since it is overlaying transform functions from two distinct anisotropic layers. Away from the rotation, the beat *frequency* is unchanged since the magnitude of anisotropy is consistent across the rotation. However, the altered beat can be difficult to interpret without a wave propagation model, and even more so when the rotation is not instantaneous.

Conflict of Interest

The authors declare no conflicts of interest relevant to this study.

Data Availability Statement

The Jones-matrix model described in Section 3 and a series of computational notebooks with interactive examples to reproduce Figures 6–8, and similar model scenarios are made openly available by Hills (2025). All data presented in this article are from prior publications and openly available at archives provided therein (Bradford et al., 2013; Campbell & Phillips, 2021; Dahl-Jensen et al., 2023; Dall, 2020; Eisen et al., 2007; Franke et al., 2021; Gerber et al., 2023; Hills et al., 2023; Young & Dawson, 2021; Young, Schroeder, et al., 2021; Zeising & Humbert, 2022).

Acknowledgments

We thank two reviewers, David Prior and Bruce Campbell, for their thoughtful comments as well as the journal editors, Joshua Feinberg and Yusuke Yokoyama, and the entire editorial board at *Reviews of Geophysics*. A scientific illustrator, Dani Bergey, designed and illustrated Figure 1. BHH was supported by the National Science Foundation (NSF), Grant 2317927. MRE, FMO and RD were supported by Deutsche Forschungsgemeinschaft (DFG) Emmy Noether grant (Grant DR 822/3-1) and FMO was also supported by Studienstiftung des deutschen Volkes (doctoral scholarship). NMR was supported by the Independent Research Fund Denmark (DFF), Grant 2032-00364B. TAG was supported by Novo Nordisk Foundation Grant NNF23OC0081251. MRS was supported by NSF (Grant 2049302).

References

Aartsen, M. G., Abbasi, R., Ackermann, M., Adams, J., Aguilar, J. A., Ahlers, M., et al. (2021). IceCube-Gen2: The window to the extreme universe. *Journal of Physics G: Nuclear and Particle Physics*, *48*(6), 060501. https://doi.org/10.1088/1361-6471/abbd48

Abbasi, R., Abdou, Y., Abu-Zayyad, T., Actis, O., Adams, J., Aguilar, J., et al. (2011). Search for neutrino-induced cascades with five years of AMANDA data. *Astroparticle Physics*, *34*(6), 420–430. https://doi.org/10.1016/j.astropartphys.2010.10.007

Abbasi, R., Ackermann, M., Adams, J., Aggarwal, N., Aguilar, J., Ahlers, M., et al. (2024). In situ estimation of ice crystal properties at the South Pole using LED calibration data from the IceCube Neutrino Observatory. *The Cryosphere*, *18*(1), 75–102. https://doi.org/10.5194/tc-18-75-2024

Acharya, H. (1972). Surface-wave dispersion in Byrd Land, Antarctica. *Bulletin of the Seismological Society of America*, *62*(4), 955–959. https://doi.org/10.1785/BSSA0620040955

Achterberg, A., Ackermann, M., Adams, J., Ahrens, J., Andeen, K., Atlee, D., et al. (2006). First year performance of the IceCube neutrino telescope. *Astroparticle Physics*, *26*(3), 155–173. https://doi.org/10.1016/j.astropartphys.2006.06.007

Aguilar, J. A., Allison, P., Beatty, J., Bernhoff, H., Besson, D., Bingefors, N., et al. (2021). Design and sensitivity of the Radio Neutrino Observatory in Greenland (RNO-G). *Journal of Instrumentation*, *16*(3), P03025. https://doi.org/10.1088/1748-0221/16/03/P03025

Aguilar, J. A., Allison, P., Besson, D., Bishop, A., Botner, O., Bouma, S., et al. (2023). Radiofrequency ice dielectric measurements at Summit Station, Greenland. *Journal of Glaciology*, 1–12. https://doi.org/10.1017/jog.2023.72

Alley, R. B. (1988). Fabrics in Polar Ice Sheets: Development and prediction. *Science*, *240*(4851), 493–495. https://doi.org/10.1126/science.240.4851.493

Alley, R. B., & Fitzpatrick, J. J. (1999). Conditions for bubble elongation in cold ice-sheet ice. *Journal of Glaciology*, *45*(149), 147–153. https://doi.org/10.3189/S0022143000003129

Allison, P., Archambault, S., Auffenberg, J., Bard, R., Beatty, J., Beheler-Amass, M., et al. (2019). Measurement of the real dielectric permittivity ϵ_r of glacial ice. *Astroparticle Physics*, *108*, 63–73. https://doi.org/10.1016/j.astropartphys.2019.01.004

Allison, P., Auffenberg, J., Bard, R., Beatty, J., Besson, D., Böser, S., et al. (2012). Design and initial performance of the Askaryan Radio Array prototype EeV neutrino detector at the South Pole. *Astroparticle Physics*, *35*(7), 457–477. https://doi.org/10.1016/j.astropartphys.2011.11.010

Arenas-Pingarrón, Á., Corr, H. F., Robinson, C., Jordan, T. A., & Brennan, P. V. (2023). Polarimetric airborne scientific instrument, mark 2, an ice-sounding airborne synthetic aperture radar for subglacial 3D imagery. *IET Radar, Sonar & Navigation*, *17*(9), 1391–1404. https://doi.org/10.1049/rsn2.12428

Ariho, G., Paden, J. D., Hoffman, A., Christianson, K. A., & Holschuh, N. (2022). Joint estimation of ice sheet vertical velocity and englacial layer geometry from multipass synthetic aperture radar data. In *International symposium on phased array systems & technology (PAST)* (pp. 01–05). IEEE. https://doi.org/10.1109/PAST49659.2022.9974985

Axtell, C., Murray, T., Kulessa, B., Clark, R. A., & Gusmeroli, A. (2016). Improved accuracy of cross-borehole radar velocity models for ice property analysis. *Geophysics*, *81*(1), WA203–WA212. https://doi.org/10.1190/geo2015-0131.1

Azuma, N. (1994). A flow law for anisotropic ice and its application to ice sheets. *Earth and Planetary Science Letters*, *128*(3–4), 601–614. https://doi.org/10.1016/0012-821X(94)90173-2

Azuma, N., Wang, Y., Mori, K., Narita, H., Hondoh, T., Shoji, H., & Watanabe, O. (1999). Textures and fabrics in the Dome F (Antarctica) ice core. *Annals of Glaciology*, *29*, 163–168. https://doi.org/10.3189/172756499781821148

Babcock, E. L., Bradford, J. H., & Hall, C. (2015). Electrical anisotropy in sea ice and a dual-polarization radar system to mitigate the effects of preferential attenuation in imaging sea ice. *Cold Regions Science and Technology*, *118*, 105–111. https://doi.org/10.1016/j.coldregions.2015.06.012

Bain, A. (2019). *Crystal optics: Properties and applications*. Wiley.

Bentley, C. R. (1971). Seismic anisotropy in the West Antarctic Ice Sheet. Antarctic snow and ice studies II (Vol. *16*, pp. 131–177).

Bentley, C. R. (1975). Advances in geophysical exploration of ice sheets and glaciers. *Journal of Glaciology*, *15*(73), 113–135. https://doi.org/10.3189/S0022143000034328

Bienert, N. L., Schroeder, D. M., Peters, S. T., MacKie, E. J., Dawson, E. J., Siegfried, M. R., et al. (2022). Post-processing synchronized bistatic radar for long offset glacier sounding. *IEEE Transactions on Geoscience and Remote Sensing*, *60*, 1–17. https://doi.org/10.1109/TGRS.2022.3147172

Bienert, N. L., Schroeder, D. M., & Summers, P. (2022). Bistatic radar tomography of shear margins: Simulated temperature and basal material inversions. *IEEE Transactions on Geoscience and Remote Sensing*, *61*, 1–16. https://doi.org/10.1109/TGRS.2022.3213047

Bingham, R. G., & Siegert, M. J. (2007). Radio-echo sounding over polar ice masses. *Journal of Environmental & Engineering Geophysics*, *12*(1), 47–62. https://doi.org/10.2113/JEEG12.1.47

Blankenship, D. D., & Bentley, C. R. (1987). *Crystalline fabric of polar ice sheets inferred from seismic anisotropy* (Vol. 170, pp. 17–28). International Association of Hydrological Sciences Press.

Blankenship, D. D., Moussessian, A., Chapin, E., Young, D., Patterson, G., Plaut, J., et al. (2024). Radar for Europa assessment and sounding: Ocean to near-surface (REASON). *Space Science Reviews*, *220*(5), 51. https://doi.org/10.1007/s11214-024-01072-3

Bogorodskiĭ, V. V., Bentley, C. R., & Gudmandsen, P. (1985). *Radioglaciology* (Vol. 1). Springer Science & Business Media.

Booth, A. D., Christoffersen, P., Schoonman, C., Clarke, A., Hubbard, B., Law, R., et al. (2020). Distributed acoustic sensing of seismic properties in a borehole drilled on a fast-flowing Greenlandic outlet glacier. *Geophysical Research Letters*, *47*(13), e2020GL088148. https://doi.org/10.1029/2020GL088148

Bradford, J. H., Nichols, J., Harper, J. T., & Meierbachtol, T. (2013). Compressional and em wave velocity anisotropy in a temperate glacier due to basal crevasses, and implications for water content estimation. *Annals of Glaciology*, *54*(64), 168–178. https://doi.org/10.3189/2013AoG64A206

Brennan, P. V., Lok, L. B., Nicholls, K., & Corr, H. (2014). Phase-sensitive FMCW radar system for high-precision antarctic ice shelf profile monitoring. *IET Radar, Sonar & Navigation*, *8*(7), 776–786. https://doi.org/10.1049/iet-rsn.2013.0053

Brisbourne, A. M., Kendall, M., Kufner, S.-K., Hudson, T. S., & Smith, A. M. (2021). Downhole distributed acoustic seismic profiling at Skytrain Ice Rise, West Antarctica. *The Cryosphere*, *15*(7), 3443–3458. https://doi.org/10.5194/tc-15-3443-2021

Brisbourne, A. M., Martín, C., Smith, A. M., Baird, A. F., Kendall, J. M., & Kingslake, J. (2019). Constraining recent ice flow history at Korff ice rise, West Antarctica, using radar and seismic measurements of ice fabric. *Journal of Geophysical Research: Earth Surface*, *124*(1), 175–194. https://doi.org/10.1029/2018JF004776

Broquet, A., Wieczorek, M., & Fa, W. (2021). The composition of the south polar cap of Mars derived from orbital data. *Journal of Geophysical Research: Planets*, *126*(8), e2020JE006730. https://doi.org/10.1029/2020je006730

Brothers, T. C., & Holt, J. W. (2016). Three-dimensional structure and origin of a 1.8 km thick ice dome within Korolev Crater, Mars. *Geophysical Research Letters*, *43*(4), 1443–1449. https://doi.org/10.1002/2015GL066440

Bruzzone, L., Plaut, J., Alberti, G., Blankenship, D., Bovolo, F., Campbell, B., et al. (2013). RIME: Radar for icy moon exploration. In *International geoscience and remote sensing symposium (IGARSS)* (pp. 3907–3910). IEEE. https://doi.org/10.1109/IGARSS.2013.6723686

Budd, W. (1973). The development of crystal orientation fabrics in moving ice. *Zeitschrift fuer Gletscherkunde und Glazialgeologie*, *8*(1–2), 65–105.

Bussemer, P., Hehl, K., Kassam, S., & Kaganov, M. I. (1991). Electromagnetic wave propagation in polycrystalline materials: Effective medium approach. *Waves in Random Media*, *1*(2), 113–131. https://doi.org/10.1088/0959-7174/1/2/002

Calonne, N., Montagnat, M., Matzl, M., & Schneebeli, M. (2017). The layered evolution of fabric and microstructure of snow at Point Barnola, Central East Antarctica. *Earth and Planetary Science Letters*, *460*, 293–301. https://doi.org/10.1016/j.epsl.2016.11.041

Campbell, B., & Phillips, R. (2021). Mars reconnaissance orbiter shallow radar radargram data, mro-m-sharad-5-radargram-v2.0 [Dataset]. *NASA Planetary Data System*. https://doi.org/10.17189/yb1w-f075

Castelnau, O., Duval, P., Lebensohn, R. A., & Canova, G. R. (1996). Viscoplastic modeling of texture development in polycrystalline ice with a self-consistent approach: Comparison with bound estimates. *Journal of Geophysical Research*, *101*(B6), 13851–13868. https://doi.org/10.1029/96JB00412

Chauve, T., Montagnat, M., Dansereau, V., Saramito, P., Fourteau, K., & Tommasi, A. (2024). A physically-based formulation for texture evolution during dynamic recrystallization. A case study for ice. *Comptes Rendus Mecanique*, *352*(G1), 99–134. https://doi.org/10.5802/crmeca.243

Choy, T. C. (2015). *Effective medium theory: Principles and applications* (Vol. 165). Oxford University Press. https://doi.org/10.1093/acprof:oso/9780198705093.001.0001

Christianson, K., Jacobel, R. W., Horgan, H. J., Alley, R. B., Anandakrishnan, S., Holland, D. M., & Dallasanta, K. J. (2016). Basal conditions at the grounding zone of Whillans Ice Stream, West Antarctica, from ice-penetrating radar. *Journal of Geophysical Research: Earth Surface*, *121*(11), 1954–1983. https://doi.org/10.1002/2015JF003806

Collett, E. (2005). *Field guide to polarization*. SPIE.

Connolly, A. (2022). Impact of biaxial birefringence in polar ice at radio frequencies on signal polarizations in ultrahigh energy neutrino detection. *Physics Reviews D*, *105*(12), 123012. https://doi.org/10.1103/PhysRevD.105.123012

Cooper, M. A., Jordan, T. M., Schroeder, D. M., Siegert, M. J., Williams, C. N., & Bamber, J. L. (2019). Subglacial roughness of the Greenland Ice Sheet: Relationship with contemporary ice velocity and geology. *The Cryosphere*, *13*(11), 3093–3115. https://doi.org/10.5194/tc-13-3093-2019

Culberg, R., Schroeder, D. M., & Steinbrügge, G. (2022). Double ridge formation over shallow water sills on jupiter's moon europa. *Nature Communications*, *13*(1), 2007. https://doi.org/10.1038/s41467-022-29458-3

Dahl-Jensen, D., Steinhage, D., Lilien, D., Gogineni, P., & Eisen, O. (2023). UHF radar profile EGRIP [Dataset]. *ERDA*. https://doi.org/10.17894/UCPH.4F771760-FB08-4A97-9E48-818B8C7601D8

Dahl-Jensen, D., Wilhelms, F., Weikusat, I., Eisen, O., & Pattyn, F. (2021). *White paper — Ice coring for ice dynamics: The role of ice-core sciences in the understanding of past and present ice flow*. (Tech. Rep.). Crans-Montana, Switzerland: International Partnerships in Ice Core Sciences.

Dall, J. (2009). Polarimetric ice sounding at p-band: First results. In *International geoscience and remote sensing symposium (IGARSS)* (Vol. 2, p. II–1024). IEEE. https://doi.org/10.1109/IGARSS.2009.5418278

Dall, J. (2010). Ice sheet anisotropy measured with polarimetric ice sounding radar. In *International geoscience and remote sensing symposium (IGARSS)* (pp. 2507–2510). IEEE. https://doi.org/10.1109/IGARSS.2010.5653528

Dall, J. (2020). Estimation of crystal orientation fabric from airborne polarimetric ice sounding radar data. In *International geoscience and remote sensing symposium (IGARSS)* (pp. 2975–2978). IEEE. https://doi.org/10.1109/IGARSS39084.2020.9323437

Dall, J., Kristensen, S. S., Krozer, V., Hernández, C. C., Vidkjær, J., Kusk, A., et al. (2010). ESA's polarimetric airborne radar ice sounder (POLARIS): Design and first results. *IET Radar, Sonar & Navigation*, *4*(3), 488–496. https://doi.org/10.1049/iet-rsn.2009.0035

Dall, J., & Kusk, A. (2009). *P-band ice sounding radar demonstrator development; campaign report (Tech. Rep.)*. National Space Institute Technical University of Denmark.

Daubar, I., Hayes, A., Collins, G., Craft, K. L., Rathbun, J., Spencer, J. R., et al. (2024). Planned geological investigations of the Europa Clipper Mission. *Space Science Reviews*, *220*(1), 18. https://doi.org/10.1007/s11214-023-01036-z

Deaconu, C., Vieregg, A. G., Wissel, S. A., Bowen, J., Chipman, S., Gupta, A., et al. (2018). Measurements and modeling of near-surface radio propagation in glacial ice and implications for neutrino experiments. *Physics Reviews D*, *98*(4), 043010. https://doi.org/10.1103/PhysRevD.98.043010

De La Chapelle, S., Castelnau, O., Lipenkov, V., & Duval, P. (1998). Dynamic recrystallization and texture development in ice as revealed by the study of deep ice cores in Antarctica and Greenland. *Journal of Geophysical Research*, *103*(B3), 5091–5105. https://doi.org/10.1029/97JB02621

Diez, A., Eisen, O., Hofstede, C., Lambrecht, A., Mayer, C., Miller, H., et al. (2015). Seismic wave propagation in anisotropic ice – Part 2: Effects of crystal anisotropy in geophysical data. *The Cryosphere*, *9*(1), 385–398. https://doi.org/10.5194/tc-9-385-2015

Doake, C. (1981). Polarization of radio waves in ice sheets. *Geophysical Journal International*, *64*(2), 539–558. https://doi.org/10.1111/j.1365-246X.1981.tb02682.x

Doake, C., Corr, H. F., & Jenkins, A. (2002). Polarization of radio waves transmitted through Antarctic ice shelves. *Annals of Glaciology*, *34*, 165–170. https://doi.org/10.3189/172756402781817572

Doake, C., Corr, H. F., Jenkins, A., Nicholls, K. W., & Stewart, C. (2003). *Interpretation of polarimetric ice penetrating radar data over Antarctic ice shelves*. (Tech. Rep. No. 14). The Forum for Research into Ice Shelf Processes.

Dowdeswell, J. A., & Evans, S. (2004). Investigations of the form and flow of ice sheets and glaciers using radio-echo sounding. *Reports on Progress in Physics*, *67*(10), 1821–1861. https://doi.org/10.1088/0034-4885/67/10/R03

Drews, R., Eisen, O., Steinhage, D., Weikusat, I., Kipfstuhl, S., & Wilhelms, F. (2012). Potential mechanisms for anisotropy in ice-penetrating radar data. *Journal of Glaciology*, *58*(209), 613–624. https://doi.org/10.3189/2012JoG11J114

Drews, R., Eisen, O., Weikusat, I., Kipfstuhl, S., Lambrecht, A., Steinhage, D., et al. (2009). Layer disturbances and the radio-echo free zone in ice sheets. *The Cryosphere*, *3*(2), 195–203. https://doi.org/10.5194/tc-3-195-2009

Eisen, O., Hamann, I., Kipfstuhl, S., Steinhage, D., & Wilhelms, F. (2007). Direct evidence for continuous radar reflector originating from changes in crystal-orientation fabric. *The Cryosphere*, *1*(1), 1–10. https://doi.org/10.5194/tc-1-1-2007

Eisen, O., Wilhelms, F., Nixdorf, U., & Miller, H. (2003). Revealing the nature of radar reflections in ice: DEP-based FDTD forward modeling. *Geophysical Research Letters*, *30*(5). https://doi.org/10.1029/2002GL016403Ci

Ershadi, M. R., Drews, R., Hawkins, J. D., Elliott, J., Lines, A. P., Koch, I., & Eisen, O. (2024). Autonomous rover enables radar profiling of ice-fabric properties in Antarctica. *IEEE Transactions on Geoscience and Remote Sensing*, *62*, 1–9. (Conference Name: IEEE Transactions on Geoscience and Remote Sensing). https://doi.org/10.1109/TGRS.2024.3394594

Ershadi, M. R., Drews, R., Martín, C., Eisen, O., Ritz, C., Corr, H., et al. (2022). Polarimetric radar reveals the spatial distribution of ice fabric at domes and divides in East Antarctica. *The Cryosphere*, *16*(5), 1719–1739. https://doi.org/10.5194/tc-16-1719-2022

Fan, S., Hager, T. F., Prior, D. J., Cross, A. J., Goldsby, D. L., Qi, C., et al. (2020). Temperature and strain controls on ice deformation mechanisms: Insights from the microstructures of samples deformed to progressively higher strains at −10, −20 and −30°C. *The Cryosphere*, *14*(11), 3875–3905. https://doi.org/10.5194/tc-14-3875-2020

Faria, S. H. (2006a). Creep and recrystallization of large polycrystalline masses. I. General continuum theory. *Proceedings of the Royal Society A: Mathematical, Physical and Engineering Sciences*, *462*(2069), 1493–1514. https://doi.org/10.1098/rspa.2005.1610

Faria, S. H. (2006b). Creep and recrystallization of large polycrystalline masses. III. Continuum theory of ice sheets. *Proceedings of the Royal Society A: Mathematical, Physical and Engineering Sciences*, *462*(2073), 2797–2816. https://doi.org/10.1098/rspa.2006.1698

Faria, S. H., Weikusat, I., & Azuma, N. (2014a). The microstructure of polar ice. Part I: Highlights from ice core research. *Journal of Structural Geology*, *61*, 2–20. https://doi.org/10.1016/j.jsg.2013.09.010

Faria, S. H., Weikusat, I., & Azuma, N. (2014b). The microstructure of polar ice. Part II: State of the art. *Journal of Structural Geology*, *61*, 21–49. (Microdynamics of Ice). https://doi.org/10.1016/j.jsg.2013.11.003

Fichtner, A., Hofstede, C., Gebraad, L., Zunino, A., Zigone, D., & Eisen, O. (2023). Borehole fibre-optic seismology inside the Northeast Greenland Ice Stream. *Geophysical Journal International*, *235*(3), 2430–2441. https://doi.org/10.1093/gji/ggad344

Fichtner, A., Kennett, B. L., & Trampert, J. (2013). Separating intrinsic and apparent anisotropy. *Physics of the Earth and Planetary Interiors*, *219*, 11–20. https://doi.org/10.1016/j.pepi.2013.03.006

Fishbaugh, K. E., Hvidberg, C. S., Byrne, S., Russell, P. S., Herkenhoff, K. E., Winstrup, M., & Kirk, R. (2010). First high-resolution stratigraphic column of the martian north polar layered deposits. *Geophysical Research Letters*, *37*(7). https://doi.org/10.1029/2009gl041642

Fitzpatrick, J. J., Voigt, D. E., Fegyveresi, J. M., Stevens, N. T., Spencer, M. K., Cole-Dai, J., et al. (2014). Physical properties of the WAIS divide ice core. *Journal of Glaciology*, *60*(224), 1140–1154. https://doi.org/10.3189/2014JoG14J100

Flowers, G. E. (2015). Modelling water flow under glaciers and ice sheets Subject Areas. *Proceedings of the Royal Society A: Mathematical, Physical and Engineering Sciences*, *471*(2176), 20140907. https://doi.org/10.1098/rspa.2014.0907

Foss, F. J., II, Putzig, N. E., Campbell, B. A., Levin, S. A., Perry, M. R., Holt, J. W., et al. (2024). Producing 3d radargrams from orbital radar sounding data at Mars: History, results, methods, lessons and plans. *Icarus*, *419*, 115793. https://doi.org/10.1016/j.icarus.2023.115793

Fountain, A. G., Jacobel, R. W., Schlichting, R., & Jansson, P. (2005). Fractures as the main pathways of water flow in temperate glaciers. *Nature*, *433*(7026), 618–621. https://doi.org/10.1038/nature03296

Franke, S., Bons, P. D., Westhoff, J., Weikusat, I., Binder, T., Streng, K., et al. (2022). Holocene ice-stream shutdown and drainage basin reconfiguration in northeast Greenland. *Nature Geoscience*, *15*(12), 995–1001. https://doi.org/10.1038/s41561-022-01082-2

Franke, S., Jansen, D., Binder, T., Paden, J. D., Dörr, N., Gerber, T. A., et al. (2021). Ultra-wideband radar data over the shear margins and along flow lines at the onset region of the Northeast Greenland Ice Stream (NEGIS) [Dataset]. *PANGAEA*. https://doi.org/10.1594/PANGAEA.928569

Frémand, A. C., Bodart, J. A., Jordan, T. A., Ferraccioli, F., Robinson, C., Corr, H. F. J., et al. (2022). British Antarctic Survey's aerogeophysical data: Releasing 25 years of airborne gravity, magnetic, and radar datasets over Antarctica. *Earth System Science Data*, *14*(7), 3379–3410. https://doi.org/10.5194/essd-14-3379-2022

Fujita, S., Hirabayashi, M., Goto-Azuma, K., Dallmayr, R., Satow, K., Zheng, J., & Dahl-Jensen, D. (2014). Densification of layered firn of the ice sheet at NEEM, Greenland. *Journal of Glaciology*, *60*(223), 905–921. https://doi.org/10.3189/2014JoG14J006

Fujita, S., & Mae, S. (1993). Relation between ice sheet internal radio-echo reflections and ice fabric at Mizuho Station, Antarctica. *Annals of Glaciology*, *17*, 269–275. https://doi.org/10.3189/S0260305500012957

Fujita, S., & Mae, S. (1994). Causes and nature of ice-sheet radio-echo internal reflections estimated from the dielectric properties of ice. *Annals of Glaciology*, *20*, 80–86. https://doi.org/10.3189/1994AoG20-1-80-86

Fujita, S., Mae, S., & Matsuoka, T. (1993). Dielectric anisotropy in ice Ih at 9.7 GHz. *Annals of Glaciology*, *17*, 276–280. https://doi.org/10.3189/s0260305500012969

Fujita, S., Maeno, H., & Matsuoka, K. (2006). Radio-wave depolarization and scattering within ice sheets: A matrix-based model to link radar and ice-core measurements and its application. *Journal of Glaciology*, *52*(178), 407–424. https://doi.org/10.3189/172756506781828548

Fujita, S., Maeno, H., Uratsuka, S., Furukawa, T., Mae, S., Fujii, Y., & Watanabe, O. (1999). Nature of radio echo layering in the Antarctic ice sheet detected by a two-frequency experiment. *Journal of Geophysical Research*, *104*(B6), 13013–13024. https://doi.org/10.1029/1999JB900034

Fujita, S., Matsuoka, K., Maeno, H., & Furukawa, T. (2003). Scattering of VHF radio waves from within an ice sheet containing the vertical-girdle-type ice fabric and anisotropic reflection boundaries. *Annals of Glaciology*, *37*, 305–316. https://doi.org/10.3189/172756403781815979

Fujita, S., Matsuoka, T., Ishida, T., Matsuoka, K., & Mae, S. (2000). A summary of the complex dielectric permittivity of ice in the megahertz range and its applications for radar sounding of polar ice sheets. In *Physics of ice core records* (pp. 185–212). Hokkaido University Press.

Fujita, S., Nakawo, M., & Mae, S. (1987). Orientation of the 700-m Mizuho core and its strain history. In *Proceedings of the National Institute of Polar Research symposium on polar meteorology and glaciology* (Vol. 1, pp. 122–131).

Fujita, S., Okuyama, J., Hori, A., & Hondoh, T. (2009). Metamorphism of stratified firn at dome Fuji, Antarctica: A mechanism for local insolation modulation of gas transport conditions during bubble close off. *Journal of Geophysical Research*, *114*(F3). https://doi.org/10.1029/2008JF001143

Gagliardini, O., & Meyssonnier, J. (1999). Analytical derivations for the behavior and fabric evolution of a linear orthotropic ice polycrystal. *Journal of Geophysical Research*, *104*(B8), 17797–17809. https://doi.org/10.1029/1999JB900146

Garnett, J. M. (1904). XII. Colours in metal glasses and in metallic films. *Philosophical Transactions of the Royal Society of London - Series A: Containing Papers of a Mathematical or Physical Character*, *203*(359–371), 385–420.

Gerber, T. A., Lilien, D., Rathmann, N., Franke, S., Young, T. J., Valero-Delgado, F., et al. (2023). Crystal fabric anisotropy causes directional hardening of the Northeast Greenland Ice Stream. *Nature Communications*, *14*(1), 2653. https://doi.org/10.1038/s41467-023-38139-8

Gerber, T. A., Lilien, D. A., Nymand, N. F., Steinhage, D., Eisen, O., & Dahl-Jensen, D. (2025). Anisotropic scattering in radio-echo sounding: Insights from northeast Greenland. *The Cryosphere*, *19*(5), 1955–1971. https://doi.org/10.5194/tc-19-1955-2025

Gerbi, C., Mills, S., Clavette, R., Campbell, S., Bernsen, S., Clemens-Sewall, D., et al. (2021). Microstructures in a shear margin: Jarvis Glacier, Alaska. *Journal of Glaciology*, *67*(266), 1163–1176. https://doi.org/10.1017/jog.2021.62

Giannopoulos, A., & Diamanti, N. (2008). Numerical modelling of ground-penetrating radar response from rough subsurface interfaces. *Near Surface Geophysics*, *6*(6), 357–369. https://doi.org/10.3997/1873-0604.2008024

Gillet-Chaulet, F., Gagliardini, O., Meyssonnier, J., Montagnat, M., & Castelnau, O. (2005). A user-friendly anisotropic flow law for ice-sheet modelling. *Journal of Glaciology*, *51*(172), 3–14. https://doi.org/10.3189/172756505781829584

Gillet-Chaulet, F., Gagliardini, O., Meyssonnier, J., Zwinger, T., & Ruokolainen, J. (2006). Flow-induced anisotropy in polar ice and related ice-sheet flow modelling. *Journal of Non-Newtonian Fluid Mechanics*, *134*(1–3 SPEC. ISS.), 33–43. https://doi.org/10.1016/j.jnnfm.2005.11.005

Gödert, G. (2003). A mesoscopic approach for modelling texture evolution of polar ice including recrystallization phenomena. *Annals of Glaciology*, *37*, 23–28. https://doi.org/10.3189/172756403781815375

Gow, A. J., Meese, D., Alley, R., Fitzpatrick, J., Anandakrishnan, S., Woods, G., & Elder, B. (1997). Physical and structural properties of the Greenland ice sheet project 2 ice core: A review. *Journal of Geophysical Research*, *102*(C12), 26559–26575. https://doi.org/10.1029/97JC00165

Gow, A. J., & Williamson, T. (1976). *Rheological implications of the internal structure and crystal fabrics of the West Antarctic ice sheet as revealed by deep core drilling at Byrd Station*. Tech. Rep. No. 12 (Vol. 87). Cold Regions Research and Engineering Laboratory. https://doi.org/10.1130/0016-7606(1976)87⟨1665:RIOTIS⟩2.0.CO;2

Grasset, O., Dougherty, M., Coustenis, A., Bunce, E., Erd, C., Titov, D., et al. (2013). JUpiter ICy moons Explorer (JUICE): An ESA mission to orbit Ganymede and to characterise the Jupiter system. *Planetary and Space Science*, *78*, 1–21. https://doi.org/10.1016/j.pss.2012.12.002

Grinsted, A., Hvidberg, C. S., Lilien, D. A., Rathmann, N. M., Karlsson, N. B., Gerber, T., et al. (2022). Accelerating ice flow at the onset of the Northeast Greenland Ice Stream. *Nature Communications*, *13*(1), 5589. https://doi.org/10.1038/s41467-022-32999-2

Gudmandsen, P. (1975). Layer echoes in polar ice sheets. *Journal of Glaciology*, *15*(73), 95–101. https://doi.org/10.3189/S0022143000034304

Hale, R., Miller, H., Gogineni, S., Yan, J. B., Rodriguez-Morales, F., Leuschen, C., et al. (2016). Multi-channel ultra-wideband radar sounder and imager. In *International geoscience and remote sensing symposium (IGARSS)* (pp. 2112–2115). IEEE. https://doi.org/10.1109/IGARSS.2016.7729545

Hargreaves, N. D. (1977). The polarization of radio signals in the radio echo sounding of ice sheets. *Journal of Physics D: Applied Physics*, *10*(9), 1285–1304. https://doi.org/10.1088/0022-3727/10/9/012

Hargreaves, N. D. (1978). The radio-frequency birefringence of polar ice. *Journal of Glaciology*, *21*(85), 301–313. https://doi.org/10.3189/s0022143000033499

Harland, S., Kendall, J.-M., Stuart, G., Lloyd, G., Baird, A., Smith, A., et al. (2013). Deformation in Rutford Ice Stream, West Antarctica: Measuring shear-wave anisotropy from icequakes. *Annals of Glaciology*, *54*(64), 105–114. https://doi.org/10.3189/2013AoG64A033

Harper, J. T. (1993). Glacier terminus fluctuations on Mount Baker, Washington, U.S.A., 1940-1990, and climatic variations. *Arctic and Alpine Research*, *25*(4), 332–340. https://doi.org/10.2307/1551916

Harrison, C. H. (1973). Radio echo sounding of horizontal layers in ice. *Journal of Glaciology*, *12*(66), 383–397. https://doi.org/10.3189/S0022143000031804

Heggy, E., Scabbia, G., Bruzzone, L., & Pappalardo, R. T. (2017). Radar probing of Jovian icy moons: Understanding subsurface water and structure detectability in the JUICE and Europa missions. *Icarus*, *285*, 237–251. https://doi.org/10.1016/j.icarus.2016.11.039

Heliere, F., Lin, C.-C., Corr, H., & Vaughan, D. (2007). Radio echo sounding of Pine Island Glacier, West Antarctica: Aperture synthesis processing and analysis of feasibility from space. *IEEE Transactions on Geoscience and Remote Sensing*, *45*(8), 2573–2582. https://doi.org/10.1109/TGRS.2007.897433

Hempel, L., Thyssen, F., Gundestrup, N., Clausen, H. B., & Miller, H. (2000). A comparison of radio-echo sounding data and electrical conductivity of the GRIP ice core. *Journal of Glaciology*, *46*(154), 369–374. https://doi.org/10.3189/172756500781833070

Hills, B. H. (2025). Benhills/effmed-ice: Pre-release for reviews of geophysics (v1.0.2) [computationalnotebook]. *Zenodo*. https://doi.org/10.5281/zenodo.12775526

Hills, B. H., Holschuh, A., Nicholas, H., Fudge, T. J., Horlings, A., Erwin, E., et al. (2023). Hercules dome ApRES data [Dataset]. *U.S. Antarctic Program Data Center*. https://doi.org/10.15784/601739

Hills, B. H., Holschuh, N., Hoffman, A., Horlings, A., Erwin, E., Kirkpatrick, L., et al. (2025). Radar-derived crystal orientation fabric suggests dynamic stability at the summit of hercules dome. *Journal of Geophysical Research: Earth Surface*, *130*(3), e2023JF007588. https://doi.org/10.1029/2023JF007588

Hoffman, A. O., Christianson, K., Holschuh, N., Case, E., Kingslake, J., & Arthern, R. (2022). The impact of basal roughness on inland Thwaites glacier sliding. *Geophysical Research Letters*, *49*(14), 1–11. https://doi.org/10.1029/2021GL096564

Hoffman, M., & Price, S. (2014). Feedbacks between coupled subglacial hydrology and glacier dynamics. *Journal of Geophysical Research: Earth Surface*, *119*(3), 414–436. https://doi.org/10.1002/2013JF002943

Hofstede, C., Eisen, O., Diez, A., Jansen, D., Kristoffersen, Y., Lambrecht, A., & Mayer, C. (2013). Investigating englacial reflections with vibro- and explosive-seismic surveys at Halvfarryggen Ice Dome, Antarctica. *Annals of Glaciology*, *54*(64), 189–200. https://doi.org/10.3189/2013AoG64A064

Hogan, K. A., Larter, R. D., Graham, A. G., Arthern, R., Kirkham, J. D., Totten Minzoni, R., et al. (2020). Revealing the former bed of Thwaites Glacier using sea-floor bathymetry: Implications for warm-water routing and bed controls on ice flow and buttressing. *The Cryosphere*, *14*(9), 2883–2908. https://doi.org/10.5194/tc-14-2883-2020

Holschuh, N., Christianson, K., Anandakrishnan, S., Alley, R. B., & Jacobel, R. W. (2016). Constraining attenuation uncertainty in common midpoint radar surveys of ice sheets. *Journal of Geophysical Research: Earth Surface*, *121*(10), 1876–1890. https://doi.org/10.1002/2016JF003942

Holschuh, N., Christianson, K., Paden, J., Alley, R. B., & Anandakrishnan, S. (2020). Linking postglacial landscapes to glacier dynamics using swath radar at Thwaites glacier, Antarctica. *Geology*, *48*(3), 268–272. https://doi.org/10.1130/G46772.1

Holschuh, N., Lilien, D., & Christianson, K. (2019). Thermal weakening, convergent flow, and vertical heat transport in the Northeast Greenland Ice Stream shear margins. *Geophysical Research Letters*, *46*(14), 8184–8193. https://doi.org/10.1029/2019GL083436

Horgan, H. J., Anandakrishnan, S., Alley, R. B., Burkett, P. G., & Peters, L. E. (2011). Englacial seismic reflectivity: Imaging crystal-orientation fabric in West Antarctica. *Journal of Glaciology*, *57*(204), 639–650. https://doi.org/10.3189/002214311797409686

Horgan, H. J., Anandakrishnan, S., Alley, R. B., Peters, L. E., Tsoflias, G. P., Voigt, D. E., & Winberry, J. P. (2008). Complex fabric development revealed by englacial seismic reflectivity: Jakobshavn Isbræ, Greenland. *Geophysical Research Letters*, *35*(10). https://doi.org/10.1029/2008GL033712

Howat, I. M., Porter, C., Smith, B. E., Noh, M.-J., & Morin, P. (2019). The reference elevation model of Antarctica. *The Cryosphere*, 1–16. https://doi.org/10.5194/tc-2018-240

Huard, S. (1997). *Polarization of light*. Masson.

Hudleston, P. J. (2015). Structures and fabrics in glacial ice: A review. *Journal of Structural Geology*, *81*, 1–27. https://doi.org/10.1016/j.jsg.2015.09.003

Hunter, N. J. R., Wilson, C. J. L., & Luzin, V. (2023). Crystallographic preferred orientation (CPO) patterns in uniaxially compressed deuterated ice: Quantitative analysis of historical data. *Journal of Glaciology*, *69*(276), 737–748. https://doi.org/10.1017/jog.2022.95

IceCube. (2013). Evidence for high-energy extraterrestrial neutrinos at the IceCube detector. *Science*, *342*(6161), 1242856. https://doi.org/10.1126/science.1242856

Jacka, T. H., & Maccagnan, M. (1984). Ice crystallographic and strain rate changes with strain in compression and extension. *Cold Regions Science and Technology*, *8*(3), 269–286. https://doi.org/10.1016/0165-232X(84)90058-2

Jackson, M., & Kamb, B. (1997). The marginal shear stress of Ice Stream B, West Antarctica. *Journal of Glaciology*, *43*(145), 415–426. https://doi.org/10.3189/S0022143000035000

Jansen, D., Franke, S., Bauer, C. C., Binder, T., Dahl-Jensen, D., Eichler, J., et al. (2024). Shear margins in upper half of Northeast Greenland Ice Stream were established two millennia ago. *Nature Communications*, *15*(1), 1193. (Number: 1 Publisher: Nature Publishing Group). https://doi.org/10.1038/s41467-024-45021-8

Jennings, S. J., & Hambrey, M. J. (2021). Structures and deformation in glaciers and ice sheets. *Reviews of Geophysics*, *59*(3), e2021RG000743. https://doi.org/10.1029/2021RG000743

Jiracek, G. R. (1967). *Radio sounding of antarctic ice (Tech. Rep.)*. The University of Wisconsin Geophysical and Polar Research Center.

Jordan, T. M., Besson, D. Z., Kravchenko, I., Latif, U., Madison, B., Nokikov, A., & Shultz, A. (2020). Modeling ice birefringence and oblique radio wave propagation for neutrino detection at the South Pole. *Annals of Glaciology*, *61*(81), 84–91. https://doi.org/10.1017/aog.2020.18

Jordan, T. M., Martín, C., Brisbourne, A. M., Schroeder, D. M., & Smith, A. M. (2022). Radar characterization of ice crystal orientation fabric and anisotropic viscosity within an Antarctic Ice Stream. *Journal of Geophysical Research: Earth Surface*, *127*(6), 1–24. https://doi.org/10.1029/2022JF006673

Jordan, T. M., Schroeder, D. M., Castelletti, D., Li, J., & Dall, J. (2019). A polarimetric coherence method to determine ice crystal orientation fabric from radar sounding: Application to the NEEM Ice Core Region. *IEEE Transactions on Geoscience and Remote Sensing*, *57*(11), 8641–8657. https://doi.org/10.1109/TGRS.2019.2921980

Jordan, T. M., Schroeder, D. M., Cooper, W., & Siegfried, M. R. (2020). Estimation of ice fabric within Whillans Ice Stream using polarimetric phase-sensitive radar sounding. *Annals of Glaciology*, *61*(81), 74–83. https://doi.org/10.1017/aog.2020.6

Joughin, I., Smith, B. E., Howat, I. M., Scambos, T., & Moon, T. (2010). Greenland flow variability from ice-sheet-wide velocity mapping. *Journal of Glaciology*, *56*(197), 415–430. https://doi.org/10.3189/002214310792447734

Joughin, I., Smith, B. E., & Medley, B. (2014). Marine ice sheet collapse potentially under way for the Thwaites Glacier Basin, West Antarctica. *Science*, *344*(6185), 735–738. https://doi.org/10.1126/science.1249055

Journaux, B., Chauve, T., Montagnat, M., Tommasi, A., Barou, F., Mainprice, D., & Gest, L. (2019). Recrystallization processes, microstructure and crystallographic preferred orientation evolution in polycrystalline ice during high-temperature simple shear. *The Cryosphere*, *13*(5), 1495–1511. https://doi.org/10.5194/tc-13-1495-2019

Kamb, W. B. (1961). The glide direction in ice. *Journal of Glaciology*, *3*(30), 1097–1106. https://doi.org/10.3189/S0022143000017500

Kaundinya, S., Taylor, L., Sarkar, U. D., Occhiogrosso, V., Mai, H., Hoffman, A., et al. (2023). Uwb uhf dual-polarization ice-penetrating radar: Development and Antarctic field test. In *International geoscience and remote sensing symposium (IGARSS)* (pp. 48–51). IEEE. https://doi.org/10.1109/IGARSS52108.2023.10282578

Kingslake, J., Martín, C., Arthern, R. J., Corr, H. F., & King, E. C. (2016). Ice-flow reorganization in West Antarctica 2.5 kyr ago dated using radar-derived englacial flow velocities. *Geophysical Research Letters*, *43*(17), 9103–9112. https://doi.org/10.1002/2016GL070278

Kipfstuhl, S., Pauer, F., Kuhs, W. F., & Shoji, H. (2001). Air bubbles and Clathrate hydrates in the transition zone of the NGRIP Deep Ice Core. *Geophysical Research Letters*, *28*(4), 591–594. https://doi.org/10.1029/1999GL006094

Kluskiewicz, D., Waddington, E. D., Anandakrishnan, S., Voigt, D. E., Matsuoka, K., & McCarthy, M. P. (2017). Sonic methods for measuring crystal orientation fabric in ice, and results from the West Antarctic Ice Sheet (WAIS) divide. *Journal of Glaciology*, *63*(240), 603–617. https://doi.org/10.1017/jog.2017.20

Kravchenko, I., Besson, D., Ramos, A., & Remmers, J. (2011). Radio frequency birefringence in south polar ice and implications for neutrino reconstruction. *Astroparticle Physics*, *34*(10), 755–768. https://doi.org/10.1016/j.astropartphys.2011.01.008

Kufner, S.-K., Wookey, J., Brisbourne, A. M., Martín, C., Hudson, T. S., Kendall, J. M., & Smith, A. M. (2023). Strongly depth-dependent ice fabric in a fast-flowing Antarctic ice stream revealed with icequake observations. *Journal of Geophysical Research: Earth Surface*, *128*(3), e2022JF006853. https://doi.org/10.1029/2022JF006853

Landauer, J. K., & Plumb, H. (1956). *Measurements on anisotropy of thermal conductivity of ice (Tech. Rep.)*. Hanover, New Hampshire: U.S. Army Corps of Engineers Snow Ice and Permafrost Research Establishment.

Langhammer, L., Rabenstein, L., Schmid, L., Bauder, A., Grab, M., Schaer, P., & Maurer, H. (2019). Glacier bed surveying with helicopter-borne dual-polarization ground-penetrating radar. *Journal of Glaciology*, *65*(249), 123–135. https://doi.org/10.1017/jog.2018.99

Lee, J.-S., Hoppel, K. W., Mango, S. A., & Miller, A. R. (1994). Intensity and phase statistics of multilook polarimetric and interferometric SAR imagery. *IEEE Transactions on Geoscience and Remote Sensing*, *32*(5), 1017–1028. https://doi.org/10.1109/36.312890

Leinss, S., Löwe, H., Proksch, M., Lemmetyinen, J., Wiesmann, A., & Hajnsek, I. (2016). Anisotropy of seasonal snow measured by polarimetric phase differences in radar time series. *The Cryosphere*, *10*(4), 1771–1797. https://doi.org/10.5194/tc-10-1771-2016

Li, J., González, J. A., Leuschen, C., Harish, A., Gogineni, P., Montagnat, M., et al. (2018). Multi-channel and multi-polarization radar measurements around the NEEM site. *The Cryosphere*, *12*(8), 2689–2705. https://doi.org/10.5194/tc-12-2689-2018

Li, L., Yan, J.-B., O'Neill, C., Simpson, C. D., & Gogineni, S. P. (2022). Coplanar side-fed tightly coupled ultra-wideband array for polar ice sounding. *IEEE Transactions on Antennas and Propagation*, *70*(6), 4331–4341. https://doi.org/10.1109/TAP.2021.3138544

Lilien, D. A., Rathmann, N. M., Hvidberg, C. S., & Dahl-Jensen, D. (2021). Modeling ice-crystal fabric as a proxy for ice-stream stability. *Journal of Geophysical Research: Earth Surface*, *126*(9), 1–25. https://doi.org/10.1029/2021JF006306

Lilien, D. A., Rathmann, N. M., Hvidberg, C. S., Grinsted, A., Ershadi, M. R., Drews, R., & Dahl-Jensen, D. (2023). Simulating higher-order fabric structure in a coupled, anisotropic ice-flow model: Application to Dome C. *Journal of Glaciology*, *69*(278), 1–20. https://doi.org/10.1017/jog.2023.78

Llorens, M.-G., Griera, A., Bons, P. D., Weikusat, I., Prior, D. J., Gomez-Rivas, E., et al. (2022). Can changes in deformation regimes be inferred from crystallographic preferred orientations in polar ice? *The Cryosphere*, *16*(5), 2009–2024. https://doi.org/10.5194/tc-16-2009-2022

Long, D., & Ulaby, F. (2015). *Microwave radar and adiometric remote sensing*. Artech.

Long, M. D., & Becker, T. W. (2010). Mantle dynamics and seismic anisotropy. *Earth and Planetary Science Letters*, *297*(3–4), 341–354. https://doi.org/10.1016/j.epsl.2010.06.036

Lunine, J. I. (2017). Ocean worlds exploration. *Acta Astronautica*, *131*, 123–130. https://doi.org/10.1016/j.actaastro.2016.11.017

Lutz, F., Eccles, J., Prior, D. J., Craw, L., Fan, S., Hulbe, C., et al. (2020). Constraining ice shelf anisotropy using shear wave splitting measurements from active-source borehole seismics. *Journal of Geophysical Research: Earth Surface*, *125*(9), e2020JF005707. https://doi.org/10.1029/2020JF005707

Lutz, F., Prior, D. J., Still, H., Bowman, M. H., Boucinhas, B., Craw, L., et al. (2022). Ultrasonic and seismic constraints on crystallographic preferred orientations of the Priestley Glacier shear margin, Antarctica. *The Cryosphere*, *16*(8), 3313–3329. https://doi.org/10.5194/tc-16-3313-2022

Lytle, V., & Jezek, K. (1994). Dielectric permittivity and scattering measurements of Greenland firn at 26.5-40 GHz. *IEEE Transactions on Geoscience and Remote Sensing*, *32*(2), 290–295. https://doi.org/10.1109/36.295044

Ma, Y., Gagliardini, O., Ritz, C., Gillet-Chaulet, F., Durand, G., & Montagnat, M. (2010). Enhancement factors for grounded ice and ice shelves inferred from an anisotropic ice-flow model. *Journal of Glaciology*, *56*(199), 805–812. https://doi.org/10.3189/002214310794457209

MacGregor, J. A., Winebrenner, D. P., Conway, H., Matsuoka, K., Mayewski, P. A., & Clow, G. D. (2007). Modeling englacial radar attenuation at Siple Dome, West Antarctica, using ice chemistry and temperature data. *Journal of Geophysical Research*, *112*(3), 1–14. https://doi.org/10.1029/2006JF000717

Martín, C., Hindmarsh, R. C., & Navarro, F. J. (2009). On the effects of divide migration, along-ridge flow, and basal sliding on isochrones near an ice divide. *Journal of Geophysical Research*, *114*(2), 1–17. https://doi.org/10.1029/2008JF001025

Matsouka, K., Thorsteinsson, T., Björnsson, H., & Waddington, E. D. (2007). Anisotropic radio-wave scattering from englacial water regimes, Mýrdalsjökull, Iceland. *Journal of Glaciology*, *53*(182), 473–478. https://doi.org/10.3189/002214307783258422

Matsuoka, K., Furukawa, T., Fujita, S., Maeno, H., Uratsuka, S., Naruse, R., & Watanabe, O. (2003). Crystal orientation fabrics within the Antarctic ice sheet revealed by a multipolarization plane and dual-frequency radar survey. *Journal of Geophysical Research*, *108*(B10). https://doi.org/10.1029/2003jb002425

Matsuoka, K., Power, D., Fujita, S., & Raymond, C. F. (2012). Rapid development of anisotropic ice-crystal-alignment fabrics inferred from englacial radar polarimetry, central West Antarctica. *Journal of Geophysical Research*, *117*(3), 1–16. https://doi.org/10.1029/2012JF002440

Matsuoka, K., Uratsuka, S., Fujita, S., & Nishio, F. (2004). Ice-flow-induced scattering zone within the Antarctic ice sheet revealed by high-frequency airborne radar. *Journal of Glaciology*, *50*(170), 382–388. https://doi.org/10.3189/172756504781829891

Matsuoka, K., Wilen, L., Hurley, S. P., & Raymond, C. F. (2009). Effects of birefringence within ice sheets on obliquely propagating radio waves. *IEEE Transactions on Geoscience and Remote Sensing*, *47*(5), 1429–1443. https://doi.org/10.1109/TGRS.2008.2005201

Matsuoka, T., Fujita, S., Morishima, S., & Mae, S. (1997). Precise measurement of dielectric anisotropy in ice Ih at 39 GHz. *Journal of Applied Physics*, *81*(5), 2344–2348. https://doi.org/10.1063/1.364238

Maurel, A., Lund, F., & Montagnat, M. (2015). Propagation of elastic waves through textured polycrystals: Application to ice. *Proceedings of the Royal Society A: Mathematical, Physical and Engineering Sciences*, *471*(2177), 20140988. https://doi.org/10.1098/rspa.2014.0988

McCormack, F. S., Warner, R. C., Seroussi, H., Dow, C. F., Roberts, J. L., & Treverrow, A. (2022). Modeling the deformation regime of Thwaites Glacier, West Antarctica, using a simple flow relation for ice anisotropy (ESTAR). *Journal of Geophysical Research: Earth Surface*, *127*(3), e2021JF006332. https://doi.org/10.1029/2021JF006332

Meier, M. F., Kamb, W. B., Allen, C. R., & Sharp, R. P. (1974). Flow of blue glacier, Olympic Mountains, Washington, U.S.A. *Journal of Glaciology*, *13*(68), 187–212. https://doi.org/10.3189/S0022143000023029

Miles, B. W. J., Stokes, C. R., Jamieson, S. S. R., Jordan, J. R., Gudmundsson, G. H., & Jenkins, A. (2022). High spatial and temporal variability in Antarctic ice discharge linked to ice shelf buttressing and bed geometry. *Scientific Reports*, *12*(1), 10968. https://doi.org/10.1038/s41598-022-13517-2

Minchew, B. M., Meyer, C. R., Robel, A. A., Gudmundsson, G. H., & Simons, M. (2018). Processes controlling the downstream evolution of ice rheology in glacier shear margins: Case study on Rutford Ice Stream, West Antarctica. *Journal of Glaciology*, *64*(246), 1–12. https://doi.org/10.1017/jog.2018.47

Mojtabavi, S., Eisen, O., Franke, S., Jansen, D., Steinhage, D., Paden, J., et al. (2022). Origin of englacial stratigraphy at three deep ice core sites of the Greenland Ice Sheet by synthetic radar modelling. *Journal of Glaciology*, *68*(270), 799–811. https://doi.org/10.1017/jog.2021.137

Monz, M. E., Hudleston, P. J., Prior, D. J., Michels, Z., Fan, S., Negrini, M., et al. (2021). Full crystallographic orientation (*c* and *a* axes) of warm, coarse-grained ice in a shear-dominated setting: A case study, Storglaciären, Sweden. *The Cryosphere*, *15*(1), 303–324. https://doi.org/10.5194/tc-15-303-2021

Mouginot, J., Rignot, E., & Scheuchl, B. (2019). Continent-wide, interferometric SAR phase, mapping of Antarctic ice velocity. *Geophysical Research Letters*, *46*(16), 9710–9718. https://doi.org/10.1029/2019GL083826

Murray, T., Stuart, G. W., Fry, M., Gamble, N. H., & Crabtree, M. D. (2000). Englacial water distribution in a temperate glacier from surface and borehole radar velocity analysis. *Journal of Glaciology*, *46*(154), 389–398. https://doi.org/10.3189/172756500781833188

Nicholls, K. W., Corr, H. F., Stewart, C. L., Lok, L. B., Brennan, P. V., & Vaughan, D. G. (2015). Instruments and methods: A ground-based radar for measuring vertical strain rates and time-varying basal melt rates in ice sheets and shelves. *Journal of Glaciology*, *61*(230), 1079–1087. https://doi.org/10.3189/2015JoG15J073

Nimmo, F., & Pappalardo, R. T. (2016). Ocean worlds in the outer solar system. *Journal of Geophysical Research: Planets*, *121*(8), 1378–1399. https://doi.org/10.1002/2016JE005081

Nobes, D. (1999). The directional dependence of the ground penetrating radar response on the accumulation zones of temperate alpine glaciers. *First Break*, *17*(7), 249–259. https://doi.org/10.1046/j.1365-2397.1999.00028.x

Nye, J. F. (1985). *Physical properties of crystals: Their representation by tensors and matrices*. Oxford University Press.

Nymand, N. F., Lilien, D. A., Gerber, T. A., Hvidberg, C. S., Steinhage, D., Gogineni, P., et al. (2025). Double reflections in polarized radar data reveal ice fabric in the north east Greenland ice stream. *Geophysical Research Letters*, *52*(3), e2024GL110453. https://doi.org/10.1029/2024GL110453

Oraschewski, F. M., Ershadi, M. R., & Drews, R. (2025). Polarimetric wide-angle radar detects competing signatures of ice fabric and structural firn anisotropy. *Geophysical Research Letters*, *52*(14), e2024GL113096. https://doi.org/10.1029/2024gl113096

Otosaka, I. N., Shepherd, A., Ivins, E. R., Schlegel, N.-J., Amory, C., van den Broeke, M. R., et al. (2023). Mass balance of the Greenland and Antarctic ice sheets from 1992 to 2020. *Earth System Science Data*, *15*(4), 1597–1616. https://doi.org/10.5194/essd-15-1597-2023

Paden, J., Allen, C., Gogineni, S., Jezek, K., Dahl-Jensen, D., & Larsen, L. (2005). Wideband measurements of ice sheet attenuation and basal scattering. *IEEE Geoscience and Remote Sensing Letters*, *2*(2), 164–168. https://doi.org/10.1109/LGRS.2004.842474

Pappalardo, R. T., Buratti, B. J., Korth, H., Senske, D. A., Blaney, D. L., Blankenship, D. D., et al. (2024). Science overview of the Europa Clipper Mission. *Space Science Reviews*, *220*(4), 1–58. https://doi.org/10.1007/s11214-024-01070-5

Paren, J. G. (1981). Reflection coefficient at a dielectric interface. *Journal of Glaciology*, *27*(95), 203–204. https://doi.org/10.3189/S0022143000011400

Passler, N. C., Jeannin, M., & Paarmann, A. (2020). Layer-resolved absorption of light in arbitrarily anisotropic heterostructures. *Physical Review B*, *101*(16), 1–12. https://doi.org/10.1103/PhysRevB.101.165425

Passler, N. C., & Paarmann, A. (2017). Generalized 4 × 4 matrix formalism for light propagation in anisotropic stratified media: Study of surface phonon polaritons in polar dielectric heterostructures. *Journal of the Optical Society of America B*, *34*(10), 2128. https://doi.org/10.1364/josab.34.002128

Pauling, L. (1935). The structure and entropy of ice and of other crystals with some randomness of atomic arrangement. *Journal of the American Chemical Society*, *57*(12), 2680–2684. https://doi.org/10.1021/ja01315a102

Pearce, E., Zigone, D., Hofstede, C., Fichtner, A., Rimpot, J., Rasmussen, S. O., et al. (2024). Firn seismic anisotropy in the Northeast Greenland Ice Stream from ambient-noise surface waves. *The Cryosphere*, *18*(10), 4917–4932. https://doi.org/10.5194/tc-18-4917-2024

Peters, M. E., Blankenship, D. D., & Morse, D. L. (2005). Analysis techniques for coherent airborne radar sounding: Application to West Antarctic ice streams. *Journal of Geophysical Research*, *110*(B6). https://doi.org/10.1029/2004JB003222

Phillips, R. J., Zuber, M. T., Smrekar, S. E., Mellon, M. T., Head, J. W., Tanaka, K. L., et al. (2008). Mars north polar deposits: Stratigraphy, age, and geodynamical response. *Science*, *320*(5880), 1182–1185. https://doi.org/10.1126/science.1157546

Piazolo, S., Wilson, C. J. L., Luzin, V., Brouzet, C., & Peternell, M. (2013). Dynamics of ice mass deformation: Linking processes to rheology, texture, and microstructure. *Geochemistry, Geophysics, Geosystems*, *14*(10), 4185–4194. https://doi.org/10.1002/ggge.20246

Picardi, G., Biccari, D., Seu, R., Marinangeli, L., Johnson, W., Jordan, R., et al. (2004). Performance and surface scattering models for the Mars Advanced Radar for Subsurface and Ionosphere Sounding (MARSIS). *Planetary and Space Science*, *52*(1–3), 149–156. https://doi.org/10.1016/j.pss.2003.08.020

Picardi, G., Plaut, J. J., Biccari, D., Bombaci, O., Calabrese, D., Cartacci, M., et al. (2005). Radar soundings of the subsurface of Mars. *Science*, *310*(5756), 1925–1928. https://doi.org/10.1126/science.1122165

Picotti, S., Vuan, A., Carcione, J. M., Horgan, H. J., & Anandakrishnan, S. (2015). Anisotropy and crystalline fabric of Whillans Ice Stream (West Antarctica) inferred from multicomponent seismic data. *Journal of Geophysical Research: Solid Earth*, *120*(6), 4237–4262. https://doi.org/10.1002/2014JB011591

Plaut, J. J., Picardi, G., Safaeinili, A., Ivanov, A. B., Milkovich, S. M., Cicchetti, A., et al. (2007). Subsurface radar sounding of the south polar layered deposits of Mars. *Science*, *316*(5821), 92–95. https://doi.org/10.1126/science.1139672

Plaut, J. J., Safaeinili, A., Holt, J. W., Phillips, R. J., Head III, J. W., Seu, R., et al. (2009). Radar evidence for ice in lobate debris aprons in the mid-northern latitudes of Mars. *Geophysical Research Letters*, *36*(2). https://doi.org/10.1029/2008GL036379

Poincaré, H. (1892). *Théorie mathématique de la lumière* (Vol. 2). MI MISHCHENKO AND LD TRAVIS, 44. (georges carré, paris).

Prior-Jones, M. R., Bagshaw, E. A., Lees, J., Clare, L., Burrow, S., Werder, M. A., et al. (2021). Cryoegg: Development and field trials of a wireless subglacial probe for deep, fast-moving ice. *Journal of Glaciology*, *67*(264), 627–640. https://doi.org/10.1017/jog.2021.16

Pritchard, H. D., Fretwell, P. T., Fremand, A. C., Bodart, J. A., Kirkham, J. D., Aitken, A., et al. (2025). Bedmap3 updated ice bed, surface and thickness gridded datasets for Antarctica. *Scientific Data*, *12*(1), 414. https://doi.org/10.1038/s41597-025-04672-y

Prohira, S., de Vries, K. D., Allison, P., Beatty, J., Besson, D., Connolly, A., et al. (2021). The radar echo telescope for cosmic rays: Pathfinder experiment for a next-generation neutrino observatory. *Physics Reviews D*, *104*(10), 102006. https://doi.org/10.1103/PhysRevD.104.102006

Qi, C., Prior, D. J., Craw, L., Fan, S., Llorens, M. G., Griera, A., et al. (2019). Crystallographic preferred orientations of ice deformed in direct-shear experiments at low temperatures. *The Cryosphere*, *13*(1), 351–371. https://doi.org/10.5194/tc-13-351-2019

Radzevicius, S. J., & Daniels, J. J. (2000). Ground penetrating radar polarization and scattering from cylinders. *Journal of Applied Geophysics*, *45*(2), 111–125. https://doi.org/10.1016/S0926-9851(00)00023-9

Rathmann, N. M., Grinsted, A., Mosegaard, K., Lilien, D. A., Westhoff, J., Hvidberg, C. S., et al. (2022). Elastic wave propagation in anisotropic polycrystals: Inferring physical properties of glacier ice. *Proceedings of the Royal Society A: Mathematical, Physical and Engineering Sciences*, *478*(2268), 20220574. https://doi.org/10.1098/rspa.2022.0574

Rathmann, N. M., Hvidberg, C. S., Grinsted, A., Lilien, D. A., & Dahl-Jensen, D. (2021). Effect of an orientation-dependent non-linear grain fluidity on bulk directional enhancement factors. *Journal of Glaciology*, *67*(263), 569–575. https://doi.org/10.1017/jog.2020.117

Rathmann, N. M., & Lilien, D. A. (2021). Inferred basal friction and mass flux affected by crystal-orientation fabrics. *Journal of Glaciology*, *68*(268), 236–252. https://doi.org/10.1017/jog.2021.88

Rathmann, N. M., & Lilien, D. A. (2022). On the nonlinear viscosity of the orthotropic bulk rheology. *Journal of Glaciology*, *68*(272), 1243–1248. https://doi.org/10.1017/jog.2022.33

Rathmann, N. M., Lilien, D. A., Grinsted, A., Gerber, T. A., Young, T. J., & Dahl-Jensen, D. (2022). On the limitations of using polarimetric radar sounding to infer the crystal orientation fabric of ice masses. *Geophysical Research Letters*, *49*(1), 1–11. https://doi.org/10.1029/2021GL096244

Rathmann, N. M., Lilien, D. A., Richards, D. H., McCormack, F., & Montagnat, M. (2025). Rheological control of crystal fabrics on antarctic ice shelves. *Journal of Glaciology*. https://doi.org/10.31223/X58T6F

Raymond, C. F., & Harrison, W. D. (1975). Some observations on the behavior of the liquid and gas phases in temperate glacier ice. *Journal of Glaciology*, *14*(71), 213–233. https://doi.org/10.3189/S0022143000021717

Richards, D. H., Pegler, S. S., Piazolo, S., & Harlen, O. G. (2021). The evolution of ice fabrics: A continuum modelling approach validated against laboratory experiments. *Earth and Planetary Science Letters*, *556*, 116718. https://doi.org/10.1016/j.epsl.2020.116718

Richards, D. H., Pegler, S. S., Piazolo, S., Stoll, N., & Weikusat, I. (2023). Bridging the gap between experimental and natural fabrics: Modeling ice stream fabric evolution and its comparison with ice-core data. *Journal of Geophysical Research: Solid Earth*, *128*(11), 1–18. https://doi.org/10.1029/2023JB027245

Rignot, E., Mouginot, J., Scheuchl, B., Van Den Broeke, M., Van Wessem, M. J., & Morlighem, M. (2019). Four decades of Antarctic ice sheet mass balance from 1979–2017. *Proceedings of the National Academy of Sciences of the United States of America*, *116*(4), 1095–1103. https://doi.org/10.1073/pnas.1812883116

Roberts, J. H., McKinnon, W. B., Elder, C. M., Tobie, G., Biersteker, J. B., Young, D., et al. (2023). Exploring the interior of Europa with the Europa Clipper. *Space Science Reviews*, *219*(6), 46. https://doi.org/10.1007/s11214-023-00990-y

Robin, G. D. Q., Evans, S., & Bailey, J. T. (1969). Interpretation of radio echo sounding in polar ice sheets. *Philosophical Transactions of the Royal Society of London - Series A: Mathematical and Physical Sciences*, *265*(1166), 437–505. https://doi.org/10.1098/rsta.1969.0063

Robinson, E. S. (1968). Seismic wave propagation on a heterogeneous polar ice sheet. *Journal of Geophysical Research (1896-1977)*, *73*(2), 739–753. https://doi.org/10.1029/JB073i002p00739

Ross, N., Corr, H., & Siegert, M. (2020). Large-scale englacial folding and deep-ice stratigraphy within the West Antarctic Ice Sheet. *The Cryosphere*, *14*(6), 2103–2114. https://doi.org/10.5194/tc-14-2103-2020

Ruck, G. T., Barrick, D. E., Stuart, W. D., & Krichbaum, C. K. (1970). *Radar cross section handbook*. Springer US. https://doi.org/10.1007/978-1-4899-5324-7

Savage, M. K. (1999). Seismic anisotropy and mantle deformation: What have we learned from shear wave splitting? *Reviews of Geophysics*, *37*(1), 65–106. https://doi.org/10.1029/98RG02075

Scanlan, K. M., Buhl, D. P., & Blankenship, D. D. (2022). Polarimetric airborne radar sounding as an approach to characterizing subglacial röthlisberger channels. *Ieee Journal of Selected Topics in Applied Earth Observations and Remote Sensing*, *15*, 4455–4467. https://doi.org/10.1109/JSTARS.2022.3174473

Schaefer, J. M., Codilean, A. T., Willenbring, J. K., Lu, Z.-T., Keisling, B., Fülöp, R.-H., & Val, P. (2022). Cosmogenic nuclide techniques. *Nature Reviews Methods Primers*, *2*(1), 1–22. https://doi.org/10.1038/s43586-022-00096-9

Schlegel, R., Diez, A., Löwe, H., Mayer, C., Lambrecht, A., Freitag, J., et al. (2019). Comparison of elastic moduli from seismic diving-wave and ice-core microstructure analysis in Antarctic polar firn. *Annals of Glaciology*, *60*(79), 220–230. https://doi.org/10.1017/aog.2019.10

Schroeder, D. M., Bingham, R. G., Blankenship, D. D., Christianson, K., Eisen, O., Flowers, G. E., et al. (2020). Five decades of radioglaciology. *Annals of Glaciology*, *61*(81), 1–13. https://doi.org/10.1017/aog.2020.11

Schroeder, D. M., Blankenship, D. D., & Young, D. A. (2013). Evidence for a water system transition beneath Thwaites Glacier, West Antarctica. *Proceedings of the National Academy of Sciences of the United States of America*, *110*(30), 12225–12228. https://doi.org/10.1073/pnas.1302828110

Schroeder, D. M., Grima, C., & Blankenship, D. D. (2016). Evidence for variable grounding-zone and shear-margin basal conditions across Thwaites Glacier, West Antarctica. *Geophysics*, *81*(1), WA35–WA43. https://doi.org/10.1190/geo2015-0122.1

Seltzer, C., Llorens, M.-G., & Cross, A. J. (2024). Meltwater orientations modify seismic anisotropy in temperate ice. *Geophysical Research Letters*, *51*(13), e2024GL110131. https://doi.org/10.1029/2024GL110131

Seu, R., Phillips, R. J., Biccari, D., Orosei, R., Masdea, A., Picardi, G., et al. (2007). SHARAD sounding radar on the Mars reconnaissance orbiter. *Journal of Geophysical Research*, *112*(E5). https://doi.org/10.1029/2006je002745

Shen, S., & Gao, Y. (2021). Research progress on layered seismic anisotropy - A review. *Earthquake Research Advances*, *1*(1), 100005. https://doi.org/10.1016/j.eqrea.2021.100005

Shoji, H., & Langway, C. (1988). Flow-law parameters of the dye 3, Greenland, deep ice core. *Annals of Glaciology*, *10*, 146–150. https://doi.org/10.3189/s0260305500004433x

Shoji, H., & Langway, C. C. (1985). Mechanical properties of fresh ice core from Dye 3, Greenland. In *Greenland ice core: Geophysics, geochemistry, and the environment* (Vol. 33, pp. 39–48). American Geophysical Union (AGU). https://doi.org/10.1029/GM033p0039

Siegert, M. J., & Fujita, S. (2001). Internal ice-sheet radar layer profiles and their relation to reflection mechanisms between Dome C and the Transantarctic Mountains. *Journal of Glaciology*, *47*(157), 205–212. https://doi.org/10.3189/172756501781832205

Siegert, M. J., Kingslake, J., Ross, N., Whitehouse, P. L., Woodward, J., Jamieson, S. S. R., et al. (2019). Major ice sheet change in the Weddell Sea sector of West Antarctica over the last 5,000 years. *Reviews of Geophysics*, *57*(4), 1197–1223. https://doi.org/10.1029/2019RG000651

Siegert, M. J., & Kwok, R. (2000). Ice-sheet radar layering and the development of preferred crystal orientation fabrics between Lake Vostok and Ridge B, central East Antarctica. *Earth and Planetary Science Letters*, *179*(2), 227–235. https://doi.org/10.1016/S0012-821X(00)00121-7

Sihvola, A. (2000). Mixing rules with complex dielectric coefficients. *Subsurface Sensing Technologies and Applications*, *1*(4), 393–415. https://doi.org/10.1023/A:1026511515005

Smith, A. M. (1996). Ice shelf basal melting at the grounding line, measured from seismic observations. *Journal of Geophysical Research*, *101*(C10), 22749–22755. https://doi.org/10.1029/96JC02173

Smith, E. C., Baird, A. F., Kendall, J. M., Martín, C., White, R. S., Brisbourne, A. M., & Smith, A. M. (2017). Ice fabric in an Antarctic ice stream interpreted from seismic anisotropy. *Geophysical Research Letters*, *44*(8), 3710–3718. https://doi.org/10.1002/2016GL072093

Stokes, G. G. (1851). On the composition and resolution of streams of polarized light from different sources. *Transactions of the Cambridge Philosophical Society*, *9*, 399.

Stoll, N., Weikusat, I., Jansen, D., Bons, P., Darányi, K., Westhoff, J., et al. (2025). Linking crystallographic orientation and ice stream dynamics: Evidence from the EastGRIP ice core. *The Cryosphere*, *19*, 3805–3830. https://doi.org/10.5194/tc-19-3805-2025

Svendsen, B., & Hutter, K. (1996). A continuum approach for modelling induced anisotropy in glaciers and ice sheets. *Annals of Glaciology*, *23*, 262–269. https://doi.org/10.3189/s0260305500013525

Taylor, L. (1965). Dielectric properties of mixtures. *IEEE Transactions on Antennas and Propagation*, *13*(6), 943–947. https://doi.org/10.1109/TAP.1965.1138567

Thomas, R. E., Negrini, M., Prior, D. J., Mulvaney, R., Still, H., Bowman, M. H., et al. (2021). Microstructure and crystallographic preferred orientations of an azimuthally oriented ice core from a lateral shear margin: Priestley Glacier, Antarctica. *Frontiers in Earth Science*, *9*, 702213. https://doi.org/10.3389/feart.2021.702213

Thorsteinsson, T., Waddington, E. D., & Fletcher, R. C. (2003). Spatial and temporal scales of anisotropic effects in ice-sheet flow. *Annals of Glaciology*, *37*, 40–48. https://doi.org/10.3189/172756403781815429

Touzi, R., Lopes, A., Bruniquel, J., & Vachon, P. W. (1999). Coherence estimation for SAR imagery. *IEEE Transactions on Geoscience and Remote Sensing*, *37*(1), 135–149. https://doi.org/10.1109/36.739146

Ulaby, F. T., & Elachi, C. (1990). *Radar polarimetry for geoscience applications*. Taylor & Francis.

Ulaby, F. T., & Ravaioli, U. (2015). *Fundamentals of applied electromagnetics* (Vol. 7). Pearson Upper Saddle River, NJ.

Vazquez-Roy, J. L., Krozer, V., & Dall, J. (2012). Wideband dual-polarization microstrip patch antenna array for airborne ice sounder. *IEEE Antennas and Propagation Magazine*, *54*(4), 98–107. https://doi.org/10.1109/MAP.2012.6309160

Voigt, D. E. (2017). c-axis fabric of the south pole ice core, SPC14 [Dataset]. *U.S. Antarctic Program Data Center*. https://doi.org/10.15784/601057

Voigt, D. E., Alley, R., & Fitzpatrick, J. (2015). C-axis fabric from physical properties samples of the WAIS divide ice core [Dataset]. *U.S. Antarctic Program Data Center*. https://doi.org/10.7265/N5W093VM

Wang, B., Sun, B., Martin, C., Ferraccioli, F., Steinhage, D., Cui, X., & Siegert, M. J. (2018). Summit of the East Antarctic Ice Sheet underlain by thick ice-crystal fabric layers linked to glacial–interglacial environmental change. *Geological Society, London, Special Publications*, *461*(1), 131–143. https://doi.org/10.1144/SP461.1

Wang, N., Montagner, J. P., Fichtner, A., & Capdeville, Y. (2013). Intrinsic versus extrinsic seismic anisotropy: The radial anisotropy in reference Earth models. *Geophysical Research Letters*, *40*(16), 4284–4288. https://doi.org/10.1002/grl.50873

Warren, S. G. (1984). Optical constants of ice from the ultraviolet to the microwave. *Applied Optics*, *23*(8), 1206–1225. https://doi.org/10.1364/AO.23.001206

Weikusat, I., Jansen, D., Binder, T., Eichler, J., Faria, S. H., Wilhelms, F., et al. (2017a). Physical analysis of an Antarctic ice core—Towards an integration of micro- and macrodynamics of polar ice. *Philosophical Transactions of the Royal Society A: Mathematical, Physical and Engineering Sciences*, *375*(2086), 20150347. https://doi.org/10.1098/rsta.2015.0347

Weikusat, I., Jansen, D., Binder, T., Eichler, J., Faria, S. H., Wilhelms, F., et al. (2017b). Physical analysis of an Antarctic ice core–towards an integration of micro- and macrodynamics of polar ice. *Philosophical Transactions of the Royal Society A: Mathematical, Physical and Engineering Sciences*, *375*(2086), 20150347. https://doi.org/10.1098/rsta.2015.0347

Weikusat, I., Kipfstuhl, S., & Lambrecht, A. (2013). Crystal c-axes (fabric G20) of ice core samples collected from the EDML ice core with links to raw data files [Dataset]. *PANGAEA*. https://doi.org/10.1594/PANGAEA.807207

Weikusat, I., Lambrecht, A., & Kipfstuhl, S. (2013a). Eigenvalues of crystal orientation tensors for c-axes distributions of vertical thin sections from the EDML ice core [Dataset]. *PANGAEA*. https://doi.org/10.1594/PANGAEA.807141

Weikusat, I., Lambrecht, A., & Kipfstuhl, S. (2013b). Eigenvalues of crystal orientation tensors for c-axes distributions of vertical thin sections from the EDML ice core [Dataset]. *PANGAEA*. https://doi.org/10.1594/PANGAEA.807142

Weiss, T., Siegesmund, S., Rabbel, W., Bohlen, T., & Pohl, M. (1999). Seismic velocities and anisotropy of the lower continental crust: A review. *Pure and Applied Geophysics*, *156*(1–2), 97–122. https://doi.org/10.1007/s000240050291

Welch, B. C., & Jacobel, R. W. (2003). Analysis of deep-penetrating radar surveys of West Antarctica, US-ITASE 2001. *Geophysical Research Letters*, *30*(8), 1–4. https://doi.org/10.1029/2003GL017210

Welling, C., & Collaboration, T. R.-G. (2024). Brief communication: Precision measurement of the index of refraction of deep glacial ice at radio frequencies at Summit Station, Greenland. *The Cryosphere*, *18*(7), 3433–3437. https://doi.org/10.5194/tc-18-3433-2024

Westhoff, J., Stoll, N., Franke, S., Weikusat, I., Bons, P., Kerch, J., et al. (2021). A stratigraphy-based method for reconstructing ice core orientation. *Annals of Glaciology*, *62*(85–86), 191–202. https://doi.org/10.1017/aog.2020.76

Whitten, J. L., & Campbell, B. A. (2018). Lateral continuity of layering in the Mars south polar layered deposits from SHARAD sounding data. *Journal of Geophysical Research: Planets*, *123*(6), 1541–1554. https://doi.org/10.1029/2018je005578

Wilkinson, J., Beegle-Krause, C. J., Evers, K.-U., Hughes, N., Lewis, A., Reed, M., & Wadhams, P. (2017). Oil spill response capabilities and technologies for ice-covered arctic marine waters: A review of recent developments and established practices. *Ambio*, *46*(S3), 423–441. https://doi.org/10.1007/s13280-017-0958-y

Winebrenner, D. P., Smith, B. E., Catania, G. A., Conway, H. B., & Raymond, C. F. (2003). Radio-frequency attenuation beneath Siple Dome, West Antarctica, from wide-angle and profiling radar observations. *Annals of Glaciology*, *37*, 226–232. https://doi.org/10.3189/172756403781815483

Wittlinger, G., & Farra, V. (2015). Evidence of unfrozen liquids and seismic anisotropy at the base of the polar ice sheets. *Polar Science*, *9*(1), 66–79. https://doi.org/10.1016/j.polar.2014.07.006

Woodruff, A. H., & Doake, C. (1979). Depolarization of radio waves can distinguish between floating and grounded ice sheets. *Journal of Glaciology*, *23*(89), 223–232. https://doi.org/10.3189/s0022143000029853

Yan, J.-B., Li, L., Nunn, J. A., Dahl-Jensen, D., O'Neill, C., Taylor, R. A., et al. (2020). Multiangle, frequency, and polarization radar measurement of ice sheets. *IEEE Journal of Selected Topics in Applied Earth Observations and Remote Sensing*, *13*, 2070–2080. (Conference Name: IEEE Journal of Selected Topics in Applied Earth Observations and Remote Sensing). https://doi.org/10.1109/JSTARS.2020.2991682

Yeh, P. (1980). Optics of anisotropic layered media: A new 4 × 4 matrix algebra. *Surface Science*, *96*(1–3), 41–53. https://doi.org/10.1016/0039-6028(80)90293-9

Yoshida, M., Yamashita, K., & Mae, S. (1987). Bottom topography and internal layers in East Dronning Maud Land, East Antarctica, from 179 MHz radio echo-sounding. *Annals of Glaciology*, *9*, 221–224. https://doi.org/10.3189/S0260305500000665

Young, T. J., & Dawson, E. (2021). Quad-polarimetric ApRES measurements along a 6 km-long transect at the WAIS Divide, December 2019 (Version 1.0) [Dataset]. *NERC EDS UK Polar Data Centre*. https://doi.org/10.5285/ba1caf7a-d4e0-4671-972a-e567a25ccd2c

Young, T. J., Martín, C., Christoffersen, P., Schroeder, D., Tulaczyk, S. M., & Dawson, E. J. (2021). Rapid and accurate polarimetric radar measurements of ice crystal fabric orientation at the Western Antarctic Ice Sheet (WAIS) Divide ice core site. *The Cryosphere*, *15*(8), 4117–4133. https://doi.org/10.5194/tc-15-4117-2021

Young, T. J., Schroeder, D. M., Christoffersen, P., Lok, L. B., Nicholls, K. W., Brennan, P. V., et al. (2018). Resolving the internal and basal geometry of ice masses using imaging phase-sensitive radar. *Journal of Glaciology*, *64*(246), 649–660. https://doi.org/10.1017/jog.2018.54

Young, T. J., Schroeder, D. M., Jordan, T. M., Christoffersen, P., Tulaczyk, S. M., Culberg, R., & Bienert, N. L. (2021). Inferring ice fabric from birefringence loss in airborne radargrams: Application to the Eastern Shear Margin of Thwaites Glacier, West Antarctica. *Journal of Geophysical Research: Earth Surface*, *126*(5), 1–26. https://doi.org/10.1029/2020JF006023

Zebker, H. A., & Van Zyl, J. J. (1991). Imaging radar polarimetry: A review. *Proceedings of the IEEE*, *79*(11), 1583–1606. https://doi.org/10.1109/5.118982

Zeising, O., Arenas-Pingarrón, A., Brisbourne, A. M., & Martín, C. (2025). Brief communication: Reduced bandwidth improves the depth limit of the radar coherence method for detecting ice crystal fabric asymmetry. *The Cryosphere*, *19*, 2355–2363. https://doi.org/10.5194/tc-19-2355-2025

Zeising, O., Gerber, T. A., Eisen, O., Ershadi, M. R., Stoll, N., Weikusat, I., & Humbert, A. (2023). Improved estimation of the bulk ice crystal fabric asymmetry from polarimetric phase co-registration. *The Cryosphere*, *17*(3), 1097–1105. https://doi.org/10.5194/tc-17-1097-2023

Zeising, O., & Humbert, A. (2022). Polarimetric phase-sensitive radar measurements at EastGRIP drill site, 2019 [Dataset]. *PANGAEA*. https://doi.org/10.1594/PANGAEA.951267

Zhang, Z., Nakata, N., Karplus, M., Kaip, G., Qin, L., Li, Z., et al. (2024). Seismic full-wavefield imaging of the West Antarctic Ice Sheet interior near the ice flow divide. *Earth and Planetary Science Letters*, *636*, 118701. https://doi.org/10.1016/j.epsl.2024.118701

Zichu, X. (1985). Ice formation and ice structure on Law Dome, Antarctica. *Annals of Glaciology*, *6*, 150–153. https://doi.org/10.3189/1985AoG6-1-150-153